

ABSTRACT

We have measured the parity violating asymmetry with polarized electrons scattered elastically from protons. The result is $A = -15.05 \pm 0.98(stat) \pm 0.56(syst)$ ppm at the kinematic point $\langle\theta_{lab}\rangle = 12.3^\circ$ and $\langle Q^2\rangle = 0.477(GeV/c)^2$. The value for the linear combination of the strange form factors found using A is $G_E^s + 0.392G_M^s = 0.025 \pm 0.020 \pm 0.014$ where the first error is experimental and the second stems from the uncertainties in the electromagnetic form factors.

A Measurement of Parity Violating
Asymmetry with Polarized Electrons
Scattered from Protons and Implications
for Strange Form Factors

by

BARIS TAMER TONGUC

M. Sc. Physics Department, Syracuse University, Syracuse, NY, 1998.

DISSERTATION

Submitted in partial fulfillment of the requirements for the
degree of Doctor of Philosophy in Physics
in the Graduate School of Syracuse University

February 2003

Approved

Professor PAUL A. SOUDER

Date

© Copyright 2003 Baris T. Tonguc

All rights reserved

Committee Approval Page

Contents

1	Motivation and Physics	1
1.1	Introduction	1
1.2	Motivation	2
1.3	Physics	3
1.3.1	Cross Section	3
1.3.2	Matrix Element	5
1.3.3	Proton current	5
1.3.4	Matrix Elements For Electromagnetic and Weak Interactions	5
1.3.5	Scattering Amplitude and A^{PV}	7
1.3.6	A^{PV} in terms of the Proton Sach's Form Factors	8
1.3.7	Decomposition of Proton Form Factors	9
1.3.8	Reduction in the Number of Unknowns	9
1.3.9	A^{PV} as a function of Strange Quark Form Factors	12
1.4	A^{PV} in a compact form including radiative corrections.	12
1.5	Properties of Nucleon near $Q^2=0$	13
1.6	E158 Experiment	14
1.6.1	Introduction and Physics	14

2	Descriptions of Detectors and Simulations	16
2.1	Introduction	16
2.2	Overview of E158 Experiment	16
2.3	Møller and Mott Detectors	17
2.4	Møller Detector Design and Description	22
2.4.1	Mott Detector Design and Description	28
2.5	Simulations	28
2.5.1	Resolution Studies	35
2.5.2	Cascade Shower Studies	39
2.5.3	Simulations related to detectors and fiber bundles.	44
2.5.4	Mapping out the Radiation Level and Shielding Studies	52
3	Synchrotron Radiation Analysis	70
3.1	Introduction	70
3.2	Motivation	72
3.3	The Description of High Energy Synchrotron Light Monitor (SLM)	73
3.4	Pedestal Noise	73
3.5	Linearity Studies	79
3.6	The limit exerted on the Vertical Polarization by Synchrotron Ra- diation	80
3.7	SLM Asymmetry Width and Regression Analysis	84
3.8	What we have done	91
3.9	Conclusion	91
3.9.1	Technical Drawings of SLM	93
4	Asymmetry Corrections for HAPPEX	97

4.1	Introduction	97
4.2	Organization of the Data	97
4.3	Raw Asymmetry	98
4.4	Asymmetry correction	99
4.4.1	Computation of $\frac{\partial D'}{\partial M_i}$	100
4.4.2	Computation of ΔA	102
5	HAPPEX Results and Conclusions	107
5.1	Results	107
5.2	Discussion	111

List of Figures

1.1	<i>ep</i> scattering diagram	3
1.2	Showing the kinematics of e-p scattering in the lab frame	4
1.3	Feynmann diagrams of Møller scattering at tree level.	14
2.1	The outline of the accelerator at SLAC. Shown only parts relevant to the E158 experiment.	18
2.2	Møller detector	19
2.3	Møller and Mott detectors together. However, the Mott detector is shown mainly since it surrounds radially the Møller detector.	20
2.4	Upstream view. Beam pipe (hollow pipe), partially filled Møller (inner tube) and the Mott (outer tube) are detectors shown. The wedges, the sub elements, of the detectors are shown explicitly.	21
2.5	Møller (inner) and the Mott (outer) wedges placed on the beam pipe. Central line is the beam line.	24
2.6	The wedges of the Mott and the Møller detectors. The regions left within the bold lines show the slots where the fiber layers are placed.	25
2.7	Technical drawings of the cross sections of the Møller wedge (upper part) and the Mott wedge (lower part).	26
2.8	Møller fibers bending jig.	27

2.9	Cookies for both detectors. The cookie with many holes is for the fibers from Mott detector and the cookies embedded into Al back plate are for those from Møller detector.	29
2.10	The dimensional outline and the base diagrams of the PMTs used for the detectors [30]. (Courtesy HAMAMATSU.)	30
2.11	A sketch of a light guide and mirrors (side view). Upper left part of the figure is the cylindrical hole in which a PMT is situated. Length unit is inch.	31
2.12	A sketch of the Mirror I which connects the cookie to the light guide (side view).	32
2.13	A sketch of the Mirror II which connects the light guide to the cylindrical cavity where the PMT is situated. (side view).	33
2.14	The distribution of detected light by the detector by 18 GeV electrons.	36
2.15	Total Cu thickness (cm) vs. resolution (%) while quartz layer thickness is fixed at the nominal value of 1 cm.	37
2.16	Quartz layer thickness (cm) vs. resolution (%) while Cu layer thickness is fixed at the nominal value of 1.5 cm.	38
2.17	Cu layer thickness (cm) vs. resolution (%) while both quartz layer thickness and total Cu thickness are fixed at the nominal values of 1 cm and 24 cm respectively.	40
2.18	Fractional energy loss per radiation length (%) vs. Depth of Cu medium (radiation length)	41
2.19	Distribution of the number of events vs. Fractional energy loss per radiation length (%) a) top left; within 5th radiation length, b) top right; within 6th radiation length, c) bottom left; within 7th radiation length, b) bottom right; within 8th radiation length.	42

2.20	Lateral shower development for 30 GeV electrons impinging the medium at origin. Numbers in the graph are believed to represent the total tracks entering in that vicinity.	43
2.21	Drawing of the cross section of detectors above the beam line. . . .	45
2.22	The total energy deposited by 18 GeV electrons to the Møller detector (top left), to the Mott detector (top right) and to the quartz layers (bottom left) behind the Møller detector as a function of initial beam location. Vertical lines in the graphs are drawn to show the border between the Møller and the Mott detectors in radial direction.	48
2.23	Simulation result that shows the radial distributions of outgoing electrons at the detector region. The first and the third peak or rather the wide bump are the distributions of the Mott electrons, <i>i.e.</i> the electrons scattered by the protons in the target. Second peak with dashed lines is the distribution of the Møller electrons, <i>i.e.</i> the electrons scattered by the orbital electrons in the target. . .	49
2.24	Simulation result that shows the radial distributions of outgoing electrons, <u>weighted by their momentum</u> , at the detector region. The first and the third peak are the distributions of the Mott electrons. Second wide peak with dashed lines is the distribution of the Møller electrons. The vertical axis is in logarithmic scale.	50

2.25	The total energy deposited by <i>10 MeV photons</i> in the Møller detector (top left), in the Mott detector (top right) and in the quartz layers (bottom left) behind the Møller detector as a function of initial beam location. Vertical lines in the graphs are drawn to show the border between the Møller and the Mott detectors in radial direction.	53
2.26	The crosssection of cylindrical geometry above the beam line in the case where 3 radiation length of carbon is placed at the front. . . .	54
2.27	The total energy deposited by <i>10 MeV photons</i> in the Møller detector (top left) and in the quartz layers behind the Møller detector (bottom left) as a function of the initial beam locations. Empty circles (full circles) represent the data taken from the geometry where there is (no) 3 radiation length of carbon radiator at the front. Top right (bottom right) graph shows the improvement factor due to C preradiator throughout the detector surfaces when Møller detector (the quartz layers) is (are) considered.	55
2.28	The total energy deposited by <i>18 GeV electrons</i> in the Møller detector (top left) and in the quartz layers behind the Møller detector (bottom left) as a function of the initial beam locations. Empty circles (full circles) represent the data taken from the geometry where there is (is no) 3 radiation length of carbon radiator at the front. Top right (bottom right) graph shows the improvement factor due to C preradiator throughout the detector surfaces when Møller detector (the quartz layers) is (are) considered.	56
2.29	The cross section of cylindrical geometry above the beam line. . . .	58

2.30	The energy deposited in the diagnostic rings per event as a percentage of the initial energy of the beam.	59
2.31	The energy deposited in the diagnostic rings per event in the absorbed dosage unit of $rad \times 10^{-9}$	60
2.32	The cross section of cylindrical geometry above the beam line. In this case a new Pb shielding is added to the geometry.	63
2.33	The energy deposited in the diagnostic rings per event in the absorbed dosage unit of $rad \times 10^{-9}$ in the case where a new Pb shielding is added (Fig. 2.32).	64
2.34	The cross section of cylindrical geometry above the beam line. In one case, the extra Pb shielding is kept and in the other case it is removed. Also, Pb shielding in the back is trimmed up to the r_{min} of ring 9. Also sub-configurations are shown in which the ring 9 inserted into the latter shielding by 3 cm and by 6 cm in the z, or beam line axis direction.	65
2.35	Energy depositions in the rings for three configurations. Data marked by circle, square and triangle represents the cases where the displacements of ring 9 are 0 cm, 3 cm and 6 cm in z direction respectively.	66
2.36	Energy depositions in the rings for three configurations obtained while the extra Pb shielding is placed to the geometry (see Fig. 2.34). Data marked by circle, square and triangle represents the cases where the displacements of ring 9 are 0 cm, 3 cm and 6 cm in z direction respectively.	68

2.37	Energy depositions from ring 9 vs Δz or the displacement relative to $z=34.5$ cm, the initial ring position. The fitted data marked with circle in the upper and square in the lower plot correspond the simulations when there is no extra shielding and when there is an extra shielding respectively.	69
3.1	Overview of A-line.	71
3.2	A digital image of both low and high energy SR detectors beside the beam pipe	74
3.3	Detector system for MeV SR photons	75
3.4	Showing the Cherenkov radiator, 45° tilted mirror and interior of the box.	76
3.5	Showing photodiode array mounted to the backplate of the high energy SR detector box.	77
3.6	Circuit design of the photodiodes, showing two channels out of four.	78
3.7	The pedestal and the raw signal of synchrotron light monitor 1 in the unit of the ADC counts	79
3.8	Synchrotron light monitor 1 (SLM 1) asymmetry vs. toroid asymmetry for run 1799.	81
3.9	Normalized SLM 1 Asymmetry vs. Energy bpm resolution ($\Delta E/E$) taken from beam position monitor 12 and 24 in the horizontal direction for the run 1470, P2 is the slope of the fit.	82
3.10	Normalized SLM 1 Asymmetry vs. Sum of two energy bpm resolution, $[(\Delta E_{bpm12} + \Delta E_{bpm24})/E]$, P2 is the slope of the fit.	83

3.11	Showing <i>normalized</i> SLM 1 raw asymmetry for run 1799 a) upper plot; no cut case, b) bottom plot; the same as a) except for with cutting one outlier event.	86
3.12	First order polynomial fits of a) top left; $A_{raw}(= A_0)$ vs. E_{sum} , b) top right; $A_1(= A_{raw} - C_{Esum} \cdot E_{sum})$ vs. x , c) bottom left; $A_2(= A_{raw} - C_{Esum} \cdot E_{sum} - C_x \cdot x)$ vs. y , d) bottom right; $A_3(= A_{raw} - \sum_{i=1}^3 C_i \cdot x_i)$ vs. θ_x . P2s are the slopes of the fits and are the correlation coefficients at the same time.	88
3.13	First order polynomial fit of $A_4(= A_{raw} - \sum_{i=1}^4 C_i \cdot x_i)$ vs. θ_y , as continuation of the previous figure.	89
3.14	<i>Normalized</i> SLM 1 asymmetry distribution a) top plot; raw, b) bottom plot; regressed to $E, x, y, \theta_x, \theta_y$ for the run 1470	90
3.15	Sum of SLM 1 and SLM 2 <i>normalized</i> asymmetry distribution a) top plot; raw, b) bottom plot; regressed to $E, x, y, \theta_x, \theta_y$ for the run 1470	92
3.16	Technical drawing of quartz bar.	94
3.17	Technical drawing of high energy synchrotron radiation detector backplate.	95
3.18	Technical drawing of high energy synchrotron radiation detector box.	96
4.1	Hall A beam line instrumentation.	101
4.2	Representative plots of the a_i versus run number for slug 11 including their fits to straight line.	103
4.3	Representative plots of the a_i overall slugs.	104

4.4	Asymmetry corrections for detectors I and II versus Slug number. Results using the straightforward method are also shown as solid circles.	106
5.1	Plot of A_{raw} versus data set number. The full circles are from left spectrometer and the empty circles are from the right spectrometer. The superimposed pattern is due to half wave plate mode.	108
5.2	Showing a part of the electron polarization measurements performed daily basis via both Moller and Compton polarimetry methods. . .	108
5.3	Plot of G_E^s versus G_M^s at $Q^2 = 0.477 \text{ (GeV/c)}^2$ is accompanied by the data points from various models [3, 5, 7–9] at the same Q^2 . The numbers near the data points are the reference numbers of the models. Ref. [9] is plotted twice due to a sign ambiguity.	110

Acknowledgments

I am immensely grateful to my advisor Prof. Paul A. Souder for his tremendous support, patience, guidance and the freedom he provided. Without him, this thesis would not have happened. Dedication to his work and ability to see important problems out of so many issues continues to impress me. I would like to thank Dr. Rich S. Holmes for being extremely helpful to me since I joined the group. I must thank to Dr. William E. Kahl for sharing his knowledge and experience. I would like to thank Dr. Mike Woods for making my stay at SLAC fruitful. Many thanks to Dr. Krishna S. Kumar and Dr. Robert W. Michael for spending time for me, and for the help at JLab and at SLAC. I would like to thank Diane Sanderson and Linda Pesce for taking care of administrative details for me. I am indebted to Imran Younus for all the fun, friendship, coffee and good conversation. I would also like to thank Rashid Ayad for finding time to share his knowledge and experience on the simulations inspite of his busy schedule. I thank Salah Nasri and Waled Emam for theoretical discussions. I would like to thank Lou Buda for sharing his documents about detectors. I appreciate Joe Schechter, Carl Rosenzweig and Marina Artuso for their utmost assistance during my very first semester at Syracuse University. I continue to enjoy rewarding friendship of Murat Kose, Mehmet Yavuz, Haci A. Mantar, Bekir Kayacan. I would like to thank my wife Aslihan for her sacrifices she made for me. Without her, I don't think I could have made it. I would like to thank my kids Betul and Halil for making home more noisy and cheerful than ever. I would like to thank my

brother and sister for being there. Most of all, I would like to thank my mother and my father for their unconditional love and support.

To my Mother and my Father

Chapter 1

Motivation and Physics

1.1 Introduction

Due to time scale of the experiments in the particle physics, my thesis is composed of two experiments: HAPPEX and E158. Unlike E158, HAPPEX has been completed. Therefore, the physics and the results of the HAPPEX are given in the first and the last chapter. The physics of the E158 is given briefly at the last section of the first chapter. Since my hardware experience is based on E158, I give the descriptions and simulations of E158 detectors built at Syracuse after a very brief overview of the instrumentation of the experiment. Chapter 3 and 4 cover the analysis of specific tasks in E158 and HAPPEX experiments respectively. The setup for monitoring synchrotron radiation emitted while the electron beam is bent towards the target, and the analysis of the initial data is covered in chapter 3. In chapter 4, the procedure and the setup to correct the raw asymmetry against the nonzero helicity correlations is covered, and the results of the analysis are presented.

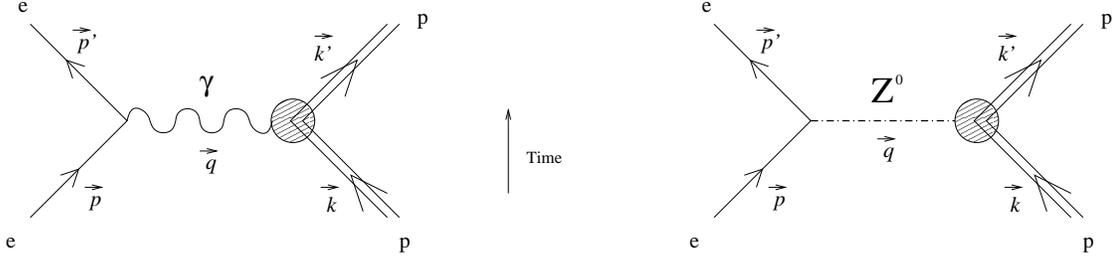
1.2 Motivation

Although the proton is often described as a bound state of three (2 up and 1 down) quarks these are best thought of as “valence” quarks and not the whole story. It is believed that besides the valence quarks there is another part described as the sea, which is comprised of quark-antiquark pairs and gluons. The naive assumption was that the sea wouldn’t contribute to the properties of proton. After the publication of deep inelastic scattering data regarding the spin structure of the proton, this assumption has been shown to be wrong. Indeed only a relatively small fraction of proton spin was due to quark spins [1], [2].

At Jlab, the collaboration of HAPPEX (Hall A Proton Parity EXperiment) measured the strange quark constituent in the proton by exploiting the parity violating scattering of polarized electrons from proton. The measured quantity is a parity violating asymmetry and is defined by

$$A^{PV} \equiv \frac{\sigma_R - \sigma_L}{\sigma_R + \sigma_L}, \quad (1.2.1)$$

where σ_R is the differential cross section of right-handed electrons, i.e., electrons with their spin and momentum parallel, and σ_L is the differential cross section of left-handed electrons, i.e., electrons with their spin and momentum anti-parallel. As shown explicitly below the above equation gives us a direct measurement of quantities called strange form factors G_E^s and G_M^s , which are related to the strange charge distribution and the strange magnetic moment distribution. Nonzero values would constitute a clear contribution from the sea in general and strange quarks in particular to the electric and magnetic properties of proton.

Figure 1.1: ep scattering diagram

1.3 Physics

There are two types of interactions relevant as far as the ep scattering concerned. First is the electromagnetic, mediated by a virtual photon (γ), and second is the weak, mediated by a massive neutral vector boson, Z^0 . They both carry momentum $\vec{q} = (\vec{p} - \vec{p}')$. The related Feynman diagrams at tree level are shown in Fig(1.1). By using “Feynman rules”, cross section can be calculated for both interactions [6].

1.3.1 Cross Section

For a collision between particle 1 and 2, producing particles 3, 4, ..., n :

$$1 + 2 \rightarrow 3 + 4 + \dots + n \quad (1.3.1)$$

the cross section is given by a general formula called the Golden Rule for scattering which is

$$d\sigma = |\mathcal{M}|^2 \frac{\hbar^2 S}{4\sqrt{(p_1 \cdot p_2)^2 - (m_1 m_2 c^2)^2}} \left[\left(\frac{c d^3 \mathbf{p}_3}{(2\pi)^3 2E_3} \right) \left(\frac{c d^3 \mathbf{p}_4}{(2\pi)^3 2E_4} \right) \dots \left(\frac{c d^3 \mathbf{p}_n}{(2\pi)^3 2E_n} \right) \right] \times (2\pi)^4 \delta^4(p_1 + p_2 - p_3 - p_4 \dots - p_n) \quad (1.3.2)$$

where $p_i = (E_i/c, \mathbf{p}_i)$ is the four-vector momentum of particle i (mass m_i), $E_i = c\sqrt{m_i^2 c^2 + \mathbf{p}_i^2}$, and S is a statistical factor ($1/j!$ for each group of j identical parti-

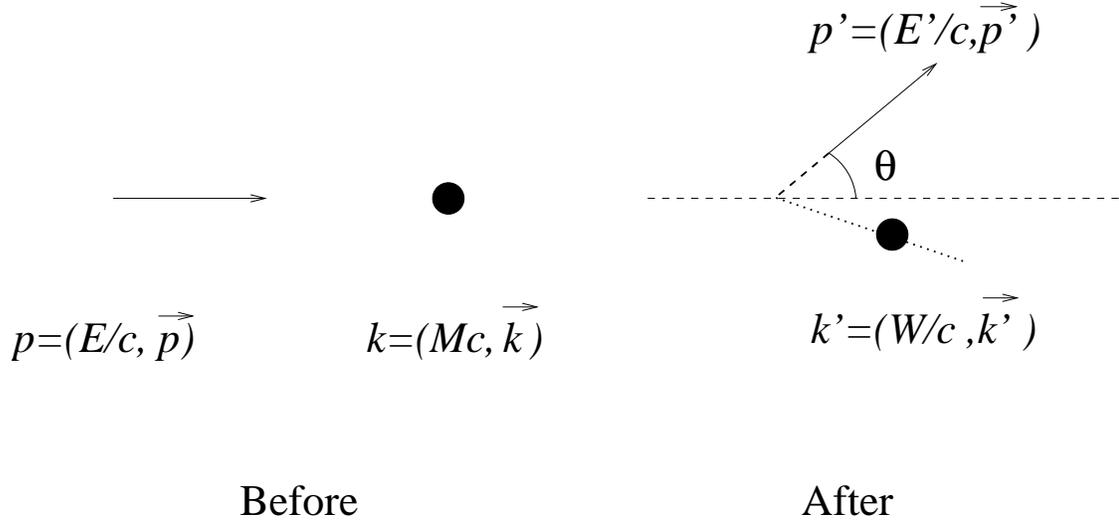


Figure 1.2: Showing the kinematics of e-p scattering in the lab frame

cles in the final state). Here, the Dirac delta function imposes the conservation of energy and momentum. In addition, \mathcal{M} is the matrix element which contains the dynamical information for a process. Now, applying the formula above (Eq. 1.3.2) to the case of the elastic e-p scattering in the lab frame by neglecting the mass of the electron (Fig. 1.2), one finds the differential cross section as

$$\frac{d\sigma}{d\Omega} = \left(\frac{\hbar E'}{8\pi M c E} \right)^2 |\mathcal{M}|^2 \quad (1.3.3)$$

where E and E' are the energies of the incoming and the outgoing electron. Also, M is the mass of the proton. The matrix element, \mathcal{M} , comes out of the integration (1.3.2) intact, since this is valid for the cases of two-body final state. Otherwise, we need to know the explicit functional form of the matrix element to carry out the integration. In any case, sooner or later, we need the explicit form of the matrix element to obtain the explicit differential cross section for the relevant process(es).

1.3.2 Matrix Element

The matrix element contains the dynamical information of an interaction. For particles 1 and 2, it is given by

$$\mathcal{M} = g_1 j_{1\mu} \left(\frac{-1}{q^2 - M_B^2} \right) g_2 j_2^\mu \quad (1.3.4)$$

where g s and j s are the charges and the currents of the particles respectively. The fraction term is the propagator term which is related to the mediator particle. Also, M_B is the mass of the boson propagator.

1.3.3 Proton current

Since the proton is a composite particle unlike leptons¹, quarks etc. we cannot treat it as a point-like particles. The matrix element of the proton current (j_μ^{pa}) is given by

$$j_\mu^{pa} = \bar{u} [F_1^{pa}(Q^2) \gamma_\mu + \frac{i}{2M} F_2^{pa}(Q^2) \sigma_{\mu\nu} q^\nu + F_A^{pa}(Q^2) \gamma_\mu \gamma^5] u \quad (1.3.5)$$

where a is the label for the mediator particle which the proton interacts with. Moreover, F^{pa} 's are called proton form factors and are only functions of Q^2 where Q is the four-vector momentum transfer.

1.3.4 Matrix Elements For Electromagnetic and Weak Interactions

We can write down the matrix elements for both electromagnetic and weak interactions by substituting the appropriate charges and currents in Eq.(1.3.4). The

¹See reference [4] for elastic $e\mu$ scattering as an example to interactions between the two point-like particles.

matrix element of the electromagnetic channel of the interaction becomes as follows.

$$\begin{aligned} \mathcal{M}_{EM} = & (-e) [\bar{u}\gamma_\mu u] \left(\frac{-1}{q^2} \right) (+e) \\ & \left[\bar{u}_p \left\{ F_1^{p\gamma} \gamma^\mu + \frac{i}{2M} F_2^{p\gamma} \sigma^{\mu\nu} q_\nu \right\} u_p \right] \end{aligned} \quad (1.3.6)$$

where the proton spinors were labelled with the subscript p . As far as the matrix element for the neutral weak interaction is concerned, we have two matrix elements because weak electron charge and current differ from one helicity state to another. The weak charge of left-handed electron is given by;

$$g_L = T_3 - Q \sin^2 \theta_W \quad (1.3.7)$$

where T_3 is third component of weak isospin number and here its value is $(-1/2)$ and Q is the electric charge number in unit of e and is -1 . Also θ_W is known as weak mixing angle. Thus, left-handed weak charge of electron will be:

$$g_L^e = -\frac{1}{2} + \sin^2 \theta_W \quad (1.3.8)$$

and the neutral weak current of the left-handed electron is given by

$$j_\mu^{eL} = [\bar{u}\gamma_\mu \frac{(1 - \gamma_5)}{2} u] \quad (1.3.9)$$

Due to the massiveness of the Z^0 , propagator term becomes $(q^2 - M_Z^2)^{-1}$. In addition, proton terms can be found by using the Eq.(1.3.5) as follows:

$$g^p j_\mu^{pZ} = \bar{u} \left\{ g_V^p (F_1^{pZ} \gamma_\mu + \frac{i}{2M} F_2^{pZ} \sigma_{\mu\nu} q^\nu) + g_A^p (F_A^{pZ} \gamma_\mu \gamma^5) \right\} u \quad (1.3.10)$$

where $g_V = (g_R + g_L)/2$ and $g_A = (g_R - g_L)/2$ are called as the spin-averaged weak charge and the difference in the charges respectively. Therefore, the matrix

element of neutral weak interaction between *left-handed* electron and unpolarized proton can be written straightforwardly as:

$$\begin{aligned} \mathcal{M}_Z^{(L)} = & \left(-\frac{1}{2} + \sin^2\theta_W\right) \left[\bar{u}\gamma_\mu\frac{(1-\gamma_5)}{2}u\right] \left(\frac{-1}{q^2 - M_Z^2}\right) \\ & \left[\bar{u}_p\left\{g_V^p(F_1^{pZ}\gamma^\mu + \frac{i}{2M}F_2^{pZ}\sigma^{\mu\nu}q_\nu) + g_A^p(F_A^{pZ}\gamma^\mu\gamma^5)\right\}u_p\right] \end{aligned} \quad (1.3.11)$$

In similar fashion, the matrix element of the neutral weak interaction between *right-handed* electron and unpolarized proton is as follows:

$$\begin{aligned} \mathcal{M}_Z^{(R)} = & (\sin^2\theta_W) \left[\bar{u}\gamma_\mu\frac{(1+\gamma_5)}{2}u\right] \left(\frac{-1}{q^2 - M_Z^2}\right) \\ & \left[\bar{u}_p\left\{g_V^p(F_1^{pZ}\gamma^\mu + \frac{i}{2M}F_2^{pZ}\sigma^{\mu\nu}q_\nu) + g_A^p(F_A^{pZ}\gamma^\mu\gamma^5)\right\}u_p\right] \end{aligned} \quad (1.3.12)$$

1.3.5 Scattering Amplitude and A^{PV}

Before going any further, we need to answer the question of whether we add amplitudes or cross sections for a polarized electron? When we observe an elastically scattered electron, there is no way we can tell what type of interaction is selected. That means that the scattering process is coherent. As a result, we need to add the amplitudes rather than the cross sections for an helicity state during the calculation of the asymmetry. Thus, for left(right)-handed electrons, total amplitude is

$$\mathcal{M}_{L(R)} = \mathcal{M}^\gamma + \mathcal{M}_{L(R)}^Z \quad (1.3.13)$$

If we substitute them in Eq. (1.2.1), the parity violating asymmetry may be written in terms of amplitudes as:

$$A^{PV} = \frac{|\mathcal{M}_R|^2 - |\mathcal{M}_L|^2}{|\mathcal{M}_R|^2 + |\mathcal{M}_L|^2} \quad (1.3.14)$$

1.3.6 A^{PV} in terms of the Proton Sach's Form Factors

Sach's form factors, which are convenient to use in A^{PV} , are defined as follows

$$G_E^a \equiv F_1^a - \tau F_2^a \quad , \quad G_M^a \equiv F_1^a + F_2^a \quad (1.3.15)$$

where $\tau \equiv Q^2/(4M^2)$ and superscript 'a' stands for mediator particle either γ or Z^0 in our case.

Finally, the parity violating asymmetry in terms of Sach's proton form factors is given by

$$A^{PV} = \left[\frac{-G_F Q^2}{\pi \alpha \sqrt{2}} \right] \times \frac{\epsilon G_E^{p\gamma} G_E^{pZ} + \tau G_M^{p\gamma} G_M^{pZ} - \frac{1}{2}(1 - 4\sin^2\theta_W)\epsilon' G_M^{p\gamma} G_A^{pZ}}{\epsilon(G_E^{p\gamma})^2 + \tau(G_M^{p\gamma})^2} \quad (1.3.16)$$

where G_F is the Fermi coupling constant given by

$$G_F \equiv \frac{\sqrt{2}}{8} \left(\frac{g_W}{M_W c^2} \right)^2 (\hbar c)^3$$

or alternatively in terms of the charge and the mass of Z^0 particle.

$$G_F = \frac{\sqrt{2}}{8} \left(\frac{g_Z}{M_Z c^2} \right)^2 (\hbar c)^3.$$

Here we have used $g_W = g_Z \cos\theta_W$, since according to electroweak theory

$$g_W = \frac{g_e}{\sin\theta_W} \quad , \quad g_Z = \frac{g_e}{\sin\theta_W \cos\theta_W}$$

and $M_W = M_Z \cos\theta_W$. In addition, Q and α are four-vector momentum transfer and the fine structure constant respectively. $G_{E(M)}^{p\gamma,Z}$ is proton's electric(magnetic) Sach's form factor while exchanging a γ or a Z^0 particle. The term G_A^{pZ} is equivalent to F_A^{pZ} . Also ϵ and ϵ' are kinematic quantities given by $[1 + 2(1 + \tau)\tan^2(\theta/2)]^{-1}$ and $\sqrt{\tau(1 + \tau)(1 - \epsilon^2)}$ respectively.

1.3.7 Decomposition of Proton Form Factors

In order not to get lost let's recall our main goal that is to measure strange form factors via A^{PV} . So far, what we have is the equation (1.3.16) which includes only form factors of the proton. Fortunately, proton form factors can be expressed in terms of form factors of quarks (Eq. 1.3.17, Eq. 1.3.18 and Eq. 1.3.19). These relations will help us obtain parity violating asymmetry as a function of quark form factors.

$$F_i^{p\gamma} = \sum_j^3 q^j F_i^j = \frac{2}{3}F_i^u - \frac{1}{3}F_i^d - \frac{1}{3}F_i^s \quad i : 1, 2 \quad (1.3.17)$$

$$F_i^{pZ} = \sum_j^3 g_V^j F_i^j = \left(\frac{1}{4} - \frac{2}{3}\sin^2\theta_W\right)F_i^u - \left(\frac{1}{4} - \frac{1}{3}\sin^2\theta_W\right)(F_i^d + F_i^s) \quad i : 1, 2 \quad (1.3.18)$$

where $g_V^j = (g_R^j + g_L^j)/2$ is the spin averaged weak charge of the j th quark.

$$F_A^{pZ} = \sum_j^3 g_A^j F^j = -\frac{1}{4}F_A^u + \frac{1}{4}(F_A^d + F_A^s) \quad (1.3.19)$$

where $g_A^j = (g_R^j - g_L^j)/2$ is difference in the weak charges of the j th quark. Since charm and much heavier quarks have masses comparable or heavier than the mass of the proton, their contribution are expected to be negligible beside those of lighter quarks. Therefore, form factors of those quarks were eliminated.

1.3.8 Reduction in the Number of Unknowns

After decomposing the proton form factor into the form factors of the three quark flavors, we end up with nine unknown form factors, since there are three form

factors arise for each quark flavor. The list is as follows:

$$F_1^u, \quad F_2^u, \quad F_A^u$$

$$F_1^d, \quad F_2^d, \quad F_A^d$$

$$F_1^s, \quad F_2^s, \quad F_A^s$$

We need other equations to deal with reducing the number of unknowns. Now, electromagnetic form factors for the proton as well as for the neutron are known. In addition, by assuming *strong* isospin symmetry we can relate neutron form factors to quark form factors. Under isospin:

$$p \rightarrow n \quad \Rightarrow \quad u \rightarrow d, \quad d \rightarrow u, \quad s \rightarrow s.$$

which implies that:

$$F_i^u \equiv F_i^{pu} = F_i^{nd}; \quad F_i^d \equiv F_i^{pd} = F_i^{nu}; \quad F_i^s \equiv F_i^{ps} = F_i^{ns} \quad (1.3.20)$$

Thus, by looking Eq. 1.3.17, we can read off $F_i^{n\gamma}$ directly as

$$F_i^{n\gamma} = \frac{2}{3}F_i^d - \frac{1}{3}F_i^u - \frac{1}{3}F_i^s \quad i : 1, 2 \quad (1.3.21)$$

By using Eq. 1.3.17 and Eq. 1.3.21 we obtain

$$F_i^u - F_i^d = F_i^{p\gamma} - F_i^{n\gamma} \quad (1.3.22)$$

If we substitute Eq. 1.3.22 in Eq.1.3.18 we get F_i^{pZ} in terms of the electromagnetic form factors of the proton, neutron and strange quarks, which is

$$F_i^{pZ} = \frac{1}{4}(F_i^{p\gamma} - F_i^{n\gamma}) - \sin^2\theta_W F_i^{p\gamma} - \frac{1}{4}F_i^s \quad (1.3.23)$$

So far, we eliminated four unknowns, which are F_i^u and F_i^d . Furthermore,

$$F_A^{pZ} \equiv G_A^{pZ} = -\frac{1}{2}G_A^\beta + \frac{1}{4}G_A^s \quad (1.3.24)$$

where G_A^s is equivalent to F_A^s , and $G_A^\beta = \frac{1}{2}(F_A^u - F_A^d)$ is empirically known. By plugging the definition (Eq. 1.3.15) into Eq. 1.3.17, Eq. 1.3.18 and Eq. 1.3.23, we can obtain Sach's form factors. Accordingly, $G_E^{p\gamma}$, $G_M^{p\gamma}$, G_E^{pZ} and G_M^{pZ} in terms of quark Sach's form factors are

$$G_E^{p\gamma} = \frac{2}{3}G_E^u - \frac{1}{3}G_E^d - \frac{1}{3}G_E^s \quad (1.3.25)$$

$$G_M^{p\gamma} = \frac{2}{3}G_M^u - \frac{1}{3}G_M^d - \frac{1}{3}G_M^s \quad (1.3.26)$$

$$\begin{aligned} G_E^{pZ} &= \left(\frac{1}{4} - \frac{2}{3}\sin^2\theta_W\right) G_E^u - \left(\frac{1}{4} - \frac{1}{3}\sin^2\theta_W\right) G_E^d \\ &\quad - \left(\frac{1}{4} - \frac{1}{3}\sin^2\theta_W\right) G_E^s \end{aligned} \quad (1.3.27)$$

$$\begin{aligned} G_M^{pZ} &= \left(\frac{1}{4} - \frac{2}{3}\sin^2\theta_W\right) G_M^u - \left(\frac{1}{4} - \frac{1}{3}\sin^2\theta_W\right) G_M^d \\ &\quad - \left(\frac{1}{4} - \frac{1}{3}\sin^2\theta_W\right) G_M^s \end{aligned} \quad (1.3.28)$$

Also G_E^{pZ} and G_M^{pZ} in terms of electromagnetic Sach's form factors for the proton, the neutron, and the strange quark are

$$G_E^{pZ} = \left(\frac{1}{4} - \sin^2\theta_W\right) G_E^{p\gamma} - \frac{1}{4}G_E^{n\gamma} - \frac{1}{4}G_E^s \quad (1.3.29)$$

$$G_M^{pZ} = \left(\frac{1}{4} - \sin^2\theta_W\right) G_M^{p\gamma} - \frac{1}{4}G_M^{n\gamma} - \frac{1}{4}G_M^s \quad (1.3.30)$$

The last two equations clearly establish links to the strange quark form factors, since electric and magnetic Sach's form factors for the proton are known as was stated earlier.

1.3.9 A^{PV} as a function of Strange Quark Form Factors

In the previous section, we linked the weak proton form factors to the strange quark form factors. Now, we will use those relations to obtain the parity violating asymmetry, A^{PV} . If we substitute Eq. 1.3.29, Eq. 1.3.30 and Eq. 1.3.24 into Eq. 1.3.16, then parity violating asymmetry in lowest or tree level will be

$$\begin{aligned}
 A^{PV} = & - \left[\frac{G_F M_p^2 \tau}{\sqrt{2} \pi \alpha \xi} \right] \left((1 - 4 \sin^2 \theta_W) \xi - \epsilon G_E^{p\gamma} G_E^{n\gamma} - \tau G_M^{p\gamma} G_M^{n\gamma} \right) \\
 & + \left[\frac{G_F M_p^2 \tau}{\sqrt{2} \pi \alpha \xi} \right] \left(\epsilon G_E^{p\gamma} G_E^s + \tau G_M^{p\gamma} G_M^s \right) \quad (1.3.31)
 \end{aligned}$$

where $\xi \equiv \epsilon(G_E^{p\gamma})^2 + \tau(G_M^{p\gamma})^2$. As can be noticed from Eq. 1.3.31, only strange form factors, G_E^s and G_M^s , remain as unknowns. The first part of the formula consists of known terms and is about 14 parts per million (ppm) at the kinematical point for the HAPPEX experiment, $Q^2 = 0.477(GeV/c)^2$. The second part including the strange form factors is expected to be small.

The result above gives a direct relation between the parity violating asymmetry and strange quark form factors. Consequently, if we measure an asymmetry different than the calculated one in the case for null strange form factors then the difference between the two can be attributed to *nonzero* strange form factors.

1.4 A^{PV} in a compact form including radiative corrections.

If $G^0 (\equiv (G^u + G^d + G^s)/3)$ is used instead of G^s and if the radiative corrections are included in the Eq.1.3.31 then A^{PV} is given by

$$A^{PV} = -A_0 \tau \rho'_{eq} \left(2 - 4\hat{\kappa}'_{eq} \sin^2 \theta_W - \frac{\epsilon \eta_p}{\epsilon \eta_p^2 + \tau \mu_p^2} \frac{G_E^0 + \beta G_M^0}{(G_M^{p\gamma}/\mu_p)} \right) - A_A \quad (1.4.1)$$

where $A_0 = (G_F M_p^2)/(\sqrt{2}\pi\alpha)$, $\mu_p(\mu_n) \approx 2.79(-1.91)$ is the proton(neutron) magnetic moment, $\eta_p = G_E^{p\gamma}(Q^2)/(G_M^{p\gamma}(Q^2)/\mu_p)$, and $\beta = \tau \mu_p/(\epsilon \eta_p)$. For our kinematics, the axial form factor of the proton is given in the Ref. [37] as $A_A = (0.56 \pm 0.23)$ ppm. $\rho'_{eq} = 0.9878$ and $\hat{\kappa}'_{eq} = 1.0027$ are the parameters that include radiative corrections [10].

If $G_{E,M}^0$, beside the $G_{E,M}^{p\gamma}$, $G_{E,M}^{n\gamma}$, is known then $G_{E,M}^s$ can be extracted from

$$G_{E,M}^s = G_{E,M}^0 - G_{E,M}^{p\gamma} - G_{E,M}^{n\gamma}. \quad (1.4.2)$$

1.5 Properties of Nucleon near $Q^2=0$

G_E^N and G_M^N can be related to the properties of a nucleon at $Q^2 = 0$. Although, we cannot measure form factors precisely at $Q^2 = 0$, one tries to measure them at Q^2 as close to 0 as possible. Physically, G_E may be attributed to the charge distribution near zero Q^2 . Therefore, $G_E^p(0) = 1$, $G_E^n(0) = 0$ and $G_E^s(0) = 0$ since there is no net strangeness in the proton. Nevertheless, the mean square radius of distribution can be written as

$$\langle r_s^2 \rangle = -6 \frac{dG_E^s}{dQ^2} \Big|_{Q^2=0} \quad (1.5.1)$$

where $\langle r_s^2 \rangle \equiv \int d^3 r r^2 \rho(r)$, $\rho(r)$; probability density

On the other hand, G_M provides information regarding the magnetic moment near $Q^2 = 0$. Accordingly, $G_M^p(0) = \mu_p$ and $G_M^n(0) = \mu_n$. Similarly, $G_M^s(0) = \mu_s$.

1.6 E158 Experiment

Below the E158 experiment is introduced and its physics is summarized briefly.

1.6.1 Introduction and Physics

The E158 experiment is currently being run at Stanford Linear Accelerator Center (SLAC), Stanford. The experiment measures the parity violating asymmetry (Eq. 1.2.1) by scattering polarized electrons from atomic electrons in a hydrogen target. The relevant tree level Feynmann diagrams are shown in Fig. 1.3. The main goal of the experiment is to measure the pseudo-scalar weak neutral coupling, g_{ee} , governing Møller scattering at an average Q^2 of 0.03 (GeV/c)^2 . The relation between the two concepts at tree level is given by [23]

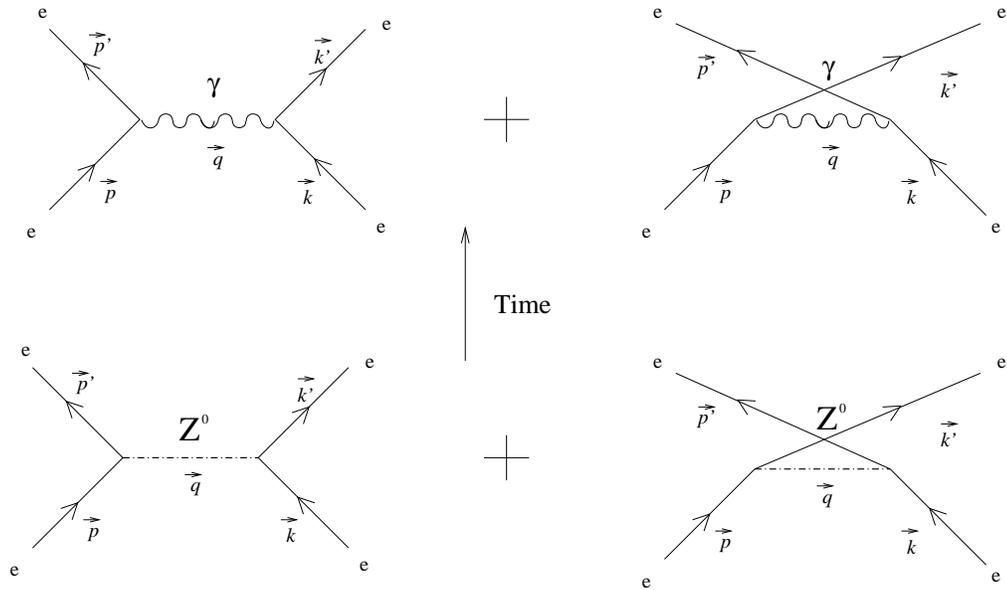


Figure 1.3: Feynmann diagrams of Møller scattering at tree level.

$$A^{PV} = mE \frac{G_F}{\sqrt{2}\pi\alpha} \frac{16\sin^2\Theta}{(3 + \cos^2\Theta)^2} g_{ee} \quad (1.6.1)$$

where m is the electron mass, E is the incident beam energy, G_F is the Fermi coupling constant, α is the fine structure constant and Θ is the scattering angle in the center of mass frame. In the standard model at tree level g_{ee} is

$$g_{ee} = \frac{1}{4} - \sin^2\theta_W \quad (1.6.2)$$

where θ_W is the weak mixing angle.

The experiment, beside testing the standard model at the loop level, is also sensitive to new physics predicted by many extensions of the model. The new physics is comprised of the phenomenon of a new gauge neutral vector boson (Z') [11], contact interactions characterized by the compositeness scale Λ_{ee} [12, 13], and the oblique quantum corrections [14, 15].

Chapter 2

Descriptions of Detectors and Simulations

2.1 Introduction

This chapter covers the E158 detectors, a description of their subcomponents, and simulations carried out in order to build them. We start with an overview of the instrumentation of the experiment briefly. We show the completed detectors first and explain them in detail after that. Finally, simulations related to detectors are covered for the rest of the chapter.

2.2 Overview of E158 Experiment

The instrumentation of the experiment can be divided into four main parts: electron source, accelerator, A-line, and End station A (ESA) (Fig. 2.1 [33]). Longitudinally polarized electrons are produced from a laser-driven photocathode. The

two-mile long linear accelerator (Linac) at SLAC accelerates the electrons to a maximum energy of 50 GeV. The electron beam consists of 400 nsec bunches. At the end of the Linac the beam is steered through an 0.5 and a 24 degree bend in the Beam Switch Yard (BSY) and in the A-line to ESA respectively.

ESA, as shown in Fig. 2.1, houses a target, a spectrometer system and three detectors. The main target throughout the experiment is a liquid hydrogen target. The spectrometer system consists of three dipoles, four quadrupoles and collimators. Two of the detectors were mentioned earlier. The third one is for Mott electrons at the forward angle.

The main purpose of the spectrometer is to focus the electrons onto the detectors and to prevent photons, created after the scattering, from reaching the detectors.

2.3 Møller and Mott Detectors

For the experiment, the medium energy physics group at Syracuse University was responsible for the design and the construction of two detectors: the first one is called a Møller detector (Fig. 2.2 [24]), since it has been used to detect the scattered electrons due to the collisions between the accelerated electrons and the atomic electrons. The other is called Mott detector (Fig. 2.3 [24]), since it has been used to detect the scattered electrons due to the collisions between the accelerated electrons and the protons of the target. Partial three dimensional drawings of both detectors are shown in Fig. 2.4 [25].

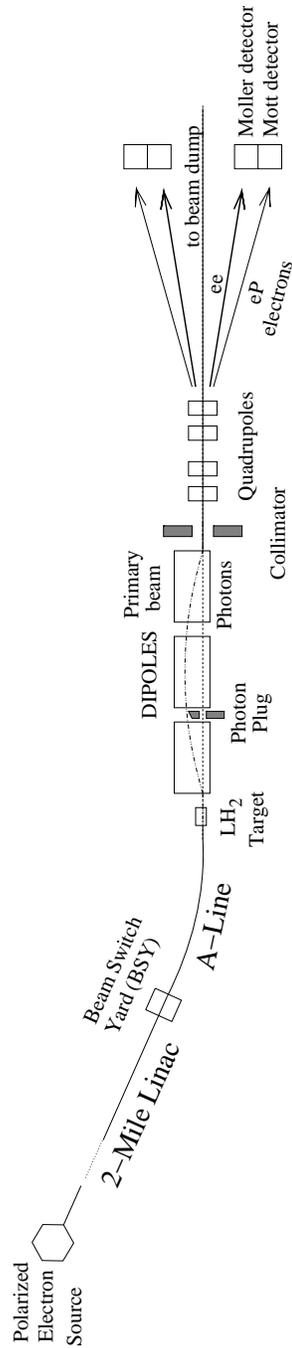


Figure 2.1: The outline of the accelerator at SLAC. Shown only parts relevant to the E158 experiment.



Figure 2.2: Møller detector

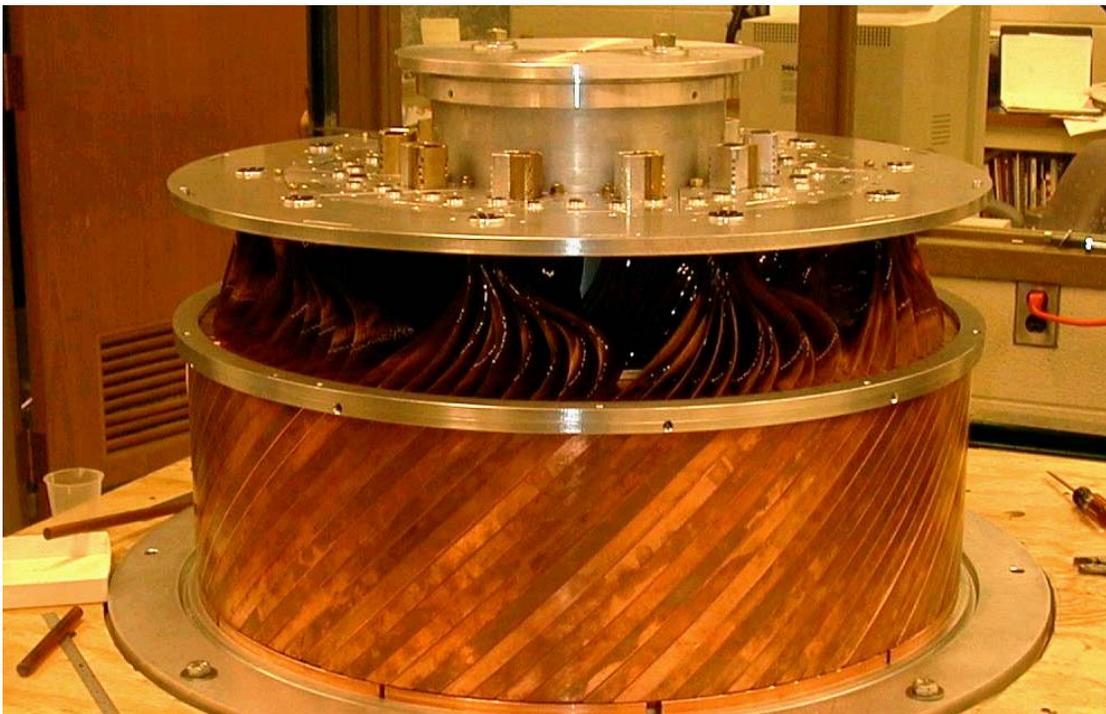


Figure 2.3: Møller and Mott detectors together. However, the Mott detector is shown mainly since it surrounds radially the Møller detector.

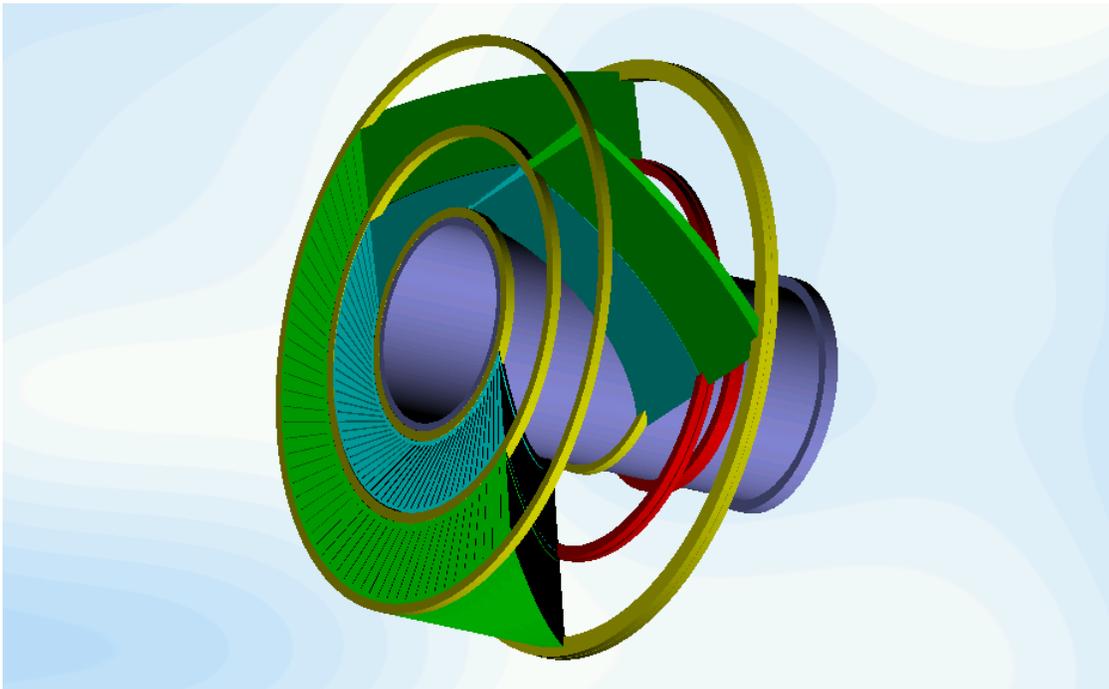


Figure 2.4: Upstream view. Beam pipe (hollow pipe), partially filled Møller (inner tube) and the Mott (outer tube) are detectors shown. The wedges, the sub elements, of the detectors are shown explicitly.

2.4 Møller Detector Design and Description

The Møller detector is a cylindrical tube with the dimensions: $r_{min}=15$ cm, $r_{max}=25$ cm and $\Delta z=25$ cm. The inside of the tube is left hollow so that the beam pipe can pass through it. The detector mainly consists of two interleaved parts: the active medium and the absorber medium. The active medium is used to collect the light created by the scattered particles that enter the detector. As the name implies, absorber medium is the one that interacts the most with the incident particles, and is used to absorb the energy of these particles. For Møller and Mott detectors the active and the absorber medium were chosen to be quartz and copper respectively. The *radiation length* of a material quantifies the energy absorption, and can be defined roughly as the thickness of the medium which reduces the mean energy of a beam of electrons by a factor of e [4]. The absorber medium is chosen from such elements which have small radiation lengths. For example, the radiation length of Cu and Pb is 1.43 cm and .56 cm respectively, whereas it is 866 cm for liquid H₂ and 12.3 cm for fused quartz [26]. Accordingly, the Møller detector is 15.7 radiation length (RL) in depth. How much beam energies is observed in the Møller detector was simulated and therefore, will be covered in the simulations part of this chapter.

The Møller detector consists of 100 identical copper wedges. Each wedge is oriented 45° relative to the beam axis (Fig. 2.5 [25]) and is 1cm thick at the outer surface. The shape of each wedge is complicated. From the front it is a plate bordered by two vertical lines from the sides and two ellipses from the top and the bottom (Fig. 2.6). The ellipses, the intersections of two cylinders and a plane with

the angle of 45° , follow the equation below.

$$\frac{x^2}{2} + y^2 = r^2 \quad (2.4.1)$$

where r is the radius of the cylinder, y is in the radial direction, and x is in the direction perpendicular to the plane. The value of y changes from 10 cm to 25 cm. If the thickness of the detector is t , then the total range of x is $\sqrt{2}t$. In our case, it is 35 cm since $t=25$ cm. A cross section of a wedge of the Møller detector is shown in upper part of the Fig. (2.7) [25]. Quartz fibers are inserted into the 1.5 mm thick slot so that the quartz layers will have 45° angle relative to the beam axis which in turn doubles the light output [29]. In addition, Cu covers with 0.5 mm thickness are also used for mechanical stability. The quartz layers of the detector, consisting of 99 quartz fibers in 0.96 mm diameter, are formed by a bending jig in which the fibers are compressed and glued (Fig. 2.8) [24].

For the ease of handling and mounting ten wedges are combined to form a unit. The free ends of fibers are grouped using semi-hollow Al rings called cookies. The size and the shape of a cookie is designed according to the size of the fiber bundle at hand, and to the location of the fibers in the layer. Fibers are divided into three groups in terms of their locations inside the unit: inner (IN), middle (MID) and outer (OUT). For a unit there are 5 cookies, one for IN, two for MID and two for OUT. Cookies for both detectors are shown in Fig. (2.9) [25]. For every cookie, a photo multiplier tube (PMT) is assigned to integrate the light output. Therefore, 50 PMTs are used for the Møller detector. Cherenkov light produced by the Møller electrons is transferred from cookies to the PMTs by the combination of light guides and mirrors. A sketch of a light guide with the mirror assembly is shown in Fig. 2.11. Light guides are cut cones made of highly polished Al material with high reflection efficiency. For each light guide there are two mirrors used to

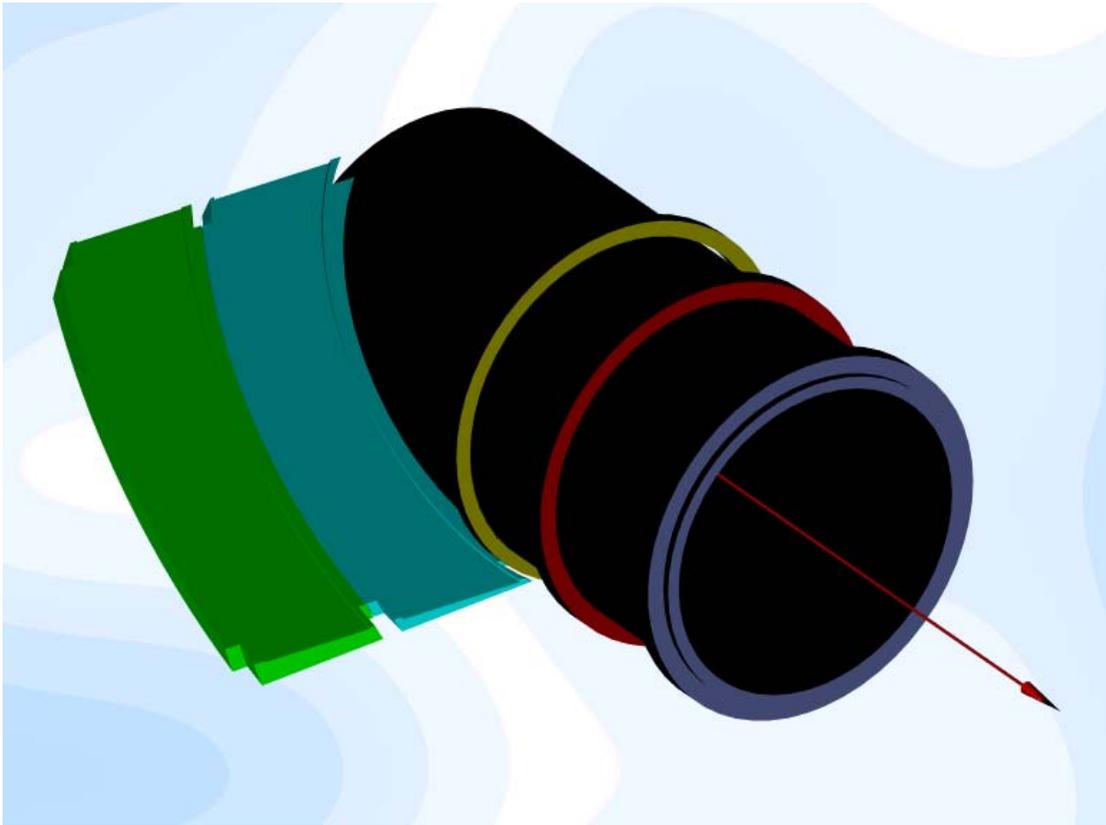


Figure 2.5: Møller (inner) and the Mott (outer) wedges placed on the beam pipe. Central line is the beam line.

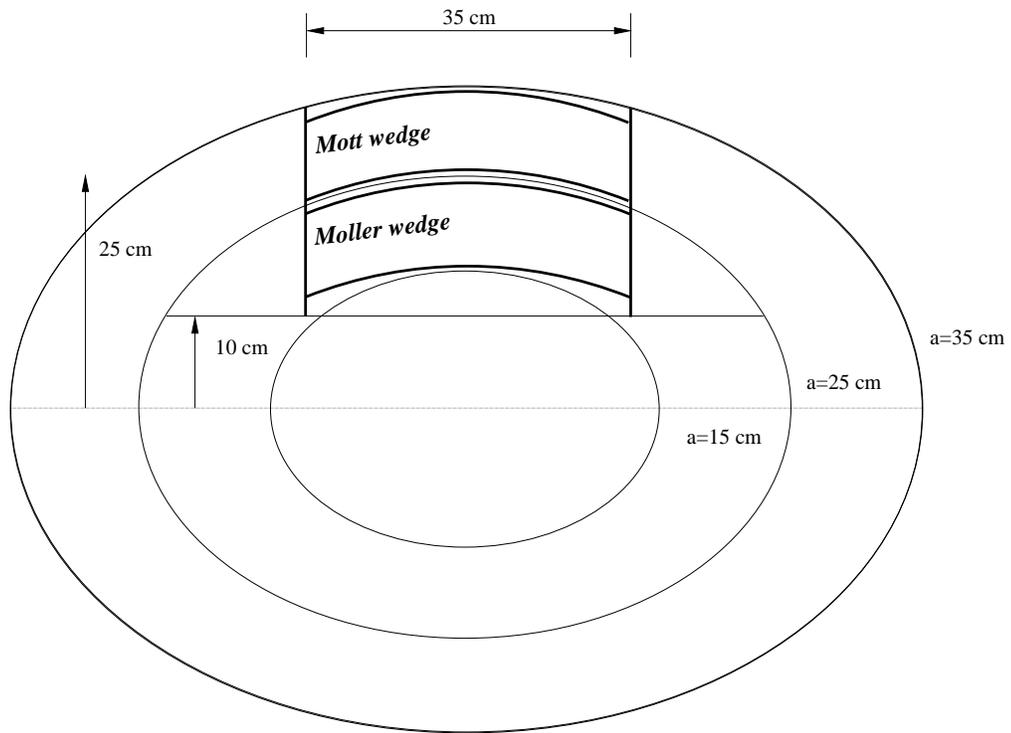


Figure 2.6: The wedges of the Mott and the Møller detectors. The regions left within the bold lines show the slots where the fiber layers are placed.

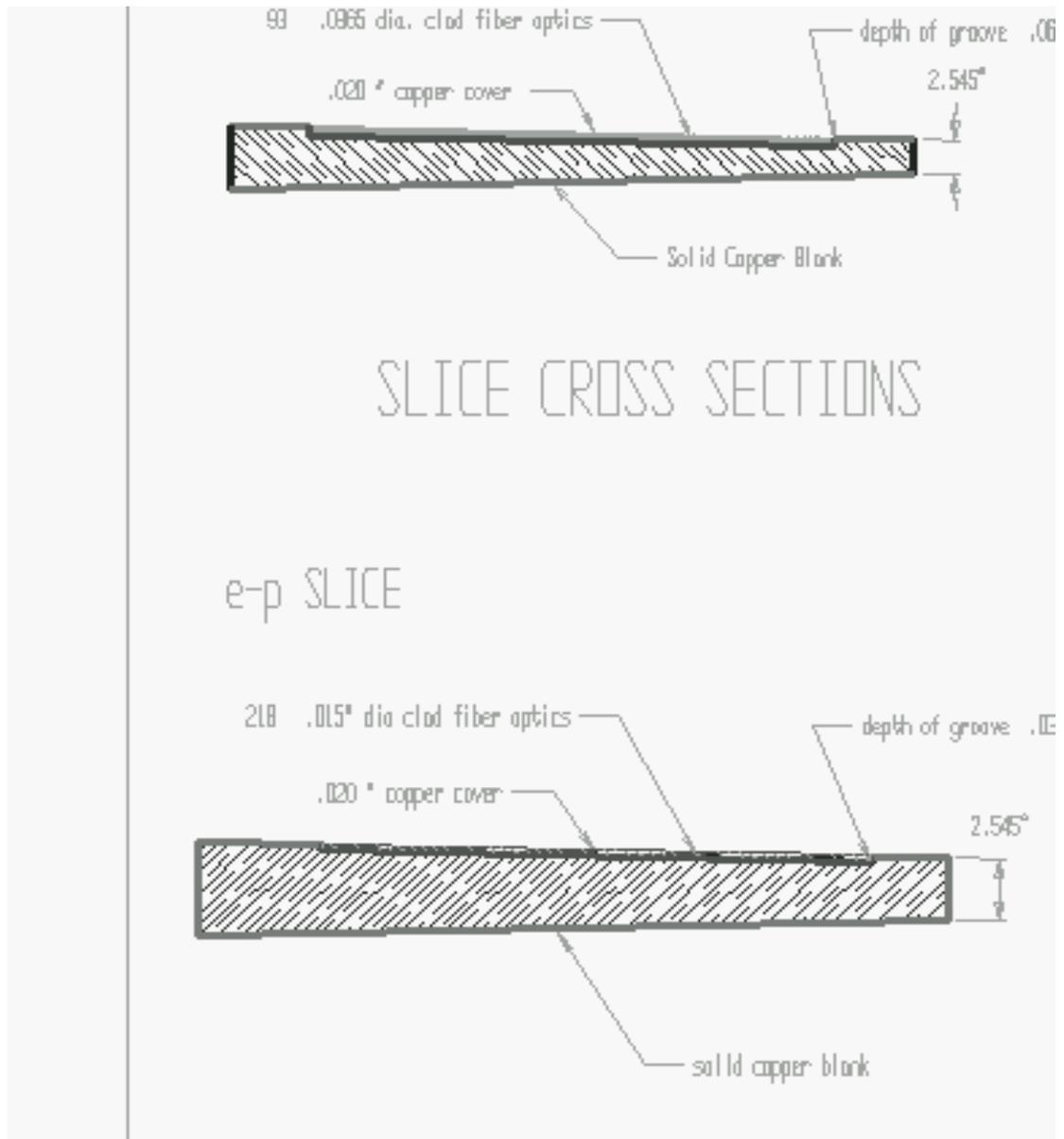


Figure 2.7: Technical drawings of the cross sections of the Møller wedge (upper part) and the Mott wedge (lower part).

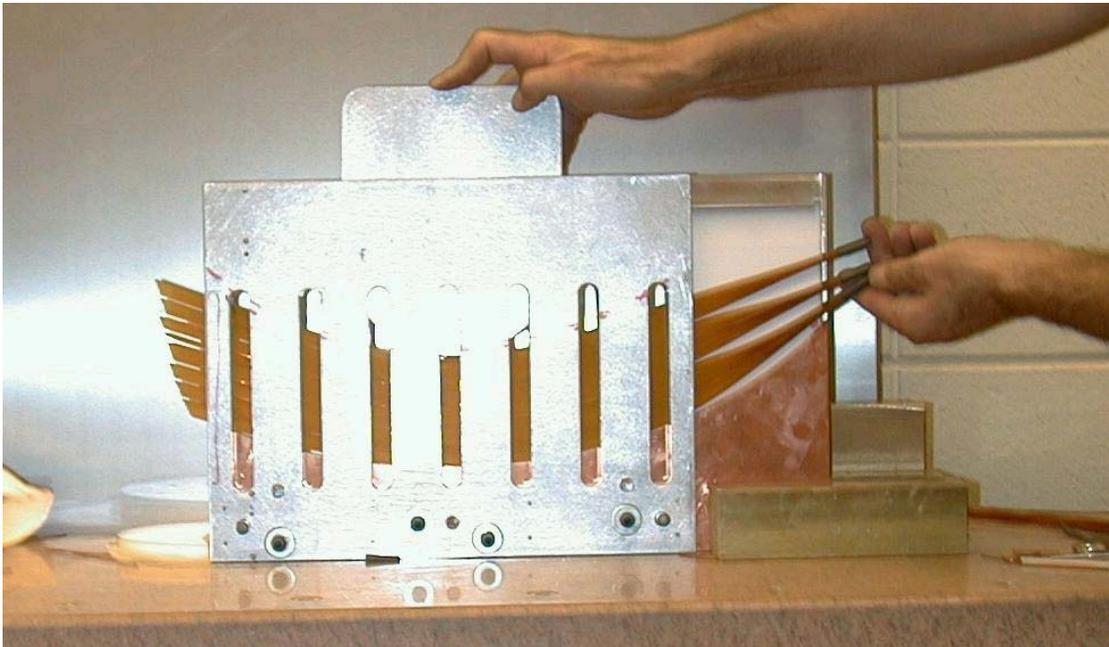


Figure 2.8: Møller fibers bending jig.

direct the light to a PMT: Mirror I is placed between a cookie and a light guide (Fig. 2.12) and Mirror II is placed between the light guide and the PMT (Fig. 2.13). PMTs are used to detect and amplify a light signal so that it can be viewed by oscilloscopes and be digitized by analog-to-digital converters (ADCs). The PMTs used for the detectors are very similar to R2154-02 model shown in HAMAMATSU company's catalogs available online [30] (Fig. 2.10). They are designed to meet the requirements of the task at hand such as fast response, radiation resistance etc.

2.4.1 Mott Detector Design and Description

The eP or Mott detector is quite similar to the Møller detector in terms of the geometry, the materials used and the geometry of wedges except for the dimensions and the amount of materials used. The Mott detector (Fig. 2.3) with dimensions of $r_{min}=25$ cm, $r_{max}=35$ cm and $\Delta z=25$ cm surrounds the Møller detector (Fig. 2.4). The wedges have the same width but differ in thickness (Fig. 2.7). The active material is again quartz in the form of fibers and the density of fibers is one third of that of the Møller detector.

The shape of wedges is quite similar to that of the Møller detector except for the dimensions of the ellipses that borders the wedge from inside and outside. The study of the shape of wedges for both detectors are given in Fig. 2.6.

2.5 Simulations

Simulations are indispensable tools in the design of any nuclear physics apparatus. Here we benefited greatly from simulations in designing the Møller and the Mott

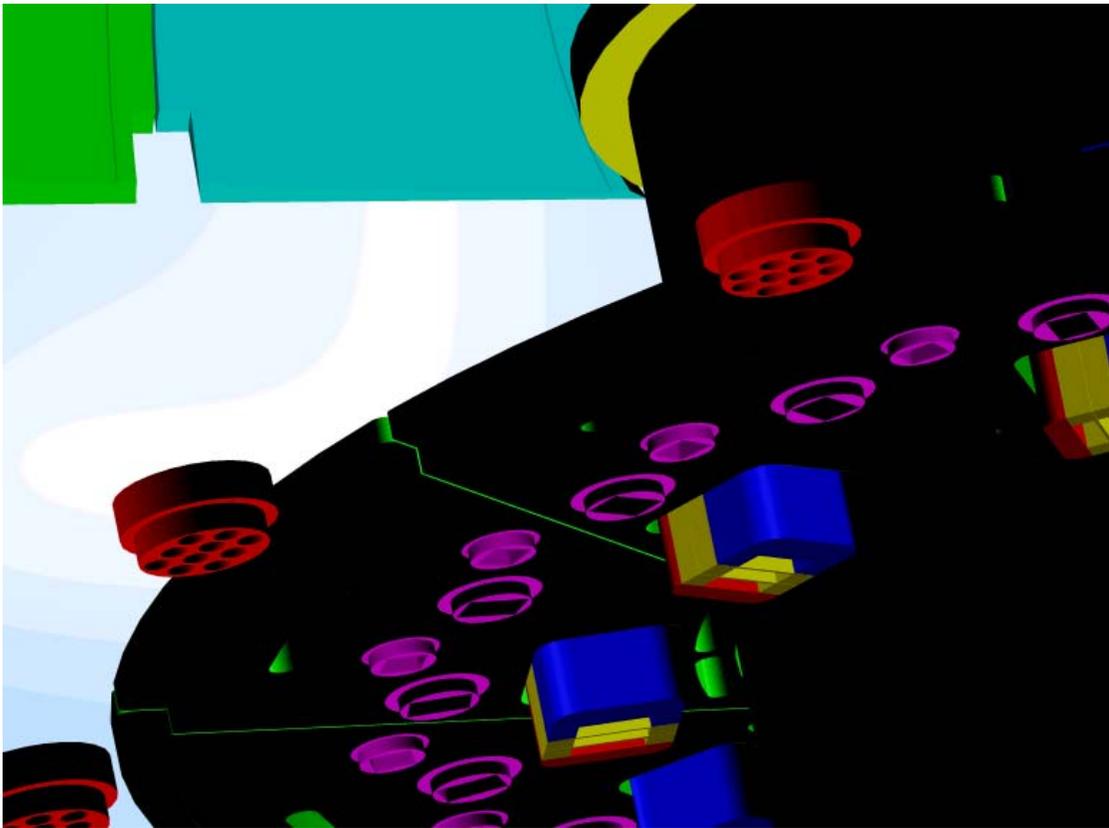
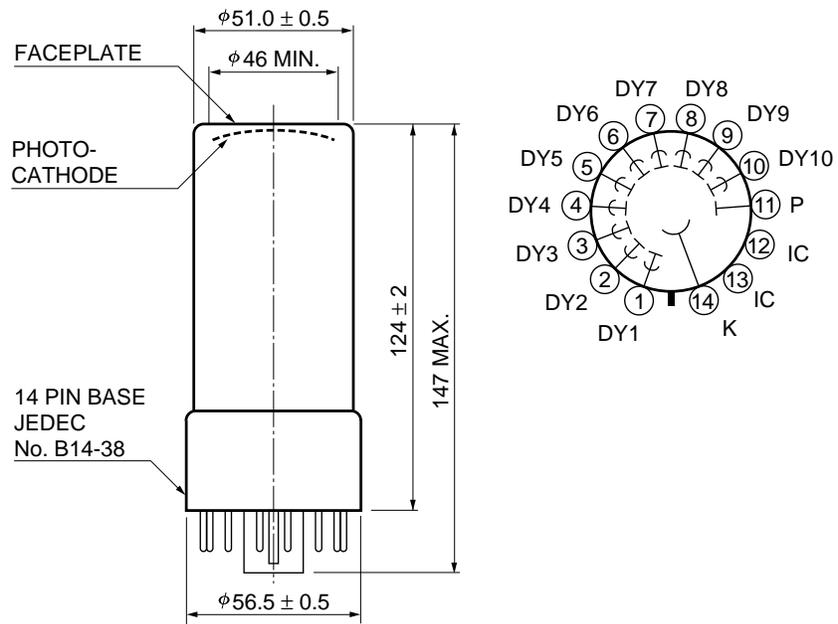


Figure 2.9: Cookies for both detectors. The cookie with many holes is for the fibers from Mott detector and the cookies embedded into Al back plate are for those from Møller detector.

29 R2154-02



TPMHA0296EB

Figure 2.10: The dimensional outline and the base diagrams of the PMTs used for the detectors [30]. (Courtesy HAMAMATSU.)

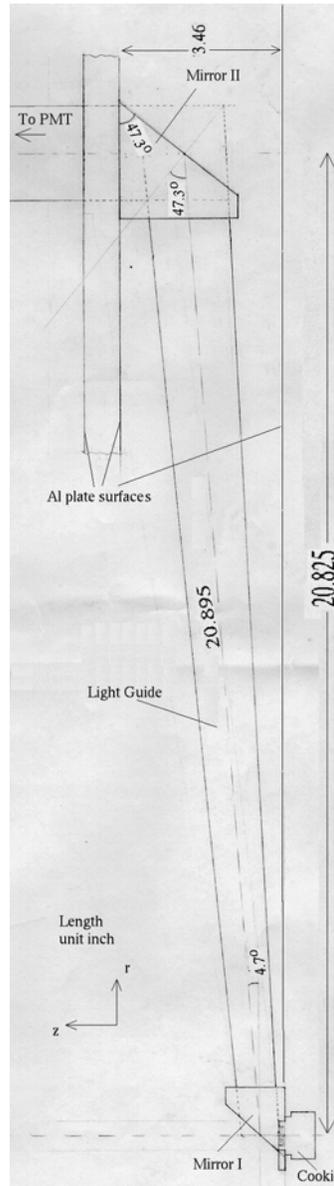


Figure 2.11: A sketch of a light guide and mirrors (side view). Upper left part of the figure is the cylindrical hole in which a PMT is situated. Length unit is inch.

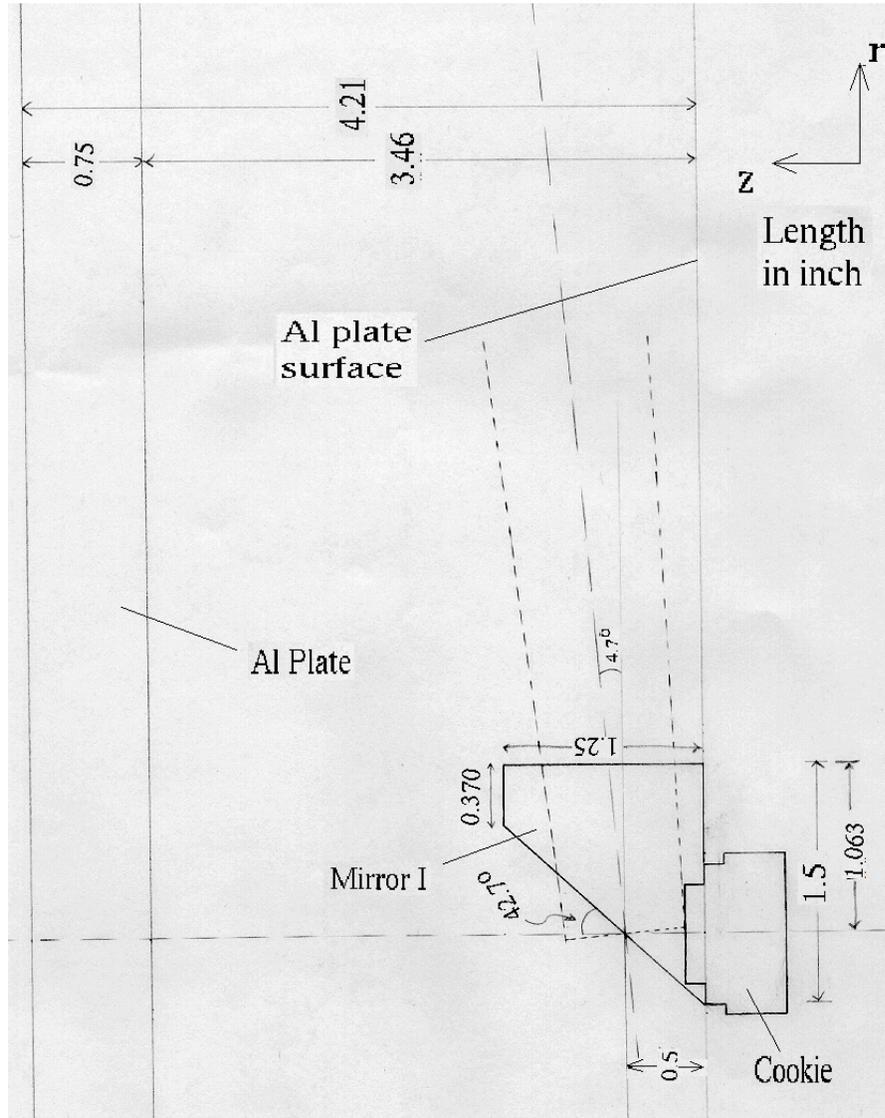


Figure 2.12: A sketch of the Mirror I which connects the cookie to the light guide (side view).

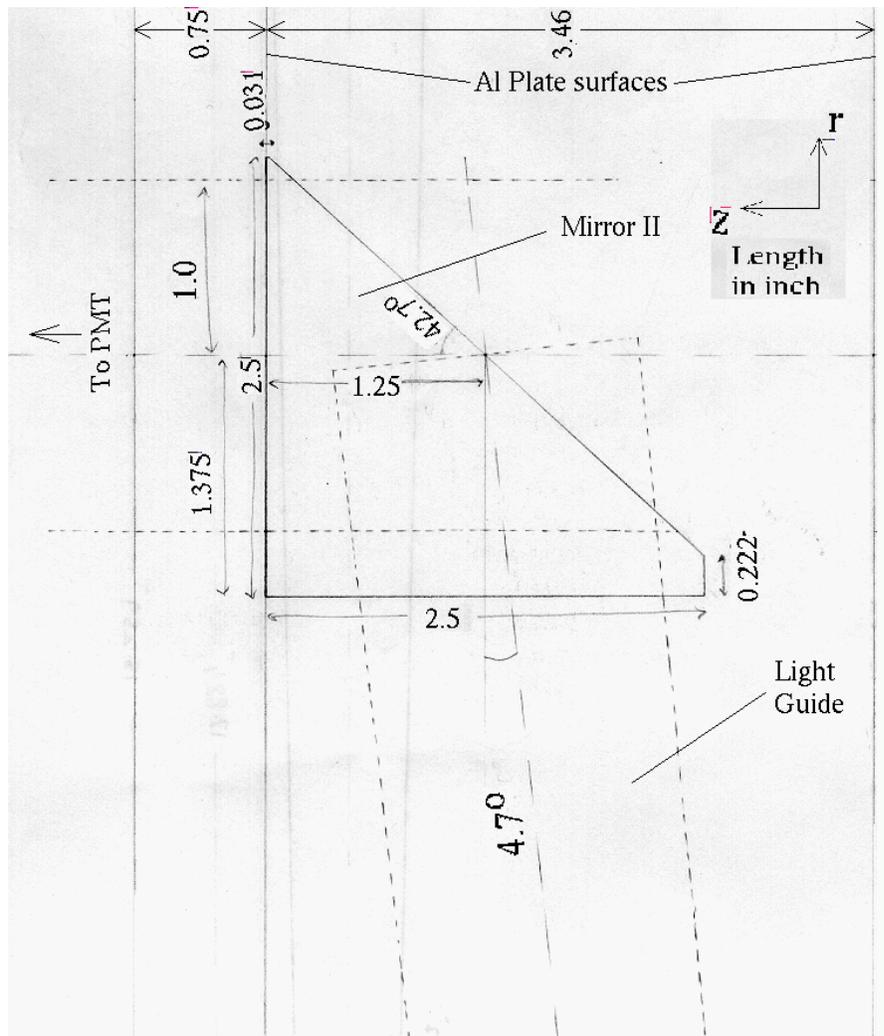


Figure 2.13: A sketch of the Mirror II which connects the light guide to the cylindrical cavity where the PMT is situated. (side view).

detectors. The program we used is called GEANT [31], versions of 3.2111 and 3.2113, which is produced by CERN. In addition, a new computer, DELL pentium III 667 MHz, was purchased and devoted for running simulations at a faster pace. We observed that the new computer saved us time by doing simulations 30-40 times shorter relative to 40-50 MHz servers. This becomes quite essential when high statistics is required for a task.

Our approach toward the simulations was to make them as simple as possible. Trying to accommodate every detail in the simulation would take time, would increase the probability of making mistakes in the code, and would make the results less transparent to draw conclusions.

We made a number of simulations to make sure the Møller detector satisfies the conditions required by the experiment which are [32]:

- Optimal light output for the incident electrons.
- Reasonable resolution $\sigma_E/E \approx 10\%$ in the range from 10 to 25 GeV.
- High tolerance to the radiation.
- Minimal response to other particles.

Simulations for the design of the detectors will be summarized below.

2.5.1 Resolution Studies

Before going to the related simulations, we should know what the resolution of a detector is. It is defined as

$$\text{resolution}(\%) \equiv \frac{\sigma_E}{E} \times 100 \quad (2.5.1)$$

where σ_E is the standard deviation of a distribution of detected light from the particles by the detector, and E is the mean of a distribution of detected light from particles by the detector. Such a distribution is given in Fig. 2.14. The smaller the value the better the resolution is.

A number of simulations have been carried out to study the resolution of the Møller detector. The first simulation involves an optimization of the total thickness of the detector. Fig. 2.15 shows the dependence of the detector resolution to the total Cu thickness at a nominal quartz thickness per layer. Moreover, every point represents a simulation run with 200 events. The geometry of simulation consists of 20 Cu layers and 20 quartz layers. The Cu and quartz layers are placed alternatively throughout the detector, and the beam is normal to them. As seen from the graph, the resolution has a minimum of 4% where the total thickness of Cu is 20 cm.

Although, the second simulation utilizes same geometry and configuration as previous one, this time the quartz thickness per layer is optimized while the nominal value for Cu layer thickness is 1.5 cm. The resolution dependence to the quartz thickness per layer is given in Fig. 2.16. Thus, 0.1 cm thick quartz layers provide us 6% resolution. In addition, increasing the thickness of quartz layer further will give better resolution while, at the same time, will boost the cost of the detector many fold and in turn will make it hardly affordable. Remember that, in actual

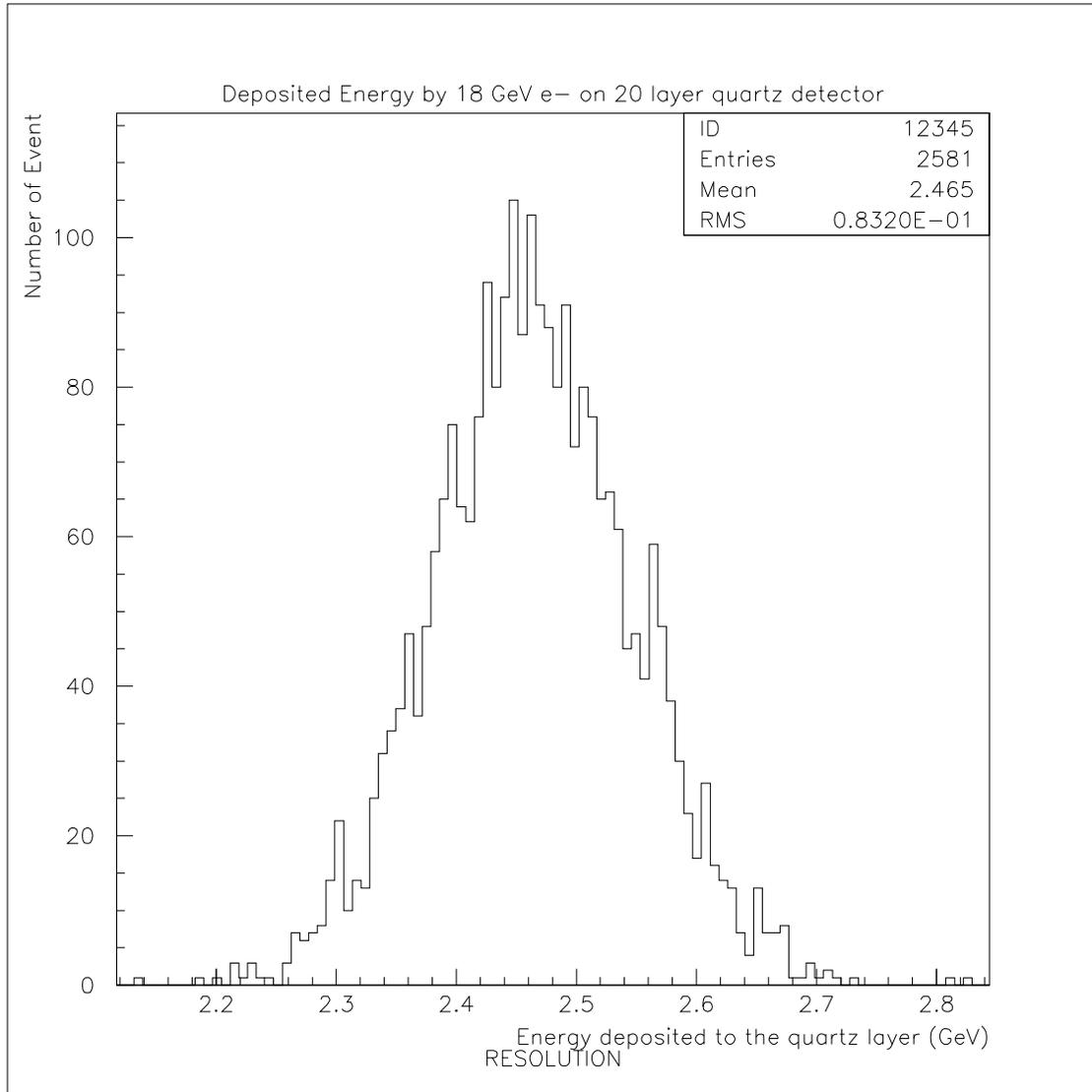


Figure 2.14: The distribution of detected light by the detector by 18 GeV electrons.

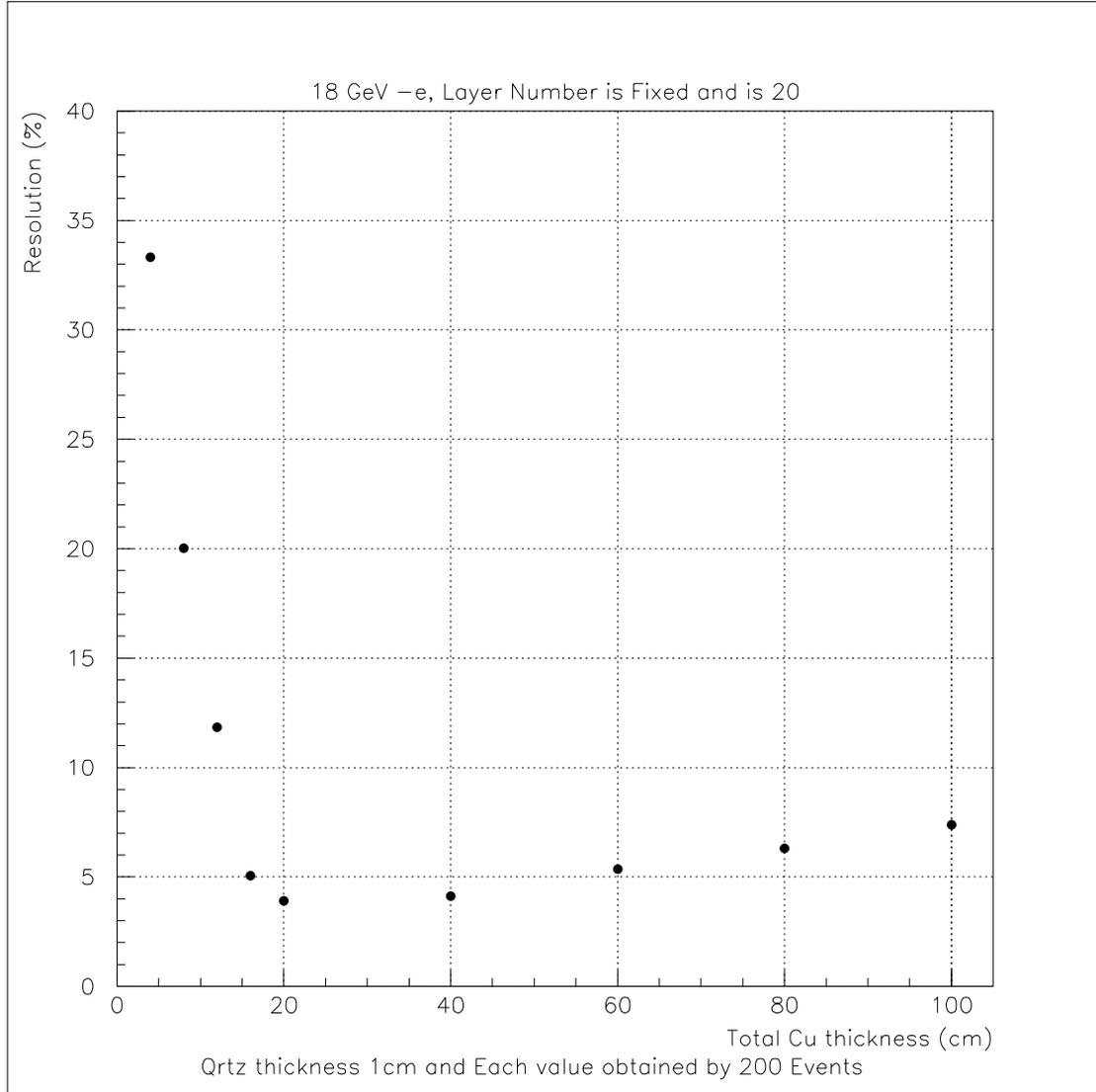


Figure 2.15: Total Cu thickness (cm) vs. resolution (%) while quartz layer thickness is fixed at the nominal value of 1 cm.

design, since the layers make 45° angle with the beam, the effective thickness of the layers will be $\sqrt{2}$ times the actual thickness.

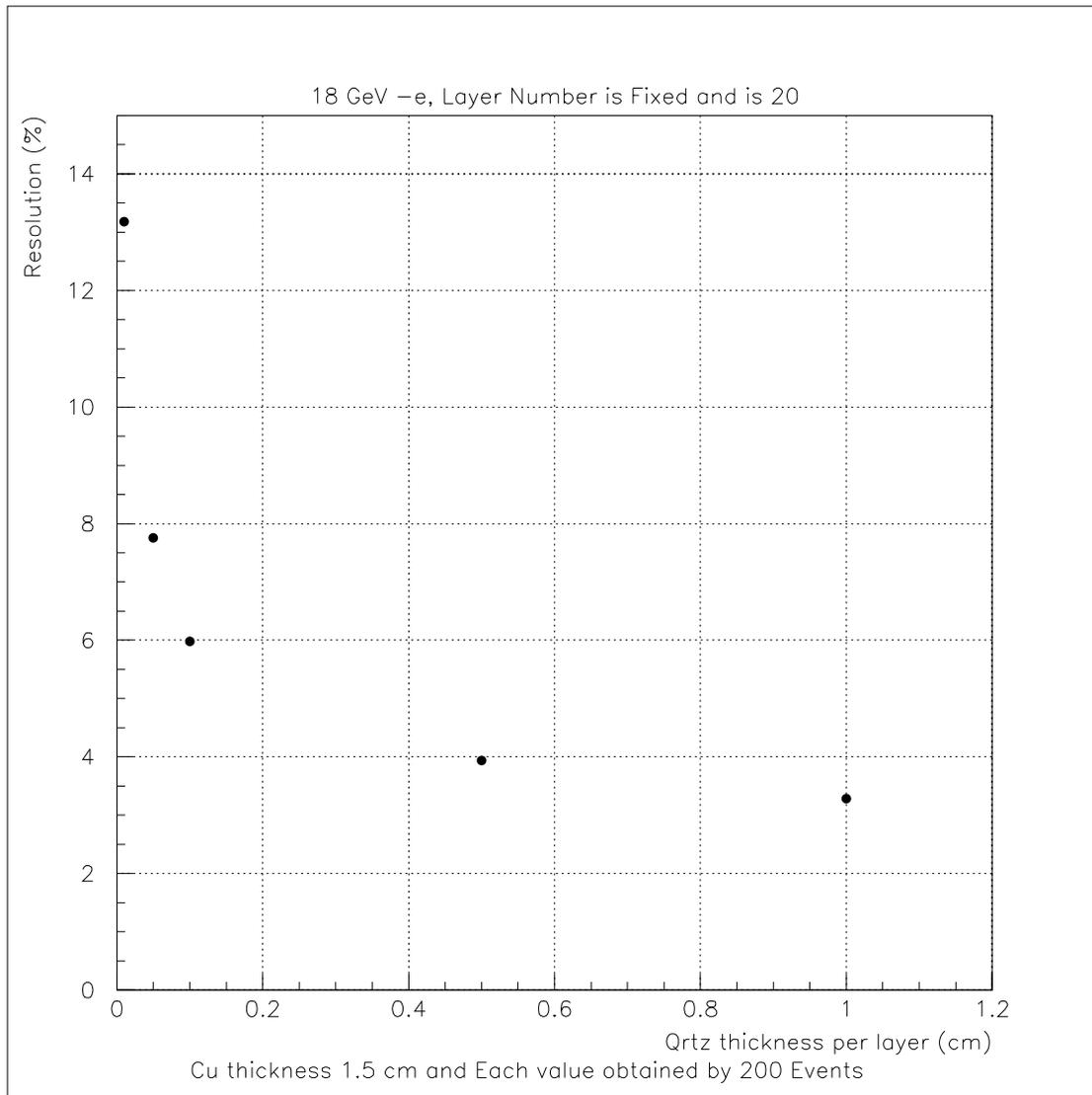


Figure 2.16: Quartz layer thickness (cm) vs. resolution (%) while Cu layer thickness is fixed at the nominal value of 1.5 cm.

The third simulation focuses on optimization of the total number of Cu layers

by keeping both the total Cu thickness plus the quartz layer thickness fixed at the nominal values. Fig. 2.17 gives the relation between the resolution and the Cu thickness per layer. The total length of Cu and quartz layers kept fixed at 24 cm and 1cm respectively during the simulation. We see more or less a linear relationship. The reason is that even though we keep the quartz layer thickness fixed, we have to add more quartz layers as we increase the number of Cu layers to the configuration. So, this causes an increase in the total density of the quartz in the detector which in turn gives a resolution more or less proportional to it.

2.5.2 Cascade Shower Studies

Another simulation topic was to study a shower development, induced by high energy electrons, throughout the Cu medium. Fig. 2.18 shows fractional energy loss per radiation length for 18 GeV electrons. Every point representing 1000 events corresponds to the mean and the standard deviation of the fractional energy loss in the certain radiation length. For example, Fig. 2.19 can give the idea how such distributions look like within the radiation lengths of 5, 6, 7 and 8. According to the first graph i.e. (Fig. 2.18) , the incident electrons lose 12% of their energies which is the maximum at 7th radiation length or 10 cm. Another point is that $\approx 96.0\%$ of energy is deposited up to 16th radiation length.

Lateral cascade shower development was also studied. Fig. 2.20 simulates the lateral shower for 30 GeV electrons entering the Cu medium in z-direction at origin and initiating cascade shower. The numbers in the graph are the total tracks entering in that locality. According to the simulation, we see clearly that the width of the cascade shower is 8 cm (extending from 4 cm to -4 cm) in transverse direction to the beam.

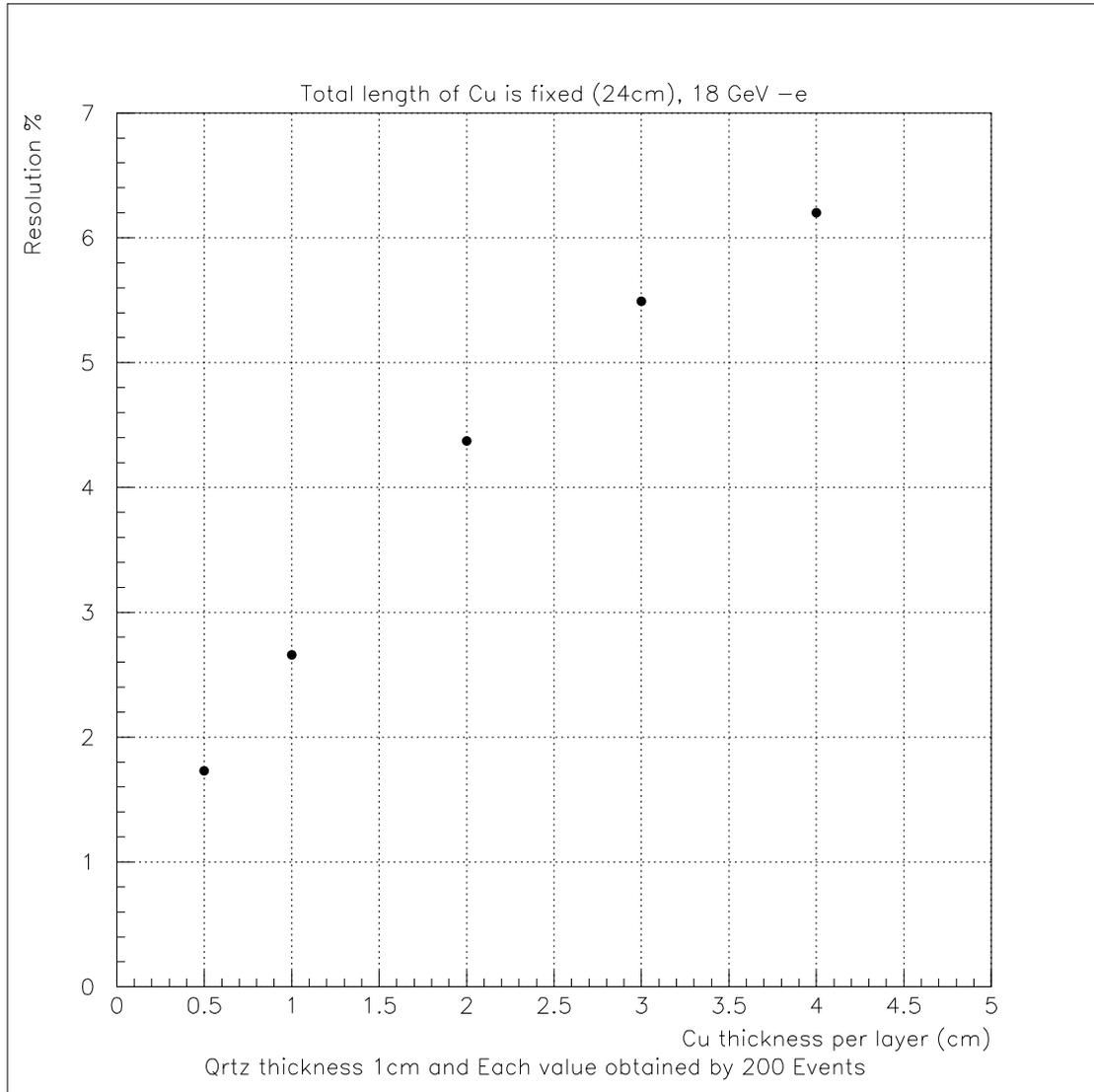


Figure 2.17: Cu layer thickness (cm) vs. resolution (%) while both quartz layer thickness and total Cu thickness are fixed at the nominal values of 1 cm and 24 cm respectively.

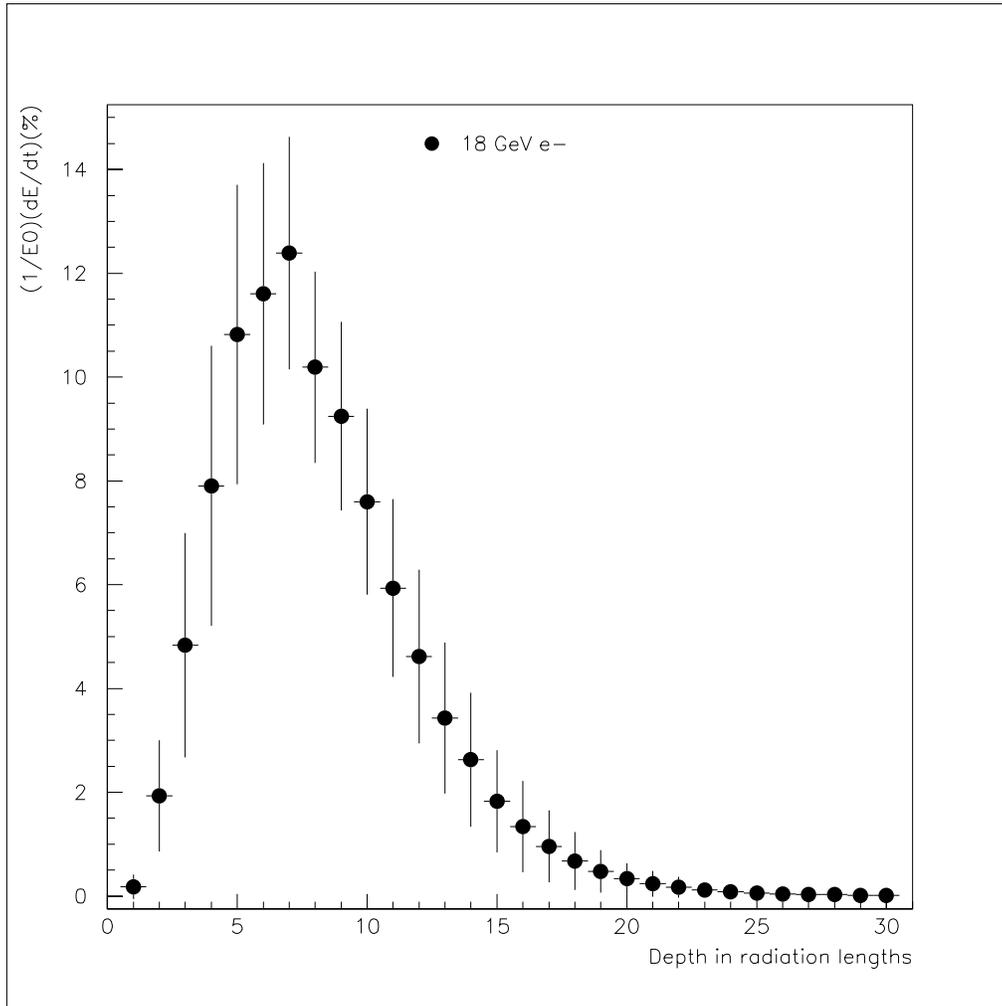


Figure 2.18: Fractional energy loss per radiation length (%) vs. Depth of Cu medium (radiation length)

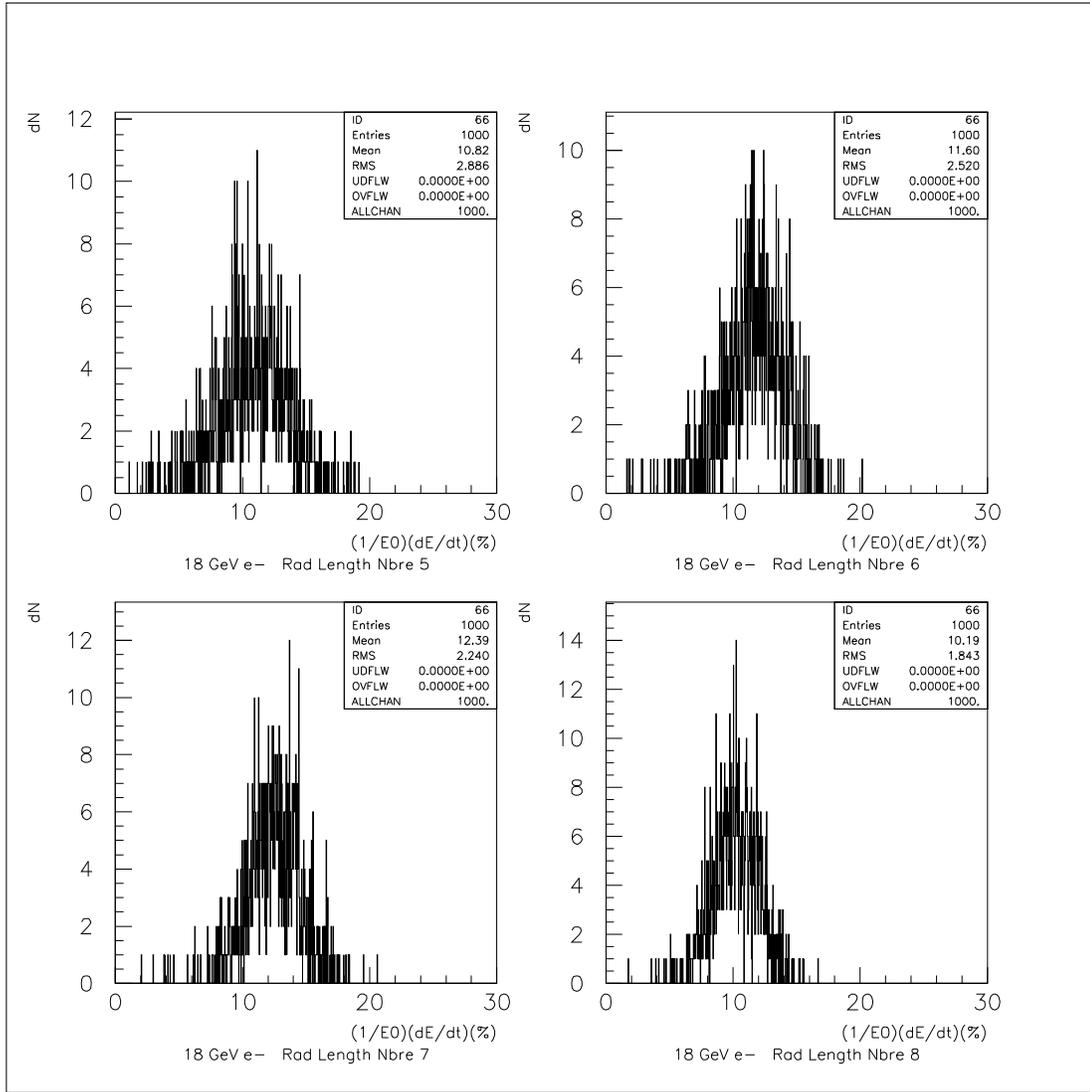


Figure 2.19: Distribution of the number of events vs. Fractional energy loss per radiation length (%) a) top left; within 5th radiation length, b) top right; within 6th radiation length, c) bottom left; within 7th radiation length, b) bottom right; within 8th radiation length.

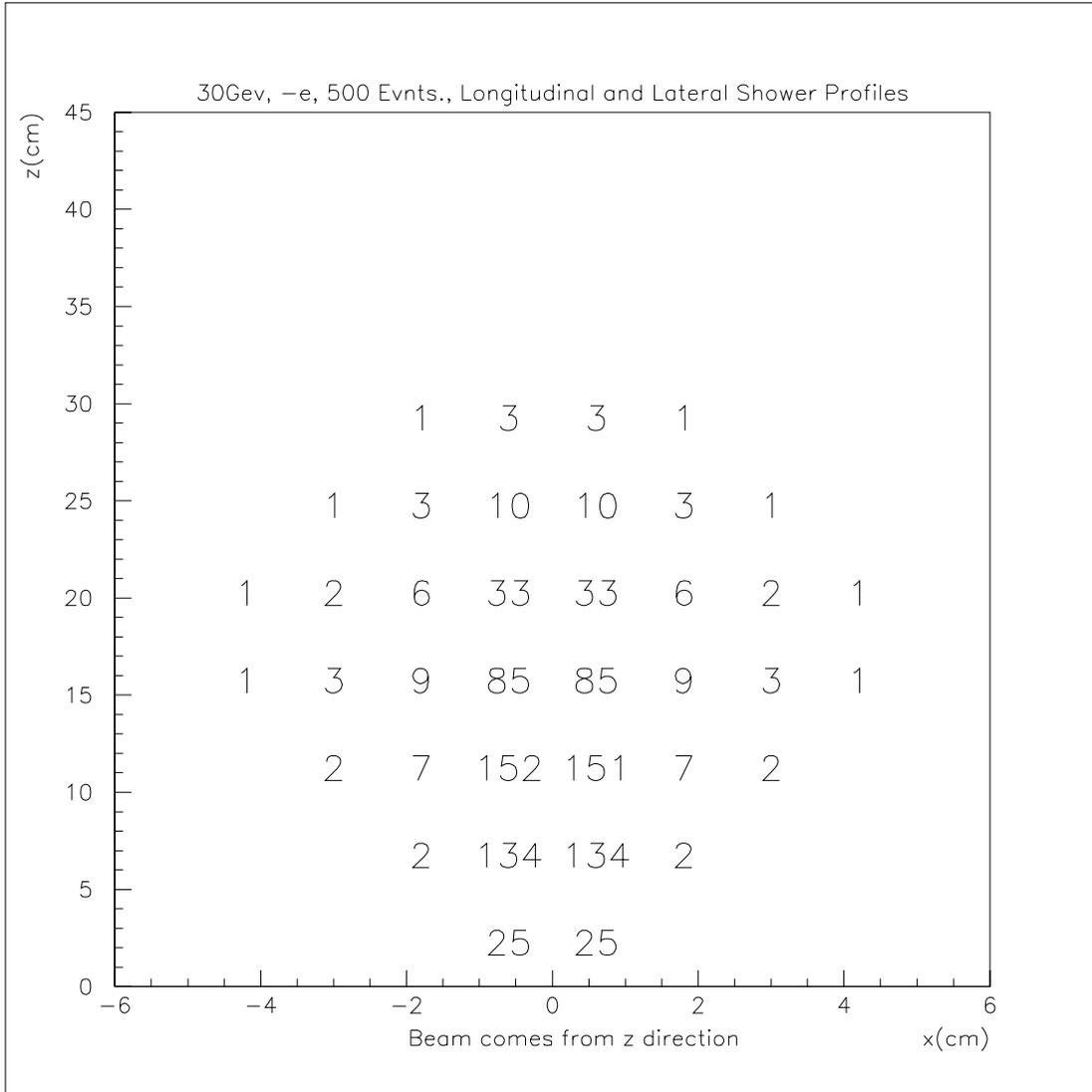


Figure 2.20: Lateral shower development for 30 GeV electrons impinging the medium at origin. Numbers in the graph are believed to represent the total tracks entering in that vicinity.

2.5.3 Simulations related to detectors and fiber bundles.

Simulations in this part study possible interference between detectors by looking detector responses to the initial beam position, and the quartz fiber bundles. The geometry of the simulation was made more similar to real life in order to see such effects. For this, the cylindrical geometry was adopted. A cross sectional drawing of detector package above the beam line is shown in Fig. 2.21. Here vertical and horizontal axes correspond to the radial (r) and beam (z) directions respectively. The region where r goes from 0 cm to 15 cm is empty and is reserved for the beam pipe. The beam line passes through the center of the detectors. Thinner slices, each with .25 cm thickness, are made of quartz, and the thicker ones, each with 2.25 cm, are made of Cu in the detectors. Also, behind the Møller detector, 4 quartz slices, with 3.5 cm from each other, are used to simulate fiber bundles. Furthermore, there is a 2 cm thick Cu tube which serves as a shield between two detectors.

The responses to electron beam

The beam sent to the detectors consists of 18 GeV electrons. In addition, again for being close to the real life situation, the beam coordinates are randomized which means that radial and angle coordinates initially are different for every event. In the simulation, such events are sent to detector surfaces within a 1 cm thick region in radial direction and the corresponding total deposited energy to the quartz layers are recorded for every event up to 1000 events. After that the code figures the mean value of the event population and the error accompanied by it. This continues until the Møller and the Mott surfaces are swept. Since the total radius of both detectors goes from 15 cm to 35 cm there are 20 data points as total.

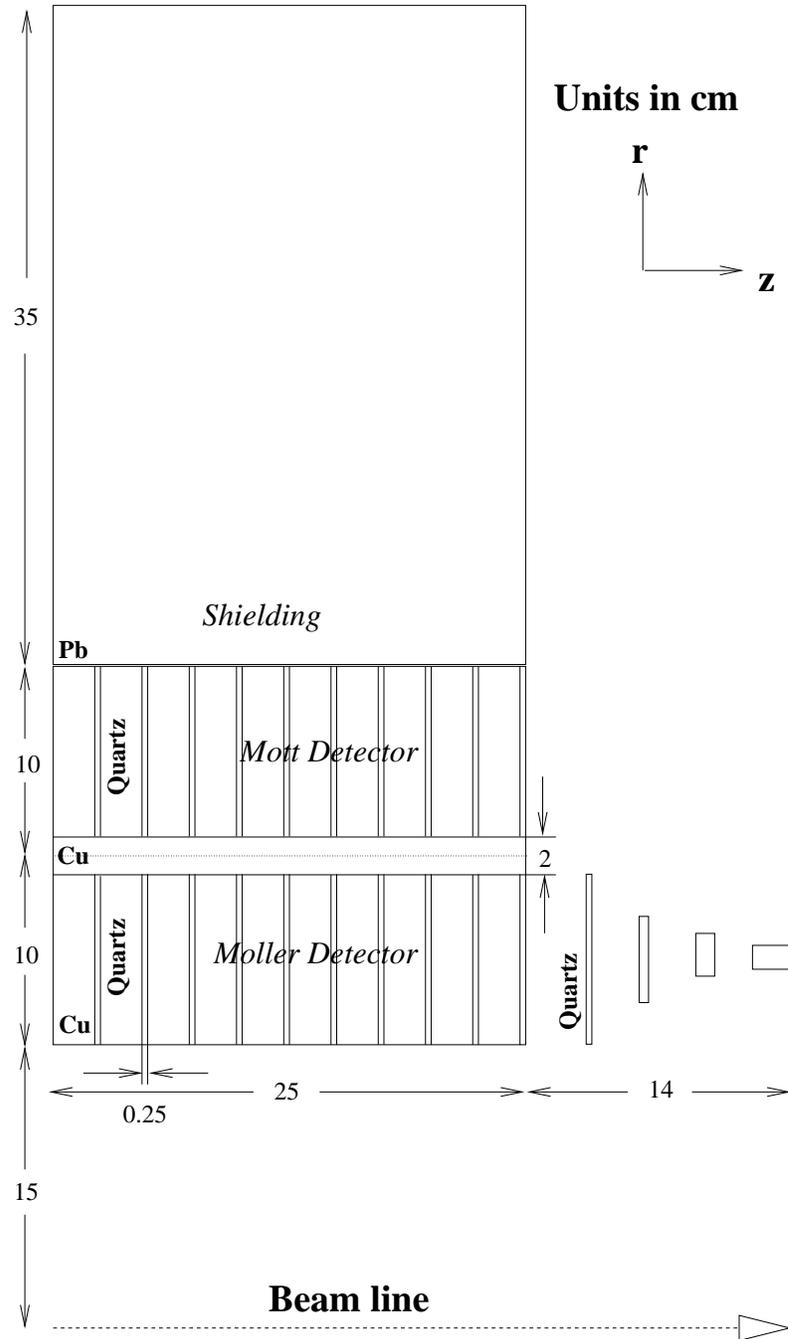


Figure 2.21: Drawing of the cross section of detectors above the beam line.

Fig. 2.22 shows how the total energy deposition depends on the initial location of the beam in radial direction. The first graph from the top left uses data points taken by the Møller detector. We see that the energy deposition averages about .4 GeV for the first half which corresponds to the beam on the Møller detector surface. In addition, it drops down sharply to 17 MeV where the position of the beam is between 25 and 26 cm since this is where the beam begins to hit to the Mott detector. From that point, the energy deposition in the Møller detector comes from the Mott detector. In this way, we can check if there is any mutual mixing between the detectors. According to the graph, the total energy deposited from the Mott region to the Møller detector is less than 1%. Of course the assumption is that the beam intensity is the same everywhere on the surface. According to a simulation that shows the distribution of electrons through the Møller and Mott scatterings (Fig. 2.23 [27], Fig. 2.24 [28]), Møller electrons outnumber the Mott electrons; therefore, the figure given above for the ratio is subject to a further suppression. The second graph from the top right in the same figure uses data points taken by the Mott detector this time. It also constitutes a sort of self check for the sanity of the simulation. In the graph, we see an opposite behavior as compared to the previous one while raising the radial coordinate of the beam, which is expected. Since the beam is sent to the Møller detector in the first half of the data, the total energy deposition in the Mott detector is quite low and ranging from .6 to 19 MeV. Once the beam starts to hit the Mott detector, it picks up sharply to .46 GeV and stays till the end of the data. Again the total energy deposited in the Mott detector through the Møller detector is about 1%. The last graph from bottom left in the figure uses data points taken by the quartz layers behind the Møller detector. The first data point is about the double of the next one in the graph. The reason is that the first point is obtained while the beam is hitting to the

lower edge of the Møller detector. This means that the induced shower particles can leave easily the Møller detector volume and can deposit energy directly to the visible part of quartz layer which is across the beam line. We see a slow but linear increase followed by a gradual decrease and a local maximum of 32 MeV in between for the first half of the data in the graph where the energy deposited in the quartz layers comes from Møller detector medium. In addition, we see a slow but linear decrease ranging from 5 to .9 MeV. Moreover, the total energy deposited in the quartz layers through the Mott detector is a bit more than 11% of what is deposited through the Møller detector. This figure gives us some understanding about the contribution of the radiation coming from behind the Møller detector to the fibers since in reality this is the region where the extension of the fibers coming from inside the Møller detectors are located in the form of fiber bundles. Energy contributions from the Mott detector to the fiber bundles of the Møller detector will degrade the sampling of the shower in the Møller detector at some level.

The responses to the photons

We also did simulations related to possible photons due to synchrotron radiation, that come to the detectors. The responses of the detectors and the fiber bundles behind the Møller detector to photons are studied. The techniques and the geometry used for photons are the same as the ones used for electrons above (Fig. 2.21). Fig. 2.25 shows the energy deposited in the detectors and the quartz layers behind the Møller detector separately by the 10 MeV photons. The plots follow more or less the similar patterns as in the Fig. 2.22. According to the plots if the detector surfaces are bombarded by 10 MeV photons, then less than 1% of the energy is deposited in each detector and 0.02% of the energy is deposited in the

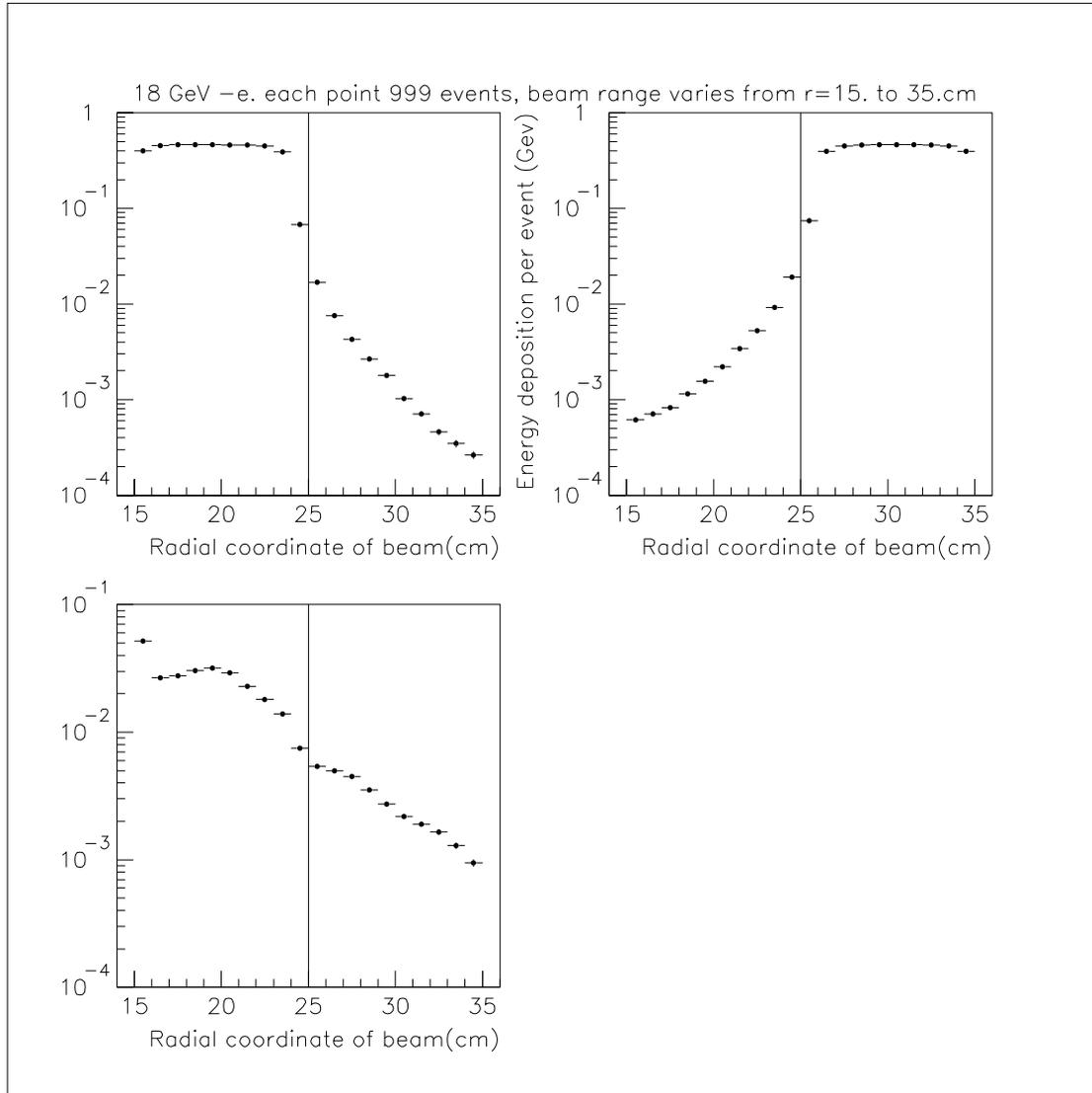


Figure 2.22: The total energy deposited by 18 GeV electrons to the Møller detector (top left), to the Mott detector (top right) and to the quartz layers (bottom left) behind the Møller detector as a function of initial beam location. Vertical lines in the graphs are drawn to show the border between the Møller and the Mott detectors in radial direction.

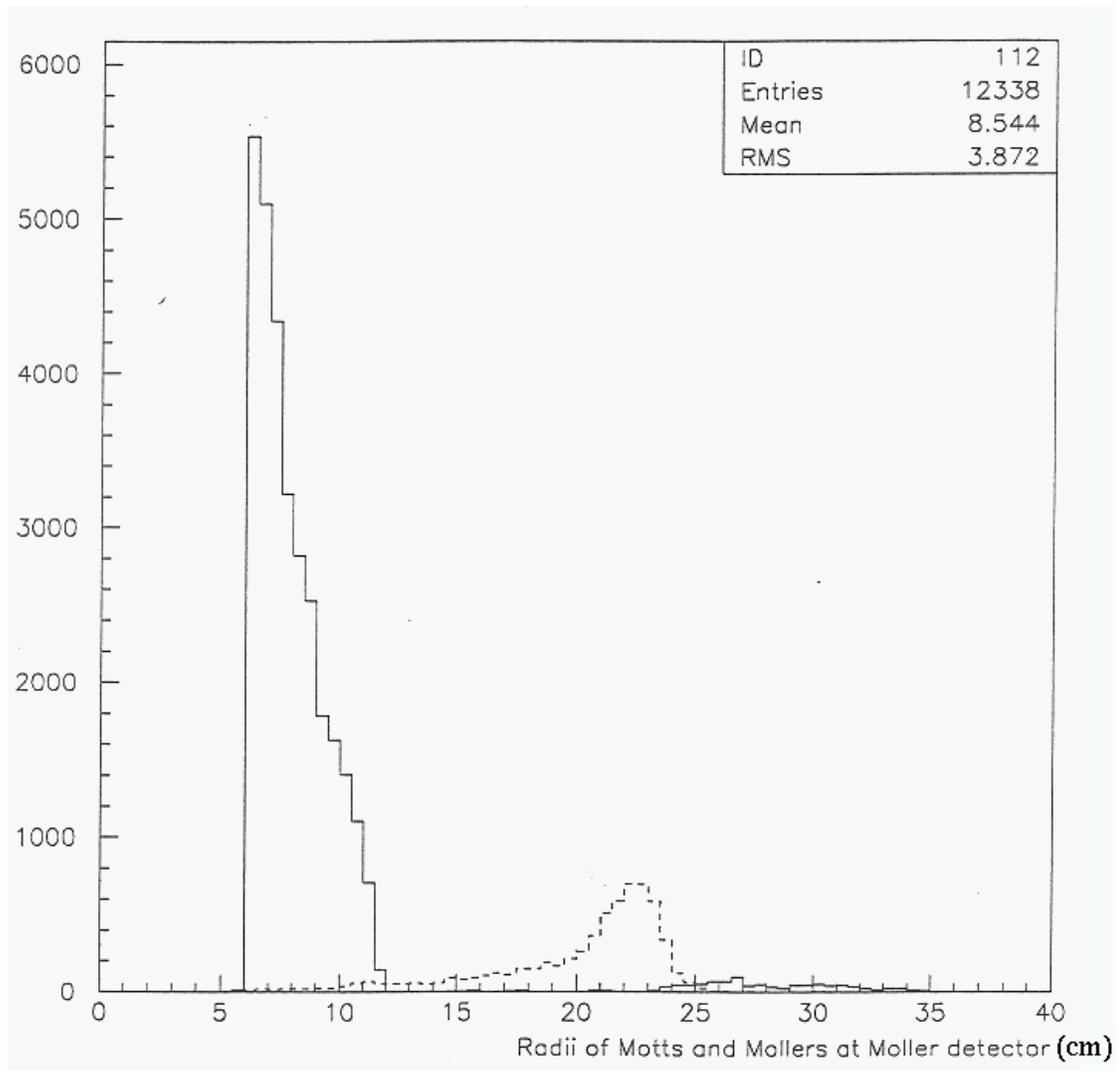


Figure 2.23: Simulation result that shows the radial distributions of outgoing electrons at the detector region. The first and the third peak or rather the wide bump are the distributions of the Mott electrons, *i.e.* the electrons scattered by the protons in the target. Second peak with dashed lines is the distribution of the Møller electrons, *i.e.* the electrons scattered by the orbital electrons in the target.

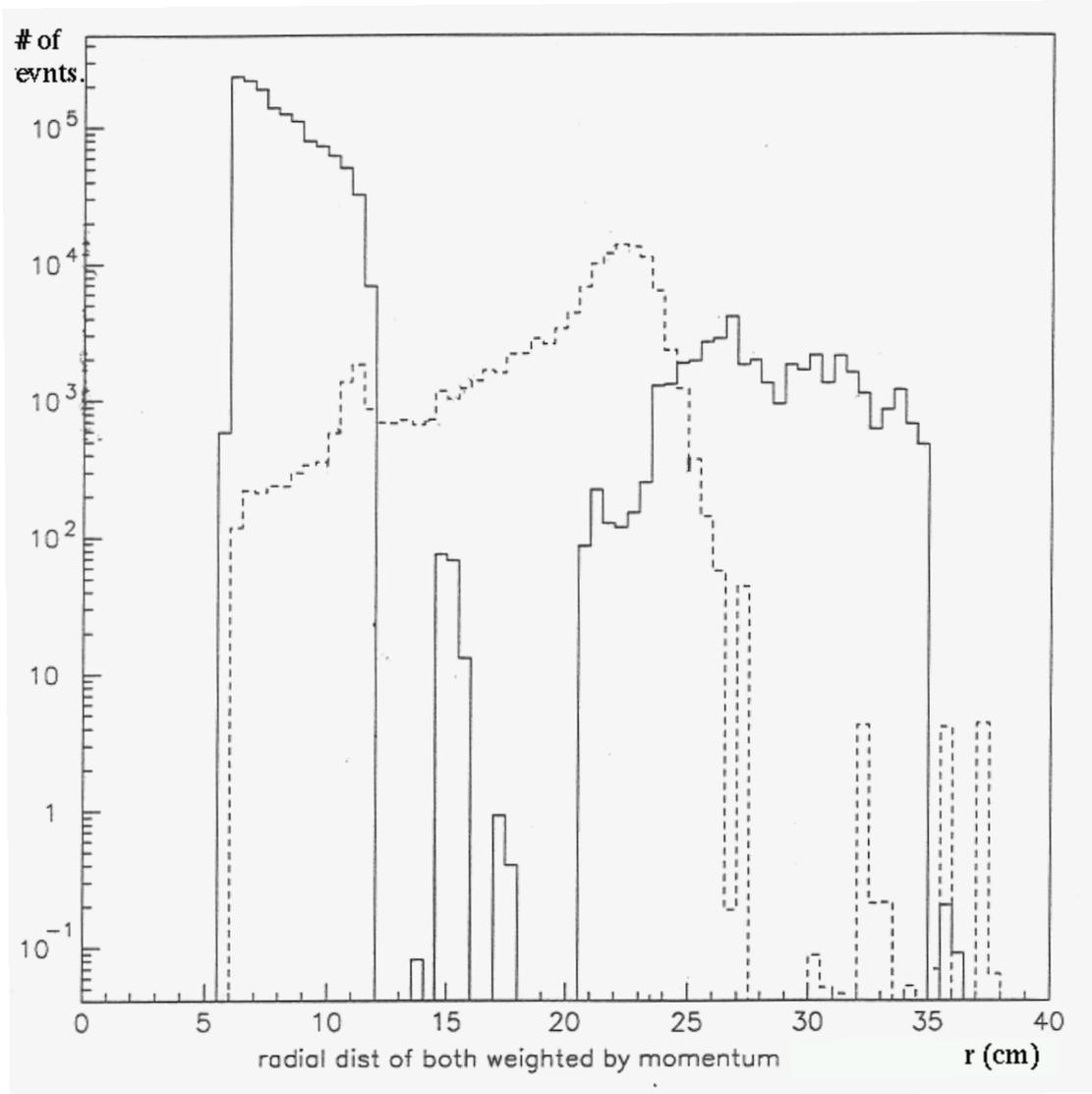


Figure 2.24: Simulation result that shows the radial distributions of outgoing electrons, weighted by their momentum, at the detector region. The first and the third peak are the distributions of the Mott electrons. Second wide peak with dashed lines is the distribution of the Møller electrons. The vertical axis is in logarithmic scale.

quartz layers behind the Møller detector. The total energy deposited in quartz layers through the Mott detector is less than 2% of what is deposited through the Møller detector in this case. The total energy deposited in the quartz layers by the 10 MeV photons is about 0.01% relative to the total energy deposited by 18 GeV electrons.

Other simulations were also carried out to determine how to suppress the contributions of the photons. For example, 3 radiation length of Carbon was put in front of the detectors in order to absorb photons (Fig. 2.26). Fig. 2.27 compares the energy depositions by the 10 MeV photons to different geometries. While one geometry has no C preradiator, the other has 3 radiation lengths of C preradiator. The upper plot in the figure shows the improvement factor, the ratio of deposited energies from the two geometries, as a function of the initial beam location if the energy is drawn by the Møller detector. Lower plot in the figure shows the improvement factor if the energy is drawn by quartz layers. We see average improvement by a factor close to 10 from the upper plot while the beam is on the Møller detector radially. When the beam is radially on the Mott detector it is worse by 14%. However, the improvement factor increases by 44% (decreases by 18%) if the beam is radially on the Møller detector (the Mott detector) for the case in which the energy deposition is drawn by the quartz layers. Meanwhile, one should look at how much the preradiator affects the energy depositions by the electrons. Fig. 2.28 shows the improvement factors in the Møller detector and in the quartz layers for the 18 GeV electrons. According to the upper plot, the energy deposition in the Møller detector directly by the beam decreased by 20%. However, the energy deposition in the Møller detector while the beam is radially on the Mott detector increases by 9%. In addition, according to the lower plot, the energy deposition in the quartz layers through the Møller detector is suppressed by a factor of 2.3.

Similarly, the energy deposition in the quartz layers through the Mott detector is suppressed by a factor of 2.4. It was understood that the preradiator in 3 radiation length corresponding to a thickness close to 60 cm did not impact on the improvement factors significantly except for the case of photons impinging on the Møller detector surface. Therefore, the idea of installing the carbon preradiator was not pursued.

2.5.4 Mapping out the Radiation Level and Shielding Studies

To know the radiation levels behind the detectors is important especially for the photo multiplier tubes (PMTs) which will be positioned in that region. There are two reasons. First, the tubes may be damaged if the exposure to the radiation reaches the critical level where they cannot function properly anymore. Second, unwanted signals are likely to be produced in the PMTs as a result of high radiation. Therefore, they are to be placed where the radiation level is as low as achievable. Typically, the radiation at tubes should be less than 0.1 MRad [29]. Proper shielding will help suppress the radiation further. Therefore, we need to find out both the location where the radiation is minimum and the proper shielding.

The first simulation focuses on mapping the radiation levels behind the detectors. The cross section of the cylindrical geometry used in the simulation is given in Fig. 2.29. The geometry consists of 2 Cu tubes, 2 Pb tubes and 10 Cu rings. The two Cu tubes representing the Møller and the Mott detectors have the same thicknesses, 10 cm in radial and 25 cm in z or beam line direction. The two Pb tubes are used for shielding from the front and the back in order to isolate the inside region

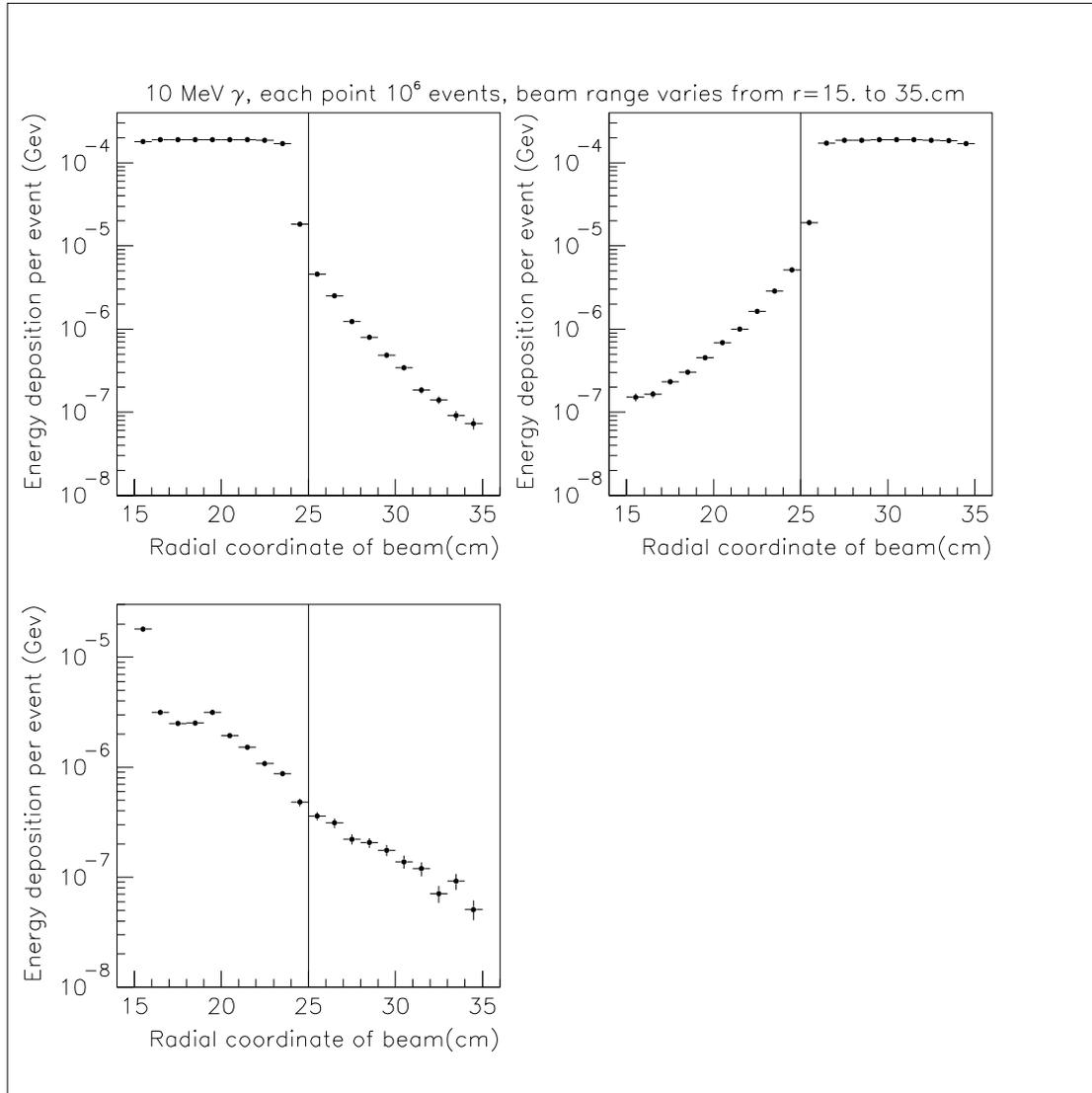


Figure 2.25: The total energy deposited by 10 MeV photons in the Møller detector (top left), in the Mott detector (top right) and in the quartz layers (bottom left) behind the Møller detector as a function of initial beam location. Vertical lines in the graphs are drawn to show the border between the Møller and the Mott detectors in radial direction.

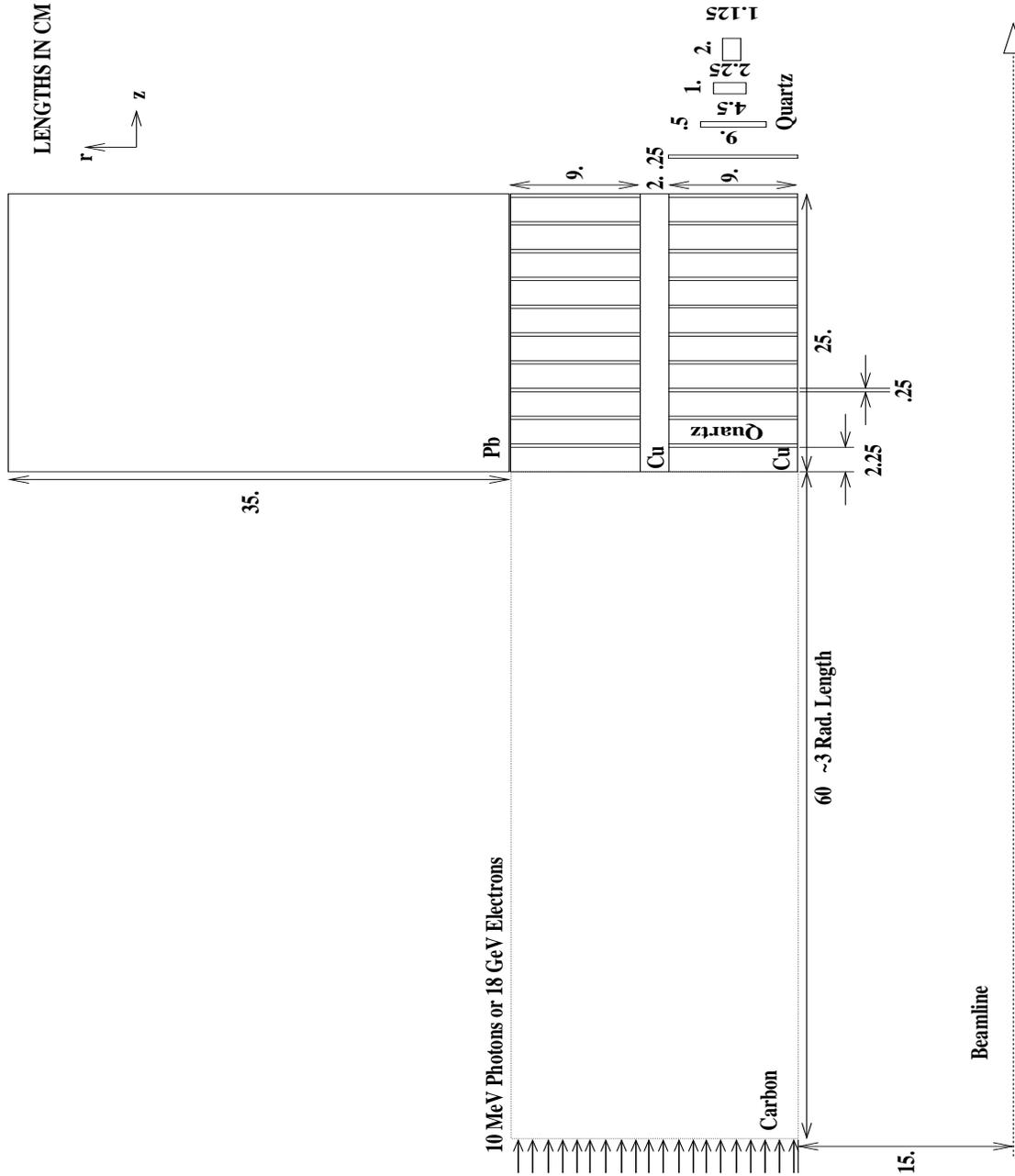


Figure 2.26: The cross-section of cylindrical geometry above the beam line in the case where 3 radiation length of carbon is placed at the front.

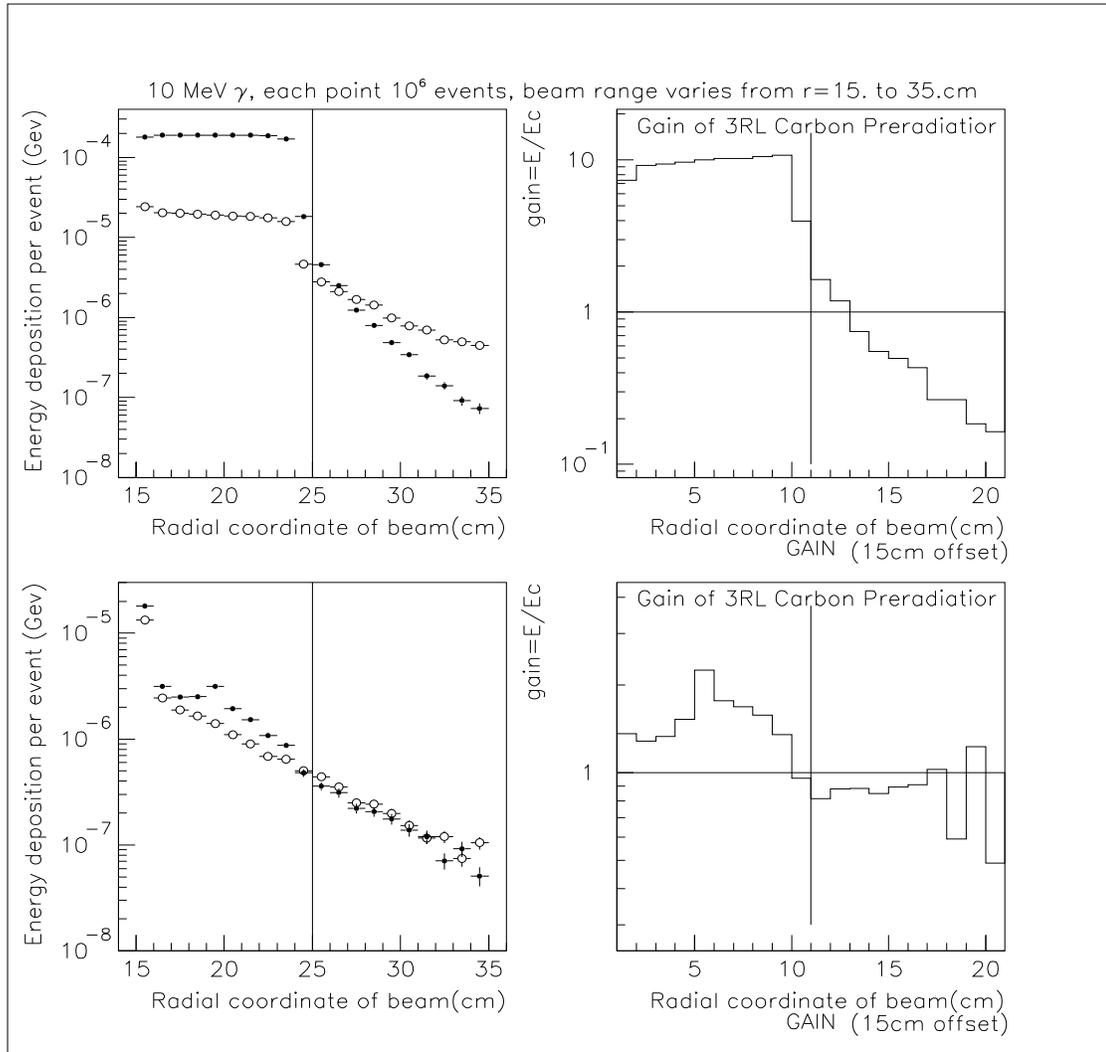


Figure 2.27: The total energy deposited by 10 MeV photons in the Møller detector (top left) and in the quartz layers behind the Møller detector (bottom left) as a function of the initial beam locations. Empty circles (full circles) represent the data taken from the geometry where there is (no) 3 radiation length of carbon radiator at the front. Top right (bottom right) graph shows the improvement factor due to C preradiator throughout the detector surfaces when Møller detector (the quartz layers) is (are) considered.

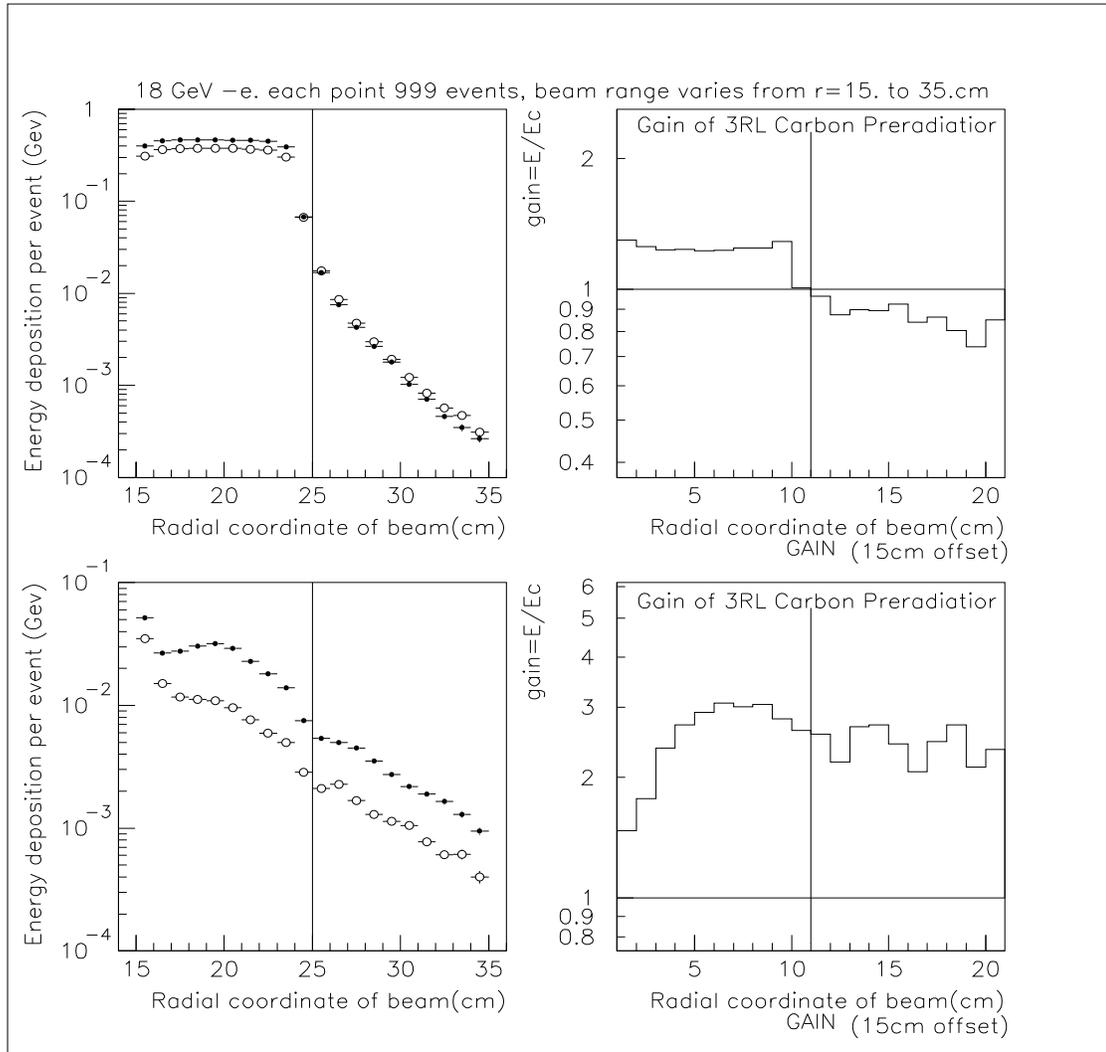


Figure 2.28: The total energy deposited by 18 GeV electrons in the Møller detector (top left) and in the quartz layers behind the Møller detector (bottom left) as a function of the initial beam locations. Empty circles (full circles) represent the data taken from the geometry where there is (is no) 3 radiation length of carbon radiator at the front. Top right (bottom right) graph shows the improvement factor due to C preradiator throughout the detector surfaces when Møller detector (the quartz layers) is (are) considered.

from the outside. The ten Cu rings are the diagnostic rings placed uniformly right in front of the back shielding. Even though, they have same thicknesses which are 3 cm in radial and 1 cm in z direction, their inner and outer radii are different from one another. In the simulation, 18 GeV electrons are sent to the Møller detector in the radial range of 21 cm to 24 cm and the corresponding energy deposited in the rings is recorded separately to see how the magnitude of the radiation vary with the rings, or with the radius indirectly. As an output, Fig. 2.30 shows energy deposition per event as a percentage of the incident beam energy in the rings such that ring number one corresponds the smallest ring in terms of the radius and so on. The vertical axis is in logarithmic scale in the graph. There is an exponential dependence between the energy deposition and the radial position of the rings. We see the maximum energy deposition at the second ring because it corresponds to the radial range where the beam is sent. According to data, $(0.16 \pm 0.003)\%$ of the incident energy is accumulated at the second ring. At the 10th ring this goes down to $(0.4 \pm 0.04) \cdot 10^{-3}\%$. Between the two rings there is a 44 cm distance in radial direction that yields a suppression of a factor of 400. In addition, Fig. 2.31 shows the energy deposition per event to the rings in the unit of *rad*, which is used to measure the radiation dosage in a medium. The conversion is done by using

$$\text{absorbed dose (rad)} = \frac{\text{absorbed energy (MeV)}}{6.24 \times 10^{10} (\text{MeV/kg})} \times \frac{1}{\text{density (kg/cm}^3\text{)}} \times \frac{1}{\text{volume (cm}^3\text{)}} \quad (2.5.2)$$

Since the diagnostic rings are made of Cu, here we use the density of copper 8.96 g/cm³ as the density. According to the graph at Fig. 2.31, the gain in terms of the radiation suppression between second and tenth rings is 1150. The discrepancy in terms of the suppression between two graphs comes from the inequality of the volumes of the two rings since the absorbed dosage is inversely proportional to the

volume of the material as shown in Eq. 2.5.2.

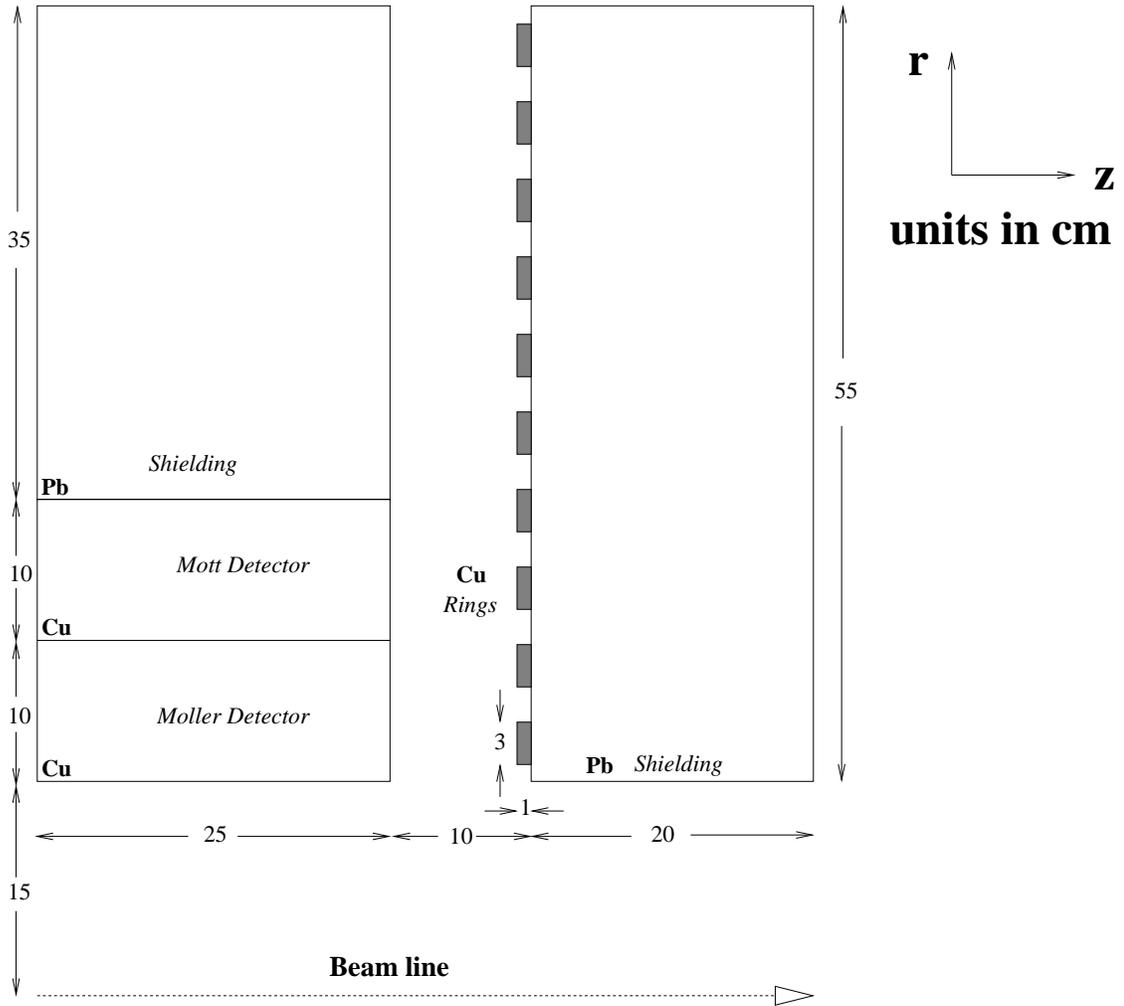


Figure 2.29: The cross section of cylindrical geometry above the beam line.

If we calculated the total dosage absorbed in the rings throughout the experiment based on findings above, we would know the total number of electrons coming to the detector. According to the proposal of the experiment [32] $2-4 \times 10^7$ electrons are expected to be hitting the detector per pulse. The repetition rate of the pulses is 120 Hz and the acquired time for the experiment is 20 weeks with the

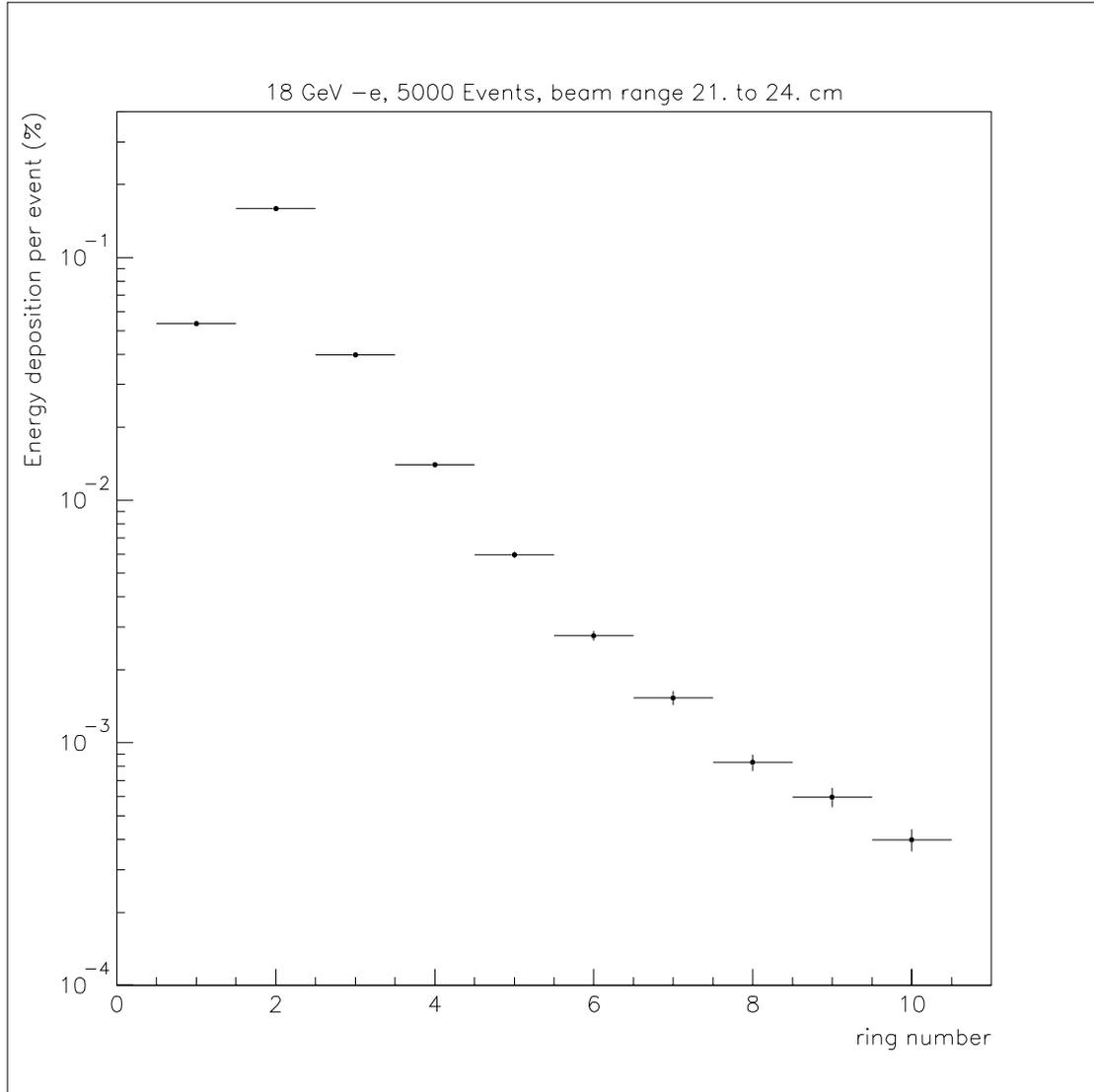


Figure 2.30: The energy deposited in the diagnostic rings per event as a percentage of the initial energy of the beam.

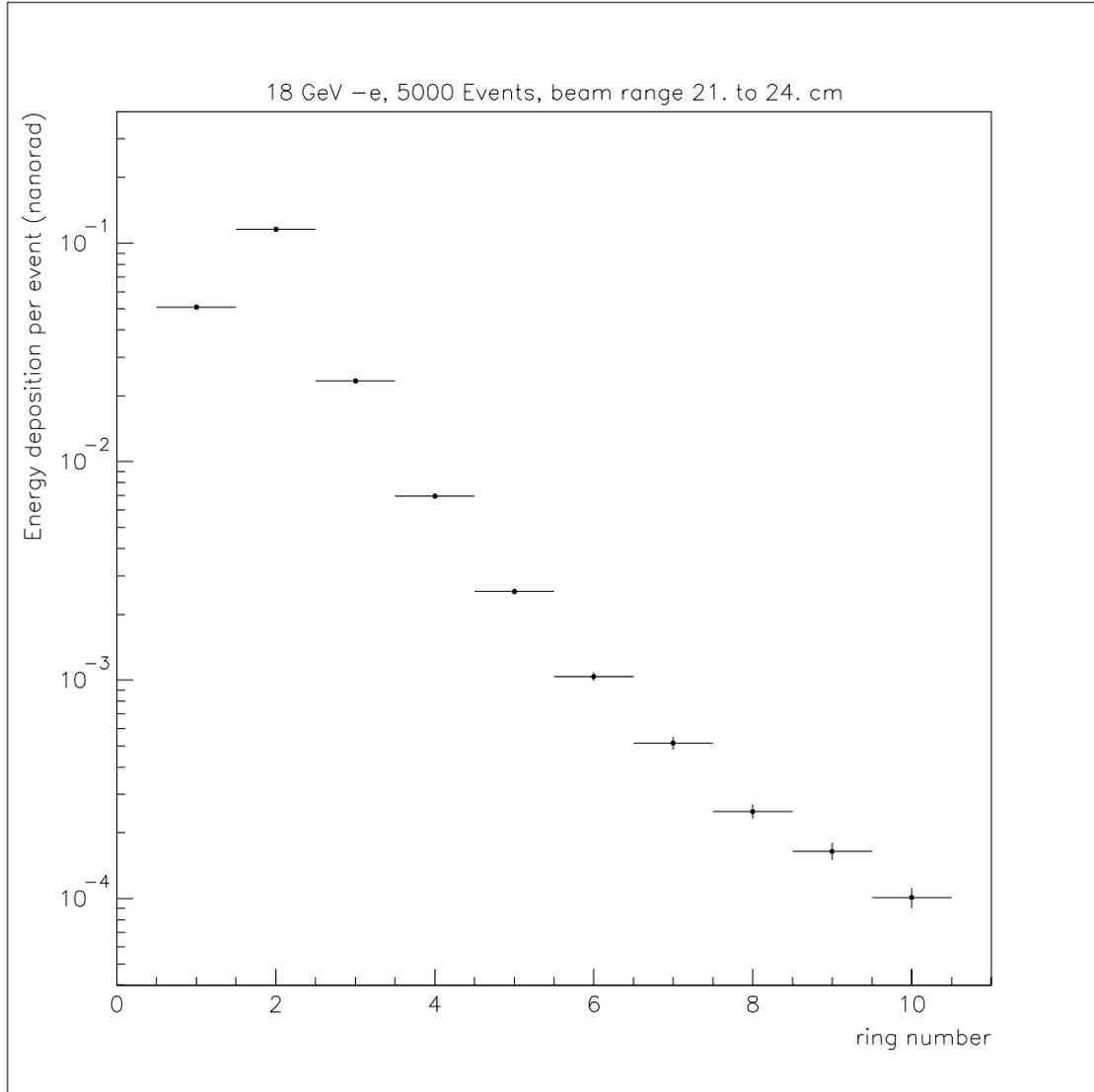


Figure 2.31: The energy deposited in the diagnostic rings per event in the absorbed dosage unit of $rad \times 10^{-9}$.

efficiency of 43%. Therefore

$$\begin{aligned} \text{total \# of -e} &= 3 \times 10^7 \left(\frac{-e}{pulse} \right) \times 120 \left(\frac{pulse}{sec} \right) \\ &\times 5.2 \times 10^6 (sec) = 1.87 \times 10^{16} \end{aligned} \quad (2.5.3)$$

By using the absorbed dose per event and the total number of electrons, the total absorbed dose is found to be about 1.89 ± 0.2 Krad in the ring 10 while this value is 2.2 ± 0.04 Mrad in the ring 2. Since the total radiation length of the designed Møller detector is about 2 radiation length less than that of the Møller detector in the simulation, this causes more energy deposition in the rings in reality than in the simulation. If we take this into account the realistic numbers are about twice the results of the simulation. Under these circumstances, the value calculated for the ring 10 is 1.89 Krad, less by a factor of 25 than the total absorbed dose limit for the PMTs mentioned earlier.

Even though the level of suppression achieved above is encouraging, we should increase it as much as possible because we may have been missing rare events of highly energetic particles that may cause PMTs to reach the exposure limit during the experiment. These kinds of events may have been slipping from the simulations since the number of events are very small as compared to that of the experiment. Therefore, a proper shielding should be adopted so that the PMTs will be prepared to such occurrences and more. At the same time, PMTs will be in a less noisier environment in terms of the radiation relative to the unshielded case.

Three different shielding studies were done. Since the second and the third are related to each other to a certain extent, both of them are worth of mentioning here rather than the one picked in the design.

The first shielding design is as follows: a Pb ring with dimensions of $r_{min}=36$, $r_{max}=45$; $z_{min}=25$ and $z_{max}=31$ cm is placed to the current geometry (Fig. 2.29)

assuming the beginning of the beam line being the origin (Fig. 2.32). Its purpose is to absorb any radiation coming from the Møller detector to the diagnostic ring 10 where the PMTs will be replaced. As a result, the absorbed dose is found to be $(2.61 \pm 0.89) \times 10^{-6}$ nanorad per event at ring 10 (Fig. 2.33). This means that the suppression on ring 10 due to the added shielding is about 30. If we calculate total absorbed radiation throughout the experiment at ring 10, it will be 63 rad ($= 1.89 \times 10^3/30$).

The second shielding simulation is aimed to achieve the same or less radiation for the PMTs without the extra piece of Pb shielding used in the previous case. Alternatively, the Pb tube behind the detectors is utilized for the shielding. Meanwhile, its r_{max} is shortened from 70 cm to 60.5 cm which is r_{min} of ring 9. The related cross-sectional geometry is given in Fig. 2.34. It is apparent that considering ring 9 rather than ring 10 will not make the situation any better unless it is pushed in the z direction so that it will be shielded by the Pb tube in the back. Fig. 2.35 shows the energy depositions in the rings with the current geometry. Data marked by circle, square and triangle represents the cases where the displacements of ring 9 are 0 cm, 3 cm and 6 cm in z direction respectively. The relative suppression is about 20 and 150 if the ring 9 is moved 3 cm and 6 cm from the initial position in z direction respectively. In addition, the suppression relative to the previous shielding (Fig. 2.32) is about 2.5 which means that the total radiation absorbed throughout the experiment has been reduced to as low as 25 rad. So, the current method of shielding reduced the suppression slightly better than the previous one without adding the extra Pb shielding.

The third simulation is carried out to see any use of adding the extra Pb tube, used for the first simulation, into the current geometry (Fig 2.34). Fig. 2.36 shows the energy depositions in the rings with the geometry. Again, data marked by

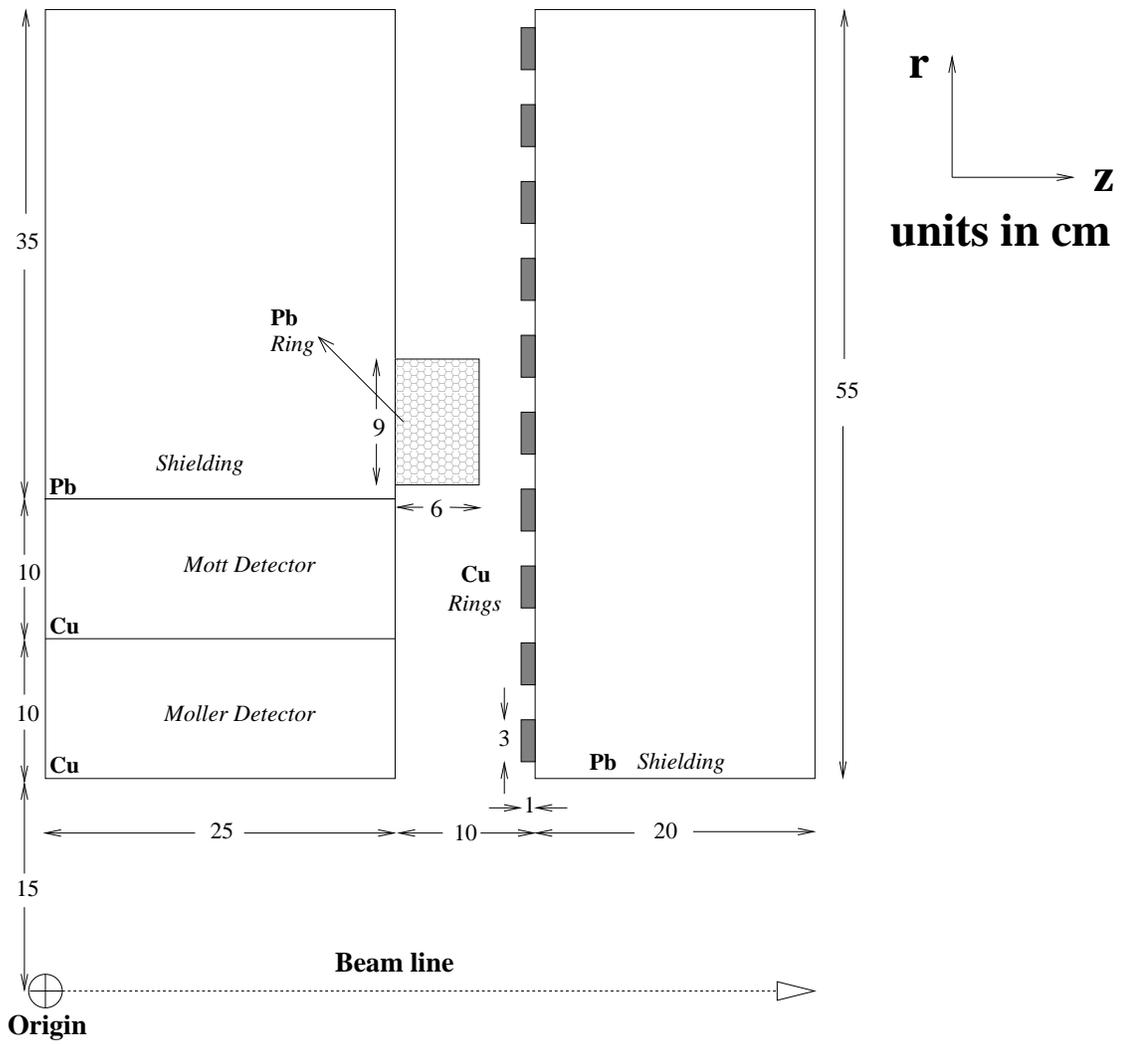


Figure 2.32: The cross section of cylindrical geometry above the beam line. In this case a new Pb shielding is added to the geometry.

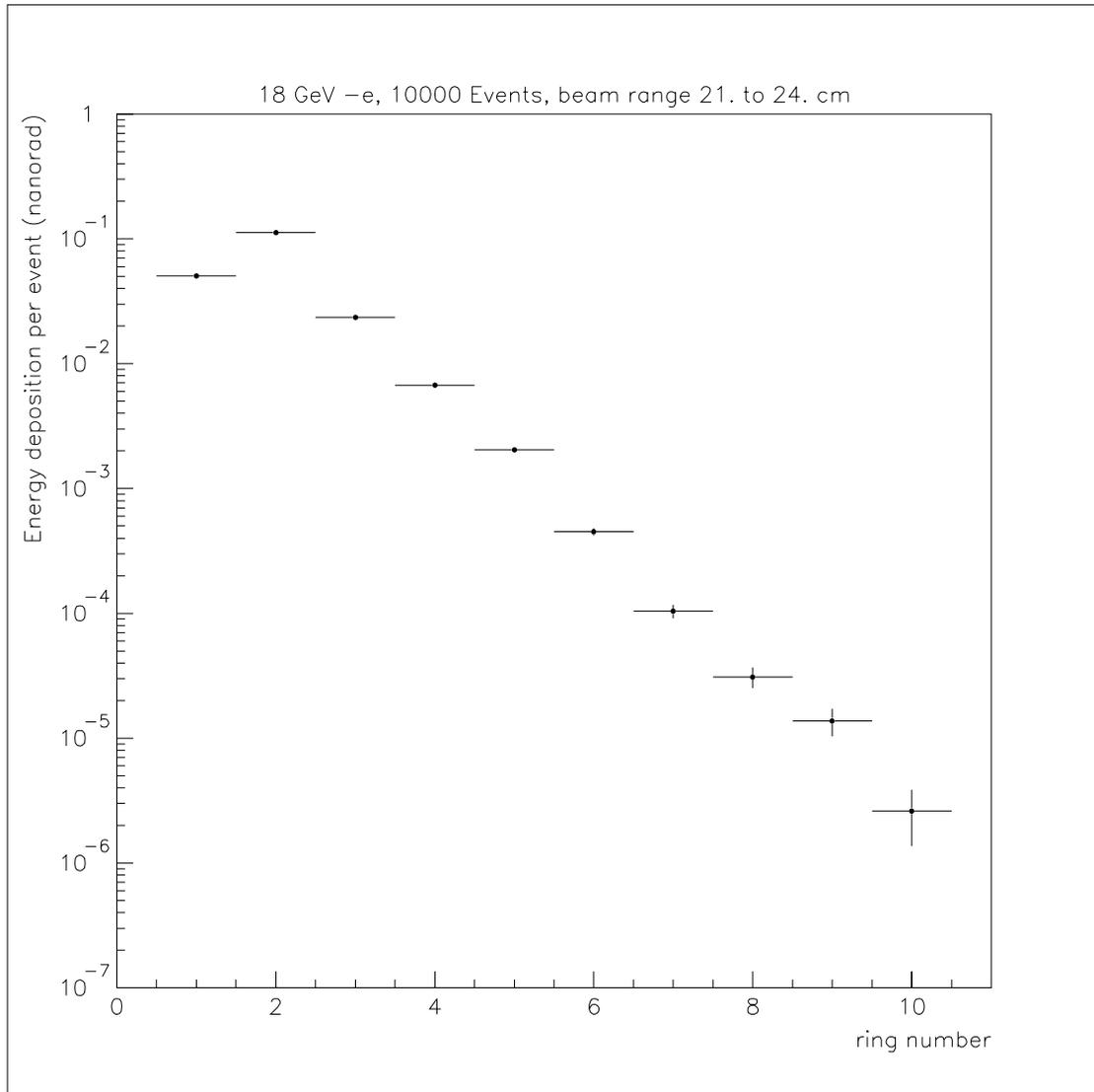


Figure 2.33: The energy deposited in the diagnostic rings per event in the absorbed dosage unit of $rad \times 10^{-9}$ in the case where a new Pb shielding is added (Fig. 2.32).

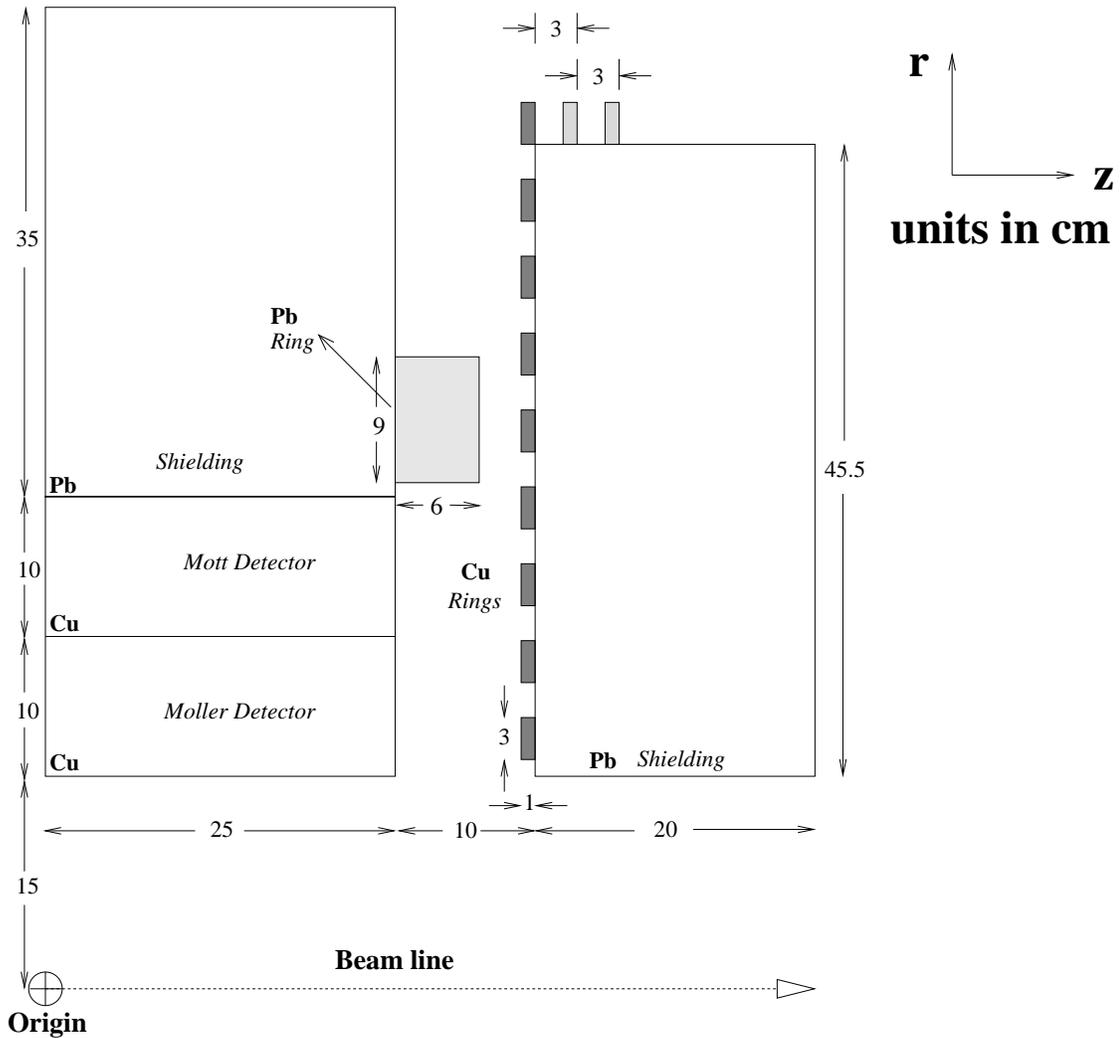


Figure 2.34: The cross section of cylindrical geometry above the beam line. In one case, the extra Pb shielding is kept and in the other case it is removed. Also, Pb shielding in the back is trimmed up to the r_{min} of ring 9. Also sub-configurations are shown in which the ring 9 inserted into the latter shielding by 3 cm and by 6 cm in the z, or beam line axis direction.

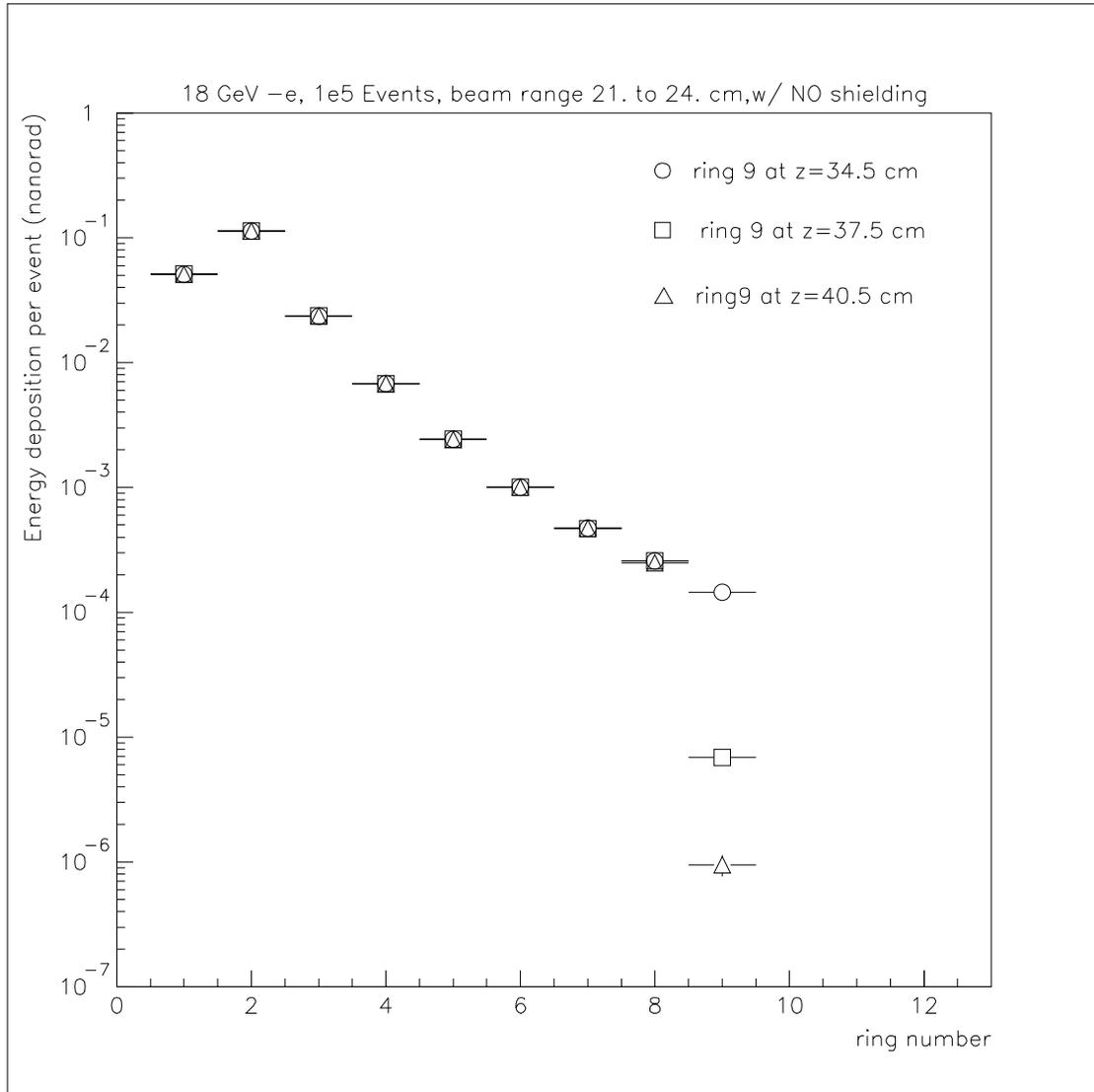


Figure 2.35: Energy depositions in the rings for three configurations. Data marked by circle, square and triangle represents the cases where the displacements of ring 9 are 0 cm, 3 cm and 6 cm in z direction respectively.

circle, square and triangle represents the cases where the displacements of ring 9 are 0 cm, 3 cm and 6 cm in z direction respectively. The extra piece of Pb shielding increased the relative suppression for the first two situations by almost a factor of 10 but for the third situation about a factor of 5. This indicates that if the ring 9 is moved to the z direction deeper and deeper the data from the two geometry converge, in turn, they may even merge at some point where getting rid of the extra shielding won't make difference in terms of energy depositions in ring 9. In order to check if such intersection occurs, data from ring 9 as a function of the displacement in z is fitted for the two geometry separately (Fig. 2.37). The function used for the fits is

$$f(z) = p_1(1 + p_2 * e^{-z}) \quad (2.5.4)$$

where p_1 and p_2 are the fit parameters. If the functions of the fits merge at some point in z then that point must satisfy both of them at the same time which means that we can find that point by solving the equation that is created by equating them. Although two functions converge in z direction, they don't intersect. In summary, even though the suppression is 5 times better with the extra Pb shielding at $\Delta z_{ring9}=6$ cm, it has been chosen not to include it in the geometry since this level of suppression is already 10^3 lower than the exposure limit of a PMT.

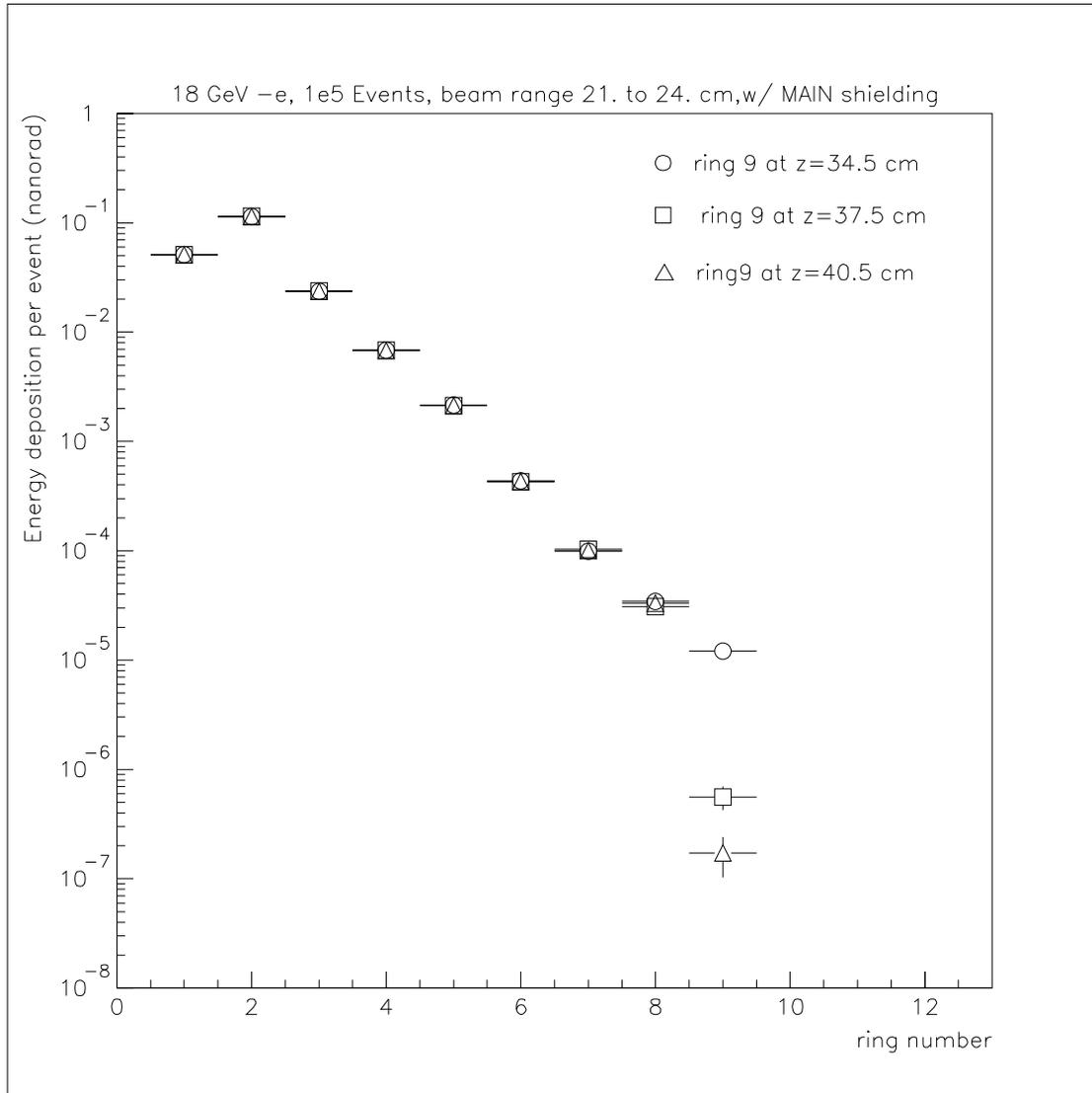


Figure 2.36: Energy depositions in the rings for three configurations obtained while the extra Pb shielding is placed to the geometry (see Fig. 2.34). Data marked by circle, square and triangle represents the cases where the displacements of ring 9 are 0 cm, 3 cm and 6 cm in z direction respectively.

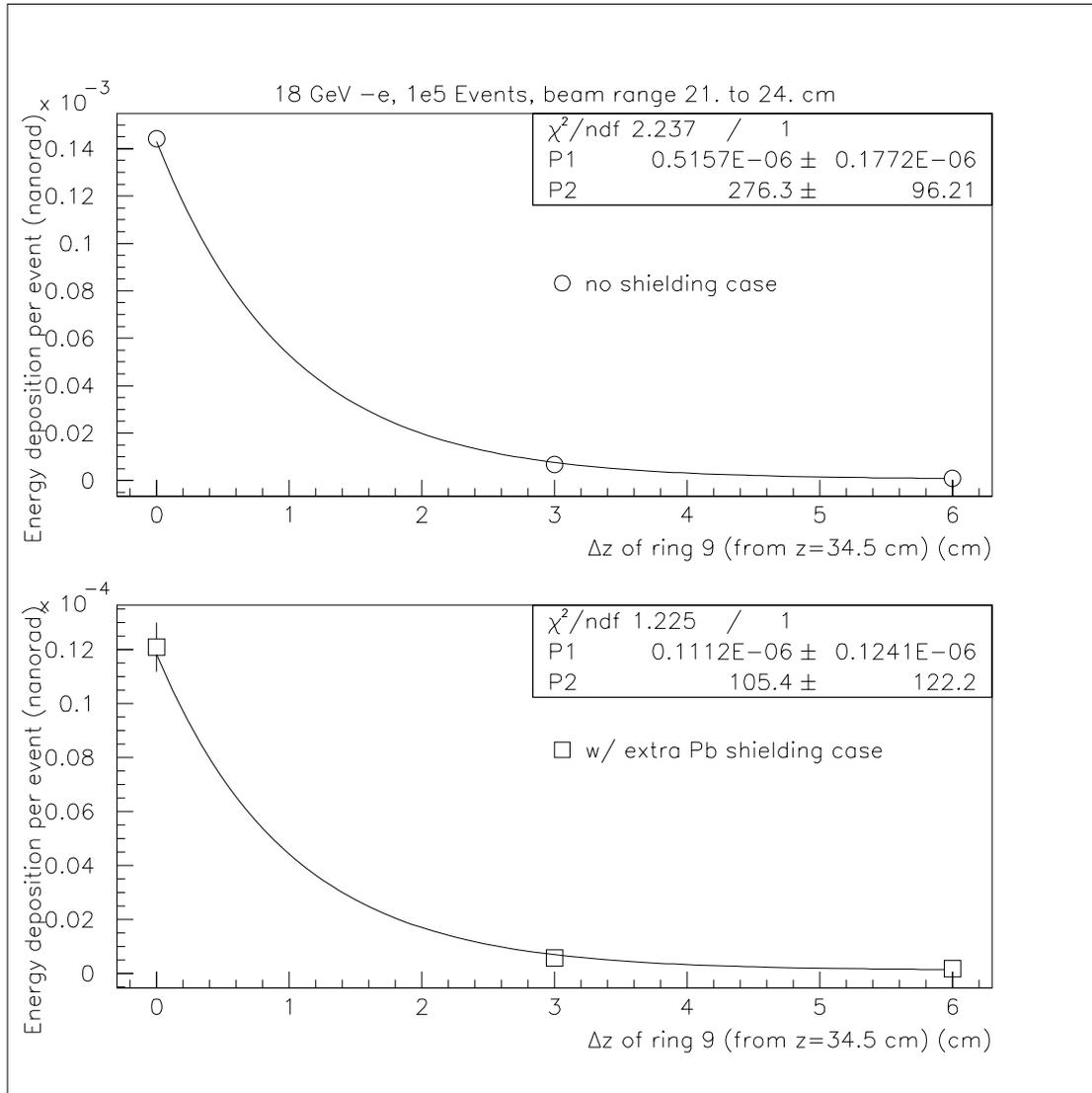


Figure 2.37: Energy depositions from ring 9 vs Δz or the displacement relative to $z=34.5$ cm, the initial ring position. The fitted data marked with circle in the upper and square in the lower plot correspond the simulations when there is no extra shielding and when there is an extra shielding respectively.

Chapter 3

Synchrotron Radiation Analysis

3.1 Introduction

This chapter is devoted to work related to the E158 experiment. Specifically, it covers the description of the synchrotron light monitor(SLM) apparatus setup as well as summarizes the progress in the analysis of its data.

Synchrotron light is monitored in A-line where the polarized electrons get bent towards the liquid H₂ target (Fig. 2.1 [33], Fig. 3.1 [16]). Our main source of the synchrotron radiation (SR) is created by B15 bending magnet at the upstream end of the A-line. There are two different systems looking at the synchrotron radiation at the same location. One is for the visible SR part (low energy spectrum) and the other is for high energy part of the spectrum, which is typically in the order of MeV energy scale. Throughout this chapter, our main focus will be on the high energy part of the SR. The schematic diagram of the high energy SLM detector is given in Fig. 3.3.

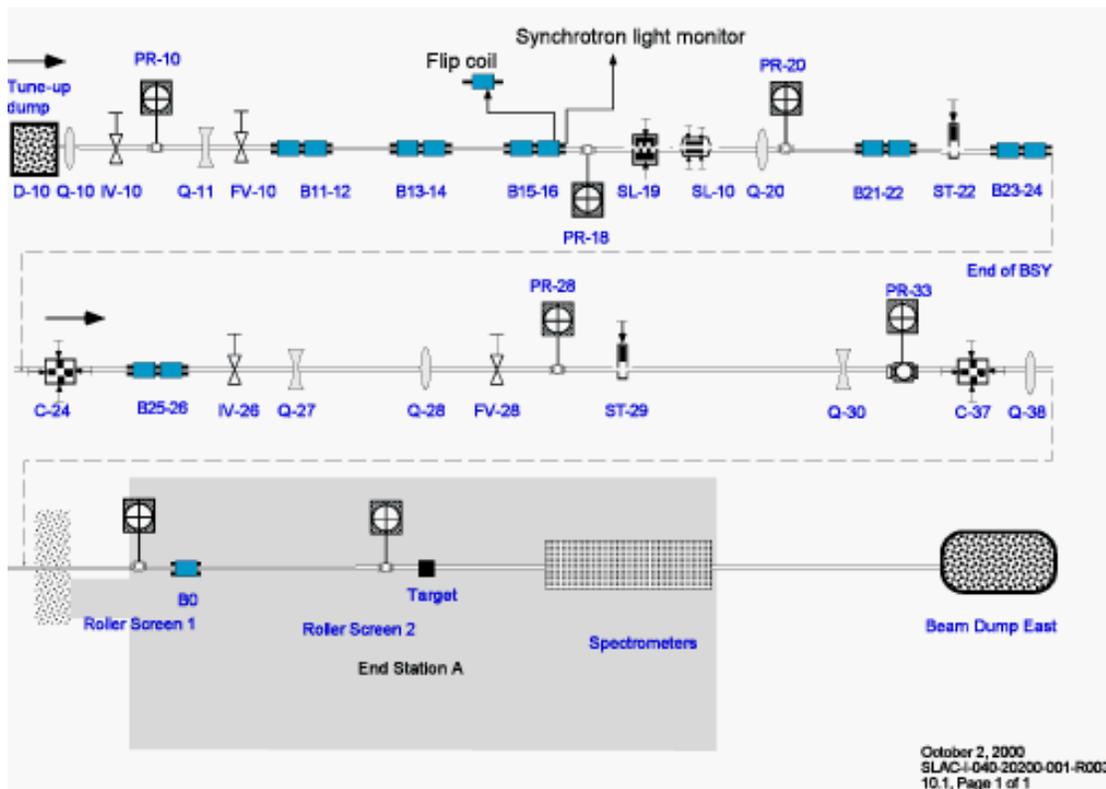


Figure 3.1: Overview of A-line.

3.2 Motivation

There are two important reasons which appealed us to work on the subject. By using the SR data, it is possible to determine if vertical polarization (P_σ) [18], [19] of the beam is helicity dependent or not, and also to cross-check energy measurements with beam position monitors (BPMs).

As the name implies, P_σ is the vertical component of polarization which is induced by the magnets of the A-line. It is the component that can cause an energy and SR background asymmetry. The measured asymmetry (A_{meas}) by the experiment is the sum of the physics asymmetry (A_{phy}) and the asymmetries due to beam properties (A_{beam}).

$$A_{meas} = A_{phy} + A_{beam} \quad (3.2.1)$$

In order to extract A_{phy} , A_{beam} must be measured precisely. A_{beam} may arise from asymmetries in the beam position, angle, energy or intensity.

If the P_σ is different for the two helicities, then this will cause an asymmetry which is given by

$$A_{P_\sigma} = \frac{P_\sigma(\eta = +1) - P_\sigma(\eta = -1)}{P_\sigma(\eta = +1) + P_\sigma(\eta = -1)} \quad (3.2.2)$$

where $\eta = +1(-1)$ for the right-handed(left-handed) electrons. Since different polarizations emit different amounts of SR, A_{P_σ} can be detected by the SLM detector. Due to the nature of A-line, the SLM data has a strong energy dependence which allows us to cross-check energy measurements with BPMs.

3.3 The Description of High Energy Synchrotron Light Monitor (SLM)

As shown in Figure 3.2, the two SR systems are beside the beam pipe as we are looking towards the upstream part of the beam line. The setup is partially shielded under the lead. A sketch of the high energy SLM will provide more details of its elements (Fig. 3.3). High energy synchrotron radiation, after splitting from the electron beam, goes into the block next to the beam pipe and passes through an aluminum flange, a lead filter/radiator, and a quartz Cherenkov radiator (Fig. 3.4) in order to produce visible light for the photodiodes (Fig. 3.5). By using a combination of reflectors and a mirror, the visible light is then guided to the lead housing to be detected by the photodiodes (Fig. 3.5). Presently, model UDT PIN 10D photodiodes from United Detector Technology are used in the setup. They are operated in photoconductive mode, cabled to a unity gain bias module which drives a 50Ω load (Fig. 3.6). In addition, the output goes over a long RG58 cable (approximately 800ft. long) to a Camac 2249W 11-bit ADC which is a charge sensitive at 0.25 pC/count. We run with a 500 nano sec. gate width. Four photodiodes are currently fed into the data acquisition system. Three of them are mounted on the backplate of the box. The fourth one is situated under the block, and faces to the beam pipe, and provides on the information outside of the setup.

3.4 Pedestal Noise

Pedestal noise is the intrinsic noise of the SLM detector. Figure 3.7 shows the related pedestal and raw signal of synchrotron light monitor I (SLM1) for the run



Figure 3.2: A digital image of both low and high energy SR detectors beside the beam pipe

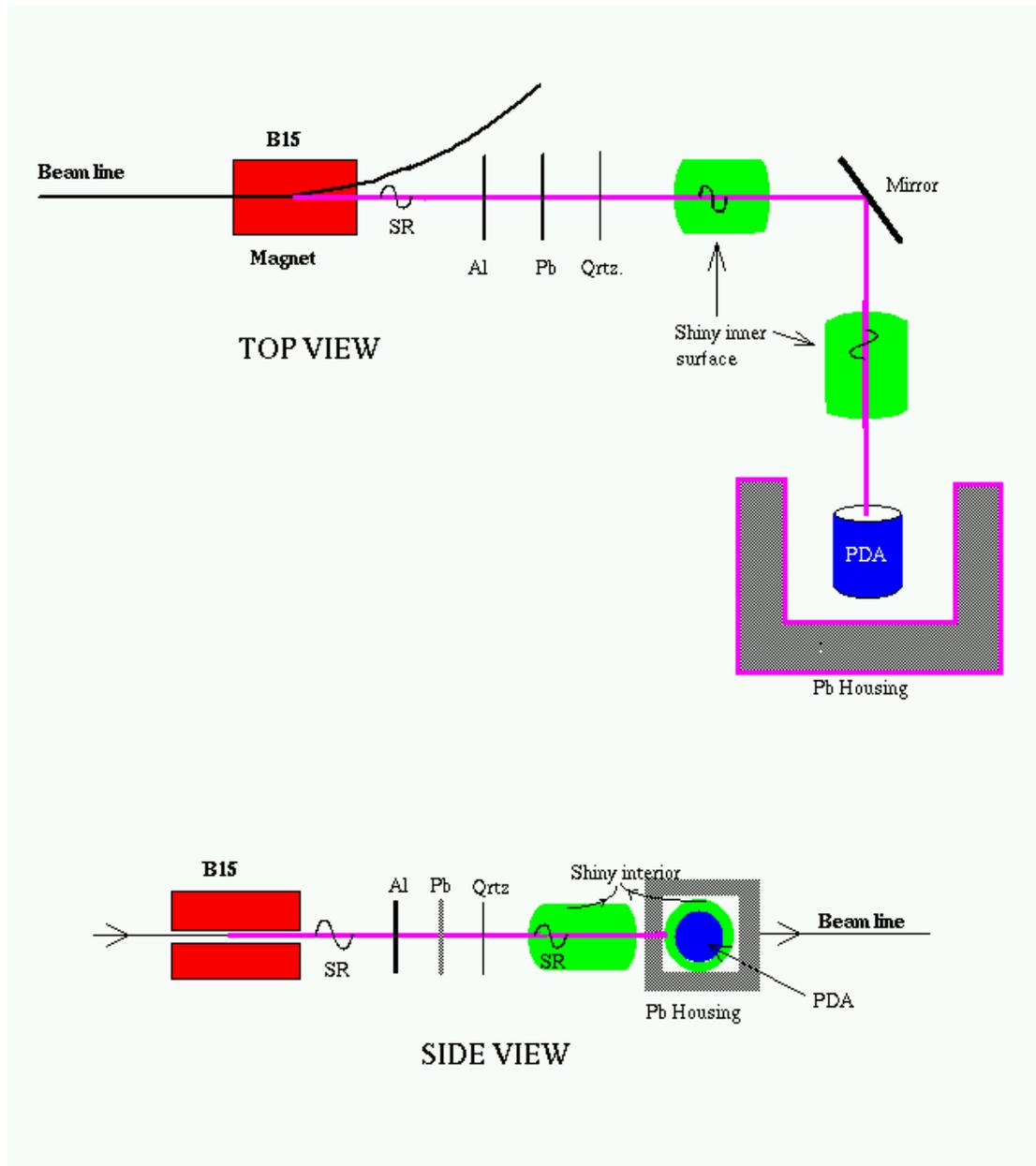


Figure 3.3: Detector system for MeV SR photons

1799. Accordingly, for a 1267 ADC channel signal in a synchrotron light monitor we get ~ 2 ADC channel width on the pedestal signal which in turn gives the pedestal noise width, $\sigma_{pedestal}(= \delta_{pedestal}/\text{Signal size}) \cong 1.58 \times 10^{-3}/\text{gate}$. Here, a gate is 100-350 nanoseconds time window and carries $(3.5 - 6) \times 10^{11}$ electrons.

In order to check if we are dominated by the pedestal noise or not, the width of other contributions σ_{other} is calculated explicitly via the width of an SLM asymmetry σ_{Asym} that utilizes gate pairs. In the calculation, the value for σ_{Asym} was quoted from Fig. 3.11. As a result, we found σ_{other} as 3.12×10^{-3} which is bigger than pedestal noise width.

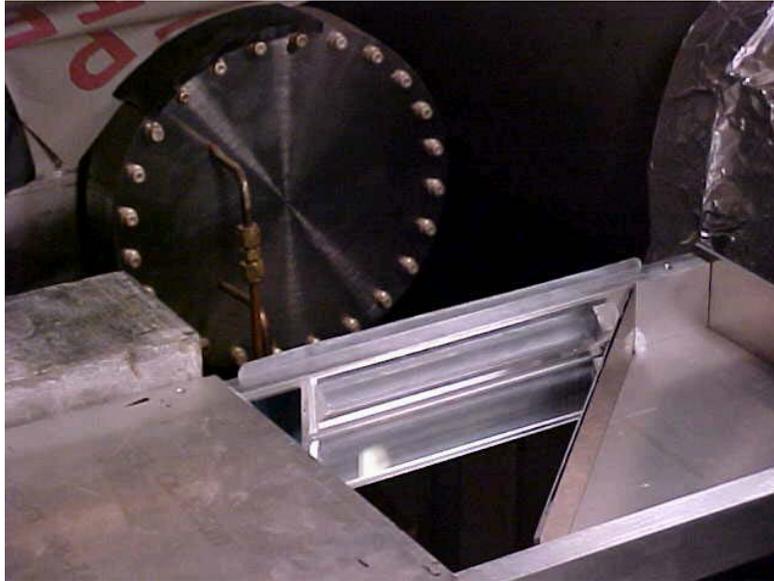


Figure 3.4: Showing the Cherenkov radiator, 45° tilted mirror and interior of the box.

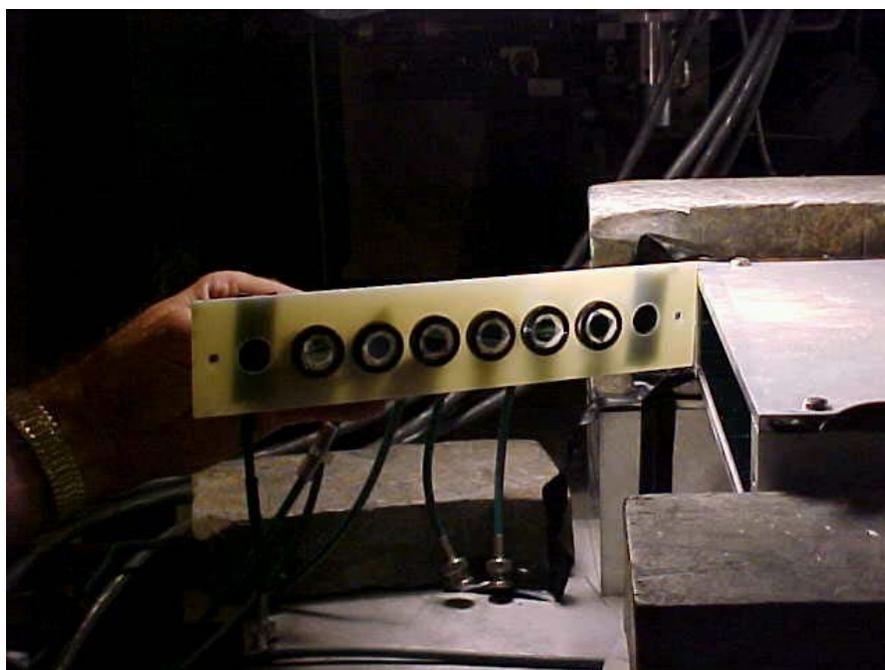


Figure 3.5: Showing photodiode array mounted to the backplate of the high energy SR detector box.

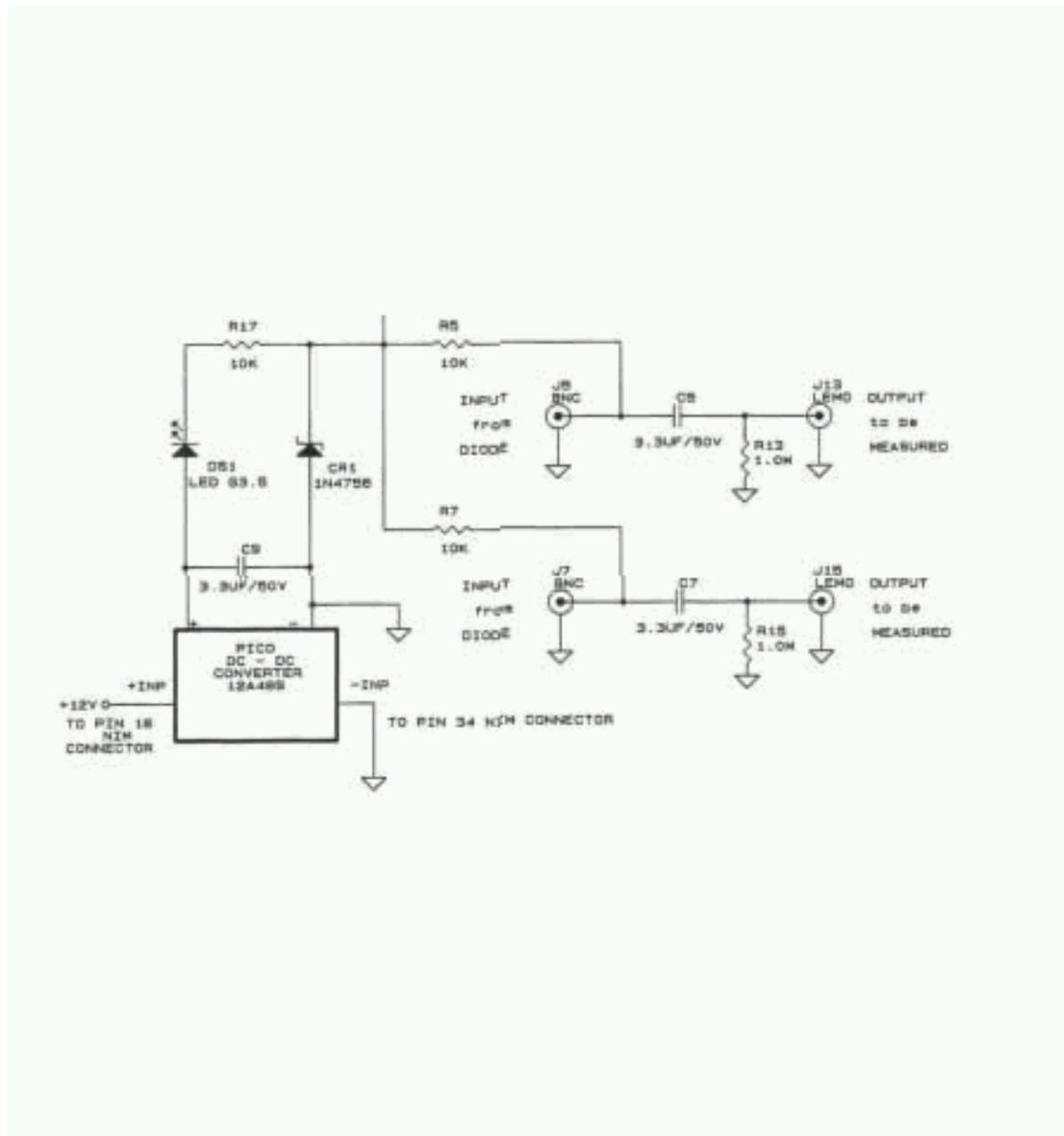


Figure 3.6: Circuit design of the photodiodes, showing two channels out of four.

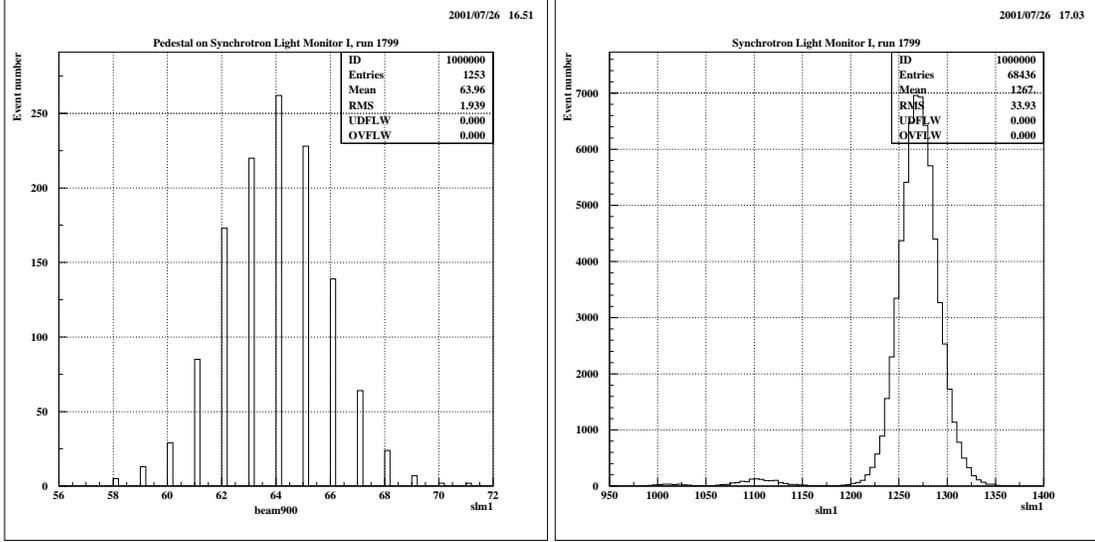


Figure 3.7: The pedestal and the raw signal of synchrotron light monitor 1 in the unit of the ADC counts

$$\sigma_{Asym}^2 = \frac{\sigma_{gate}^2}{2} \Rightarrow \sigma_{gate} \cong \underline{3.5 \times 10^{-3}/gate}, \quad (3.4.1)$$

$$\text{where } \sigma_{Asym} = 2.5 \times 10^{-3}/gate \text{ pair} \quad (3.4.2)$$

$$\sigma_{gate}^2 = \sigma_{pedestal}^2 + \sigma_{other}^2 \Rightarrow \quad (3.4.3)$$

$$\sigma_{other} \cong \boxed{3.12 \times 10^{-3} /gate} \quad (3.4.4)$$

3.5 Linearity Studies

We have compared the asymmetry (A_{slm1}) measured by the SLM1 with the asymmetry (A_{toroid}) measured by one beam current monitor (BCM) as shown in Fig. 3.8. The slope of the graph is close to 1 which means that the SLM asymmetry is

quite linear to the BCM asymmetry. In addition, we also checked the linearity of *normalized*¹ SLM asymmetry versus the energy resolution, i.e. $\Delta E/E$. The slopes are more or less -2 in Fig. 3.9 for both energy BPMs, indicating an approximate E^{-2} dependence, which is what was expected in the presence of a constant magnetic field vertical to the beam path. I should mention the fact that we are not measuring energy resolution directly, but we utilize a BPM situated on the arc of the beam line where the dispersion in position is quite sensitive to the beam energy. The formula(3.5.1) has been used for the conversion [21];

$$\frac{\Delta E}{E} = \frac{\left(\frac{X_L}{I_L}\right)^{bpm} - \left(\frac{X_R}{I_R}\right)^{bpm}}{500mm} \quad (3.5.1)$$

where *bpm* is the label that tells which BPM is used. We are interested in x position because it is the relevant one as far as the energy dispersion is concerned. We have two energy BPMs, namely bpm12 and bpm24. If we use the sum of both energy BPMs rather than one energy BPM, we ought to see an inversely proportional dependence to E , which is observed in Fig. 3.10.

3.6 The limit exerted on the Vertical Polarization by Synchrotron Radiation

Using the bending angle (Θ_{bend}) data (see Tab. 3.1) read from SCP (SLAC Control Program) we can put a limit on the vertical polarization (P_σ). Accordingly, the total bending angle due to the magnets² is found to be $98\mu\text{rad}$. Since P_σ in terms

¹Means every left or right helicity item(X_L or X_R) in the asymmetry is divided by the left or right helicity current(I_L or I_R) respectively.

²Bending due to quad magnets and at Linac are not included in this calculation

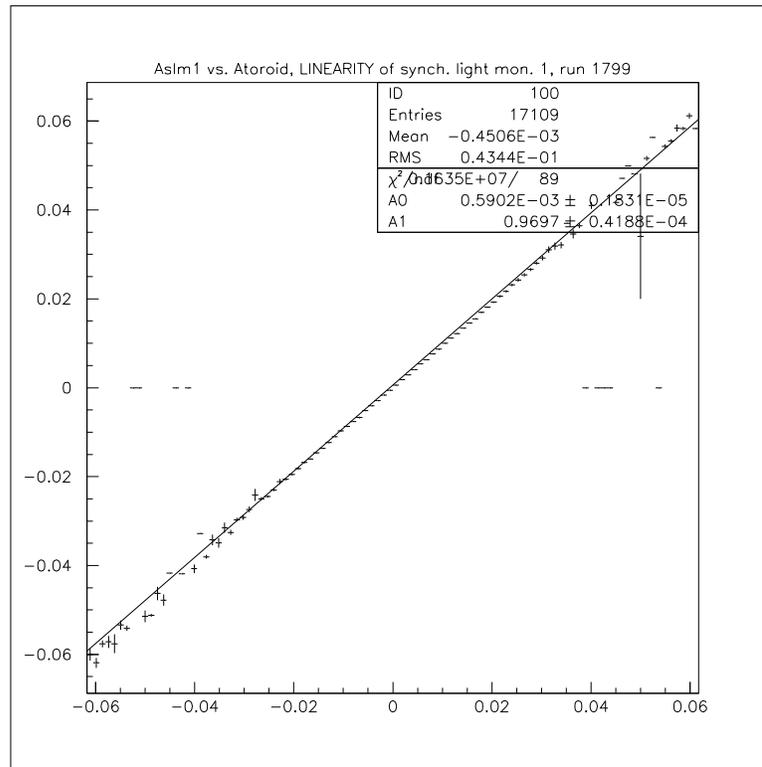


Figure 3.8: Synchrotron light monitor 1 (SLM 1) asymmetry vs. toroid asymmetry for run 1799.

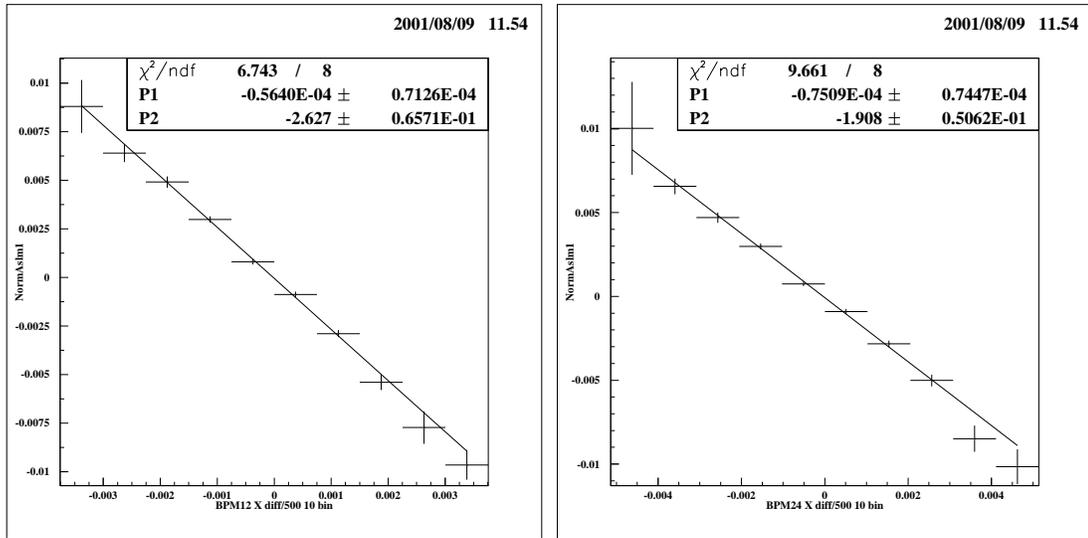


Figure 3.9: Normalized SLM 1 Asymmetry vs. Energy bpm resolution ($\Delta E/E$) taken from beam position monitor 12 and 24 in the horizontal direction for the run 1470, P2 is the slope of the fit.

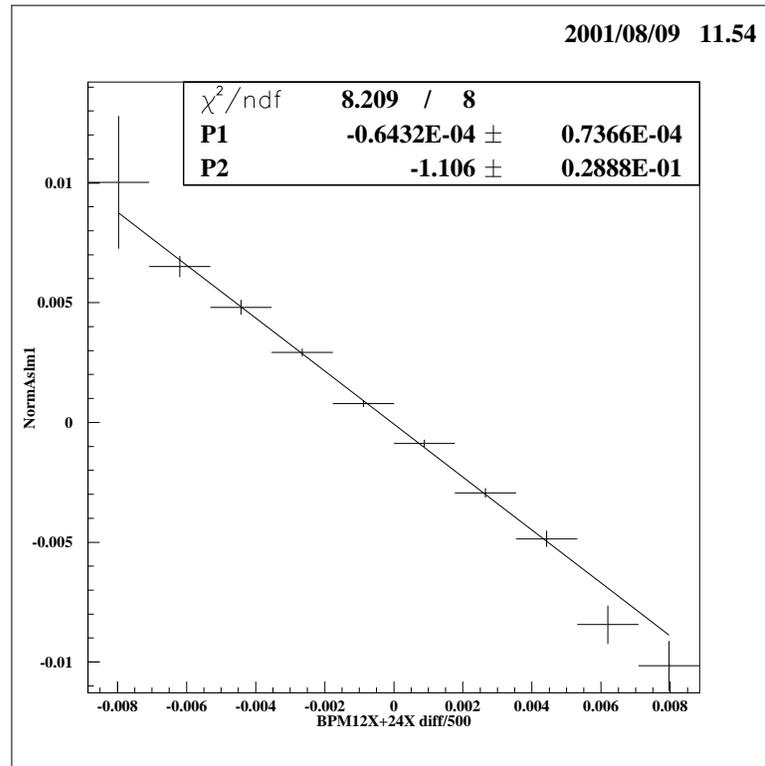


Figure 3.10: Normalized SLM 1 Asymmetry vs. Sum of two energy bpm resolution, $[(\Delta E_{bpm12} + \Delta E_{bpm24})/E]$, P2 is the slope of the fit.

of Θ_{bend} and the polarization of the beam in the beam direction P_z is given by

$$P_\sigma \approx 100 \times \Theta_{bend} \times P_z \quad (3.6.1)$$

we expect P_σ to be about 1% of P_z where P_z is $\sim 75\%$

Corrector Magnets	$\theta(\mu\text{rad})$
A1V	18
A4V	60
A10	02
A18	-42
A29	36
A33	24
TOTAL	98

Table 3.1: Bending angles a) top table; due to magnets at upstream of SLM, b) bottom table; due to the magnets after the momentum slits.

3.7 SLM Asymmetry Width and Regression Analysis

In this section the asymmetry measured by the SLM (A_{slm}) will be studied in detail. A regression technique will be used to eliminate asymmetries in the energy, position and angle of the beam.

Fig. 3.11 shows A_{slm} using data of SLM1 for a run. The upper plot in the figure gives the width of the distribution (σ_{Asym}) as 2.5×10^{-3} /gate pair. This number has already been quoted in the pedestal section. The graph also shows

that one outlier event can weigh on the width pretty much and may affect at a noticeable level (here 20% change). Assuming that the number of total gates is 10^8 for the whole experiment, the error in the SLM asymmetry should go down to $\approx 4. \times 10^{-7}$ or .4 ppm ($\cong 2.5 \times 10^{-3} / \sqrt{10^8/2}$).

Since the measured asymmetry at hand carries all helicity correlated effects such as energy, positions and angles in both x and y directions we need to take out those effects to get close to the vertical polarization asymmetry which the SLM sees by implementing a regression technique in the analysis. The regression procedure here is first order, and is straightforward once all the data is available; even though we don't have direct means of measuring energy and angle, we use a common technique which is to utilize beam position monitors by placing them in a smart way on the beam line. The way to measure energy is mentioned in previous section. As for the angle measurement, we utilize two BPMs this time. If we are to find angle on x axis (θ_x) we just need to differentiate one bpm³ from the other in the x direction. Even though what we find is in the units of length, we know the distance between two BPMs (call it d) and can convert it into angle by;

$$\tan \theta_x = \frac{\Delta x_{bpm}}{d} \Rightarrow \theta_x = \tan^{-1} \left(\frac{\Delta x_{bpm}}{d} \right) \quad (3.7.1)$$

The contribution due to a beam parameter on the asymmetry distribution depends on the degree of its correlation. If the scatter plot of the asymmetry against the parameter is fitted to a first order polynomial function ($f(x) = ax + b$), one of the two parameters gives the slope which quantifies the amount of the correlation. It is also called *correlation coefficient*. For example, if we regress

³Each bpm measures positions of the beam in two dimensions

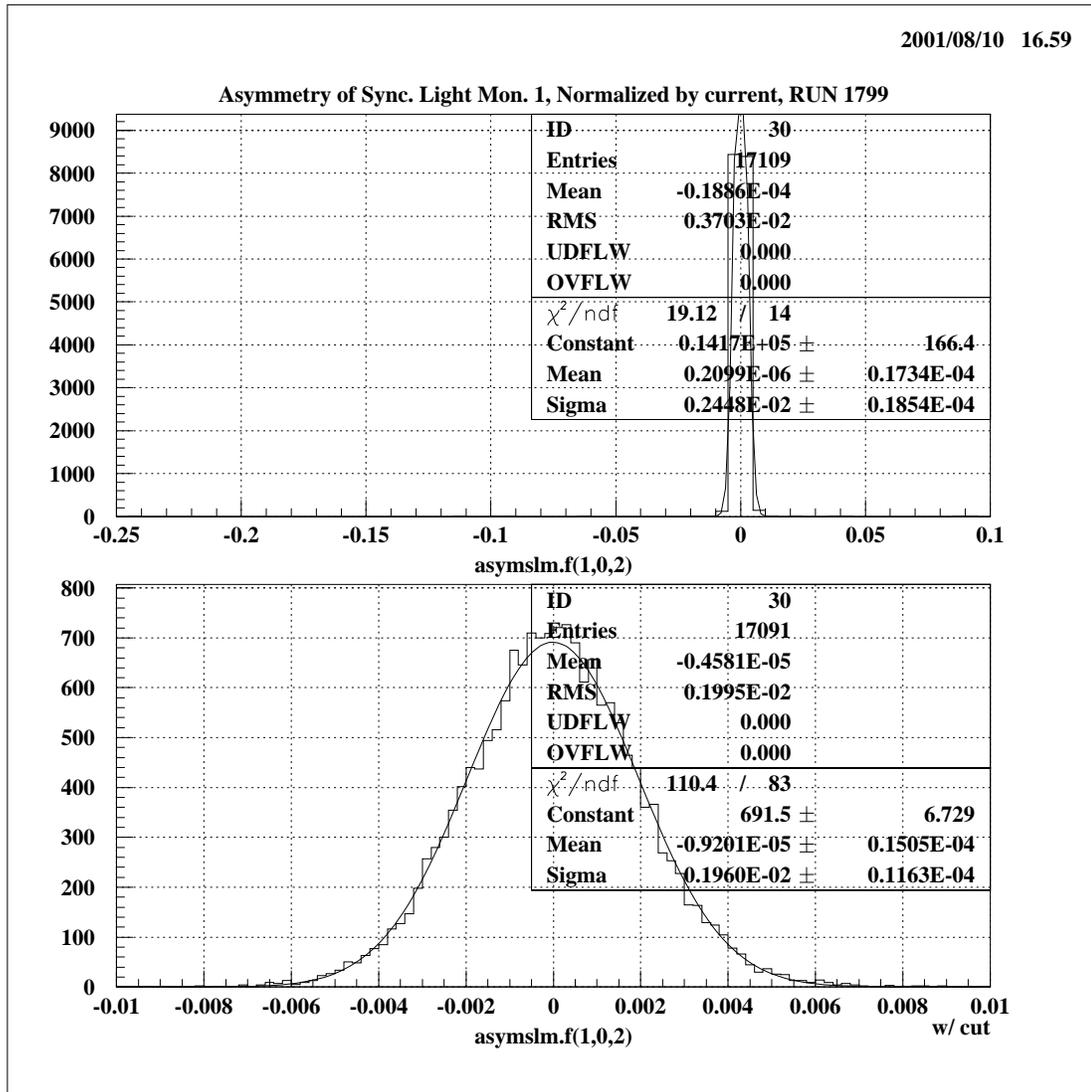


Figure 3.11: Showing *normalized* SLM 1 raw asymmetry for run 1799 a) upper plot; no cut case, b) bottom plot; the same as a) except for with cutting one outlier event.

energy from an SLM asymmetry first we find correlation by fitting, second we subtract the correlation times the energy out of the asymmetry. That is basically the procedure for regression with one parameter and is the same for n parameters. A regressed asymmetry for n parameters looks like;

$$A_n = A_{raw} - \sum_{i=1}^n C_i \cdot x_i \quad (3.7.2)$$

where C_i is the correlation coefficient of the i th beam parameter(x_i). However, there is one subtlety on the coefficients especially for second and later ones, which is to take the asymmetry regressed by preceding parameters rather than taking unregressed one as the function for the fitting. It looks like a feedback loop. Mathematically:

$$C_n \neq \frac{\Delta A_{raw}}{\Delta x_n} \quad , \text{ rather } \quad C_n = \frac{\Delta A_{n-1}}{\Delta x_n} \quad (3.7.3)$$

$$\text{where } \Delta A_{n-1} = \Delta A_{raw} - \sum_{i=1}^{n-1} C_i \cdot \Delta x_i$$

The inequality in Eq. 3.7.3 could still be valid, but then we have to assume that parameters be independent from each other, which is not the case here. In fact, as mentioned earlier that we measure energy (E) and angles (θ_x, θ_y) via BPMs which means they really are functions of positions(x or y) which are also the parameters for the asymmetry regression at the same time.

By using 5 parameters, energy, positions and angles ($E, x, y, \theta_x, \theta_y$) respectively, (Fig.3.12 and Fig.3.13), for $\sigma_{A_{raw}} = 3.47 \times 10^{-03}$ /gate pair, we were able to regress down to $\sigma_{A_{regressed}} = \boxed{1.84 \times 10^{-03}}$ (Fig.3.14).

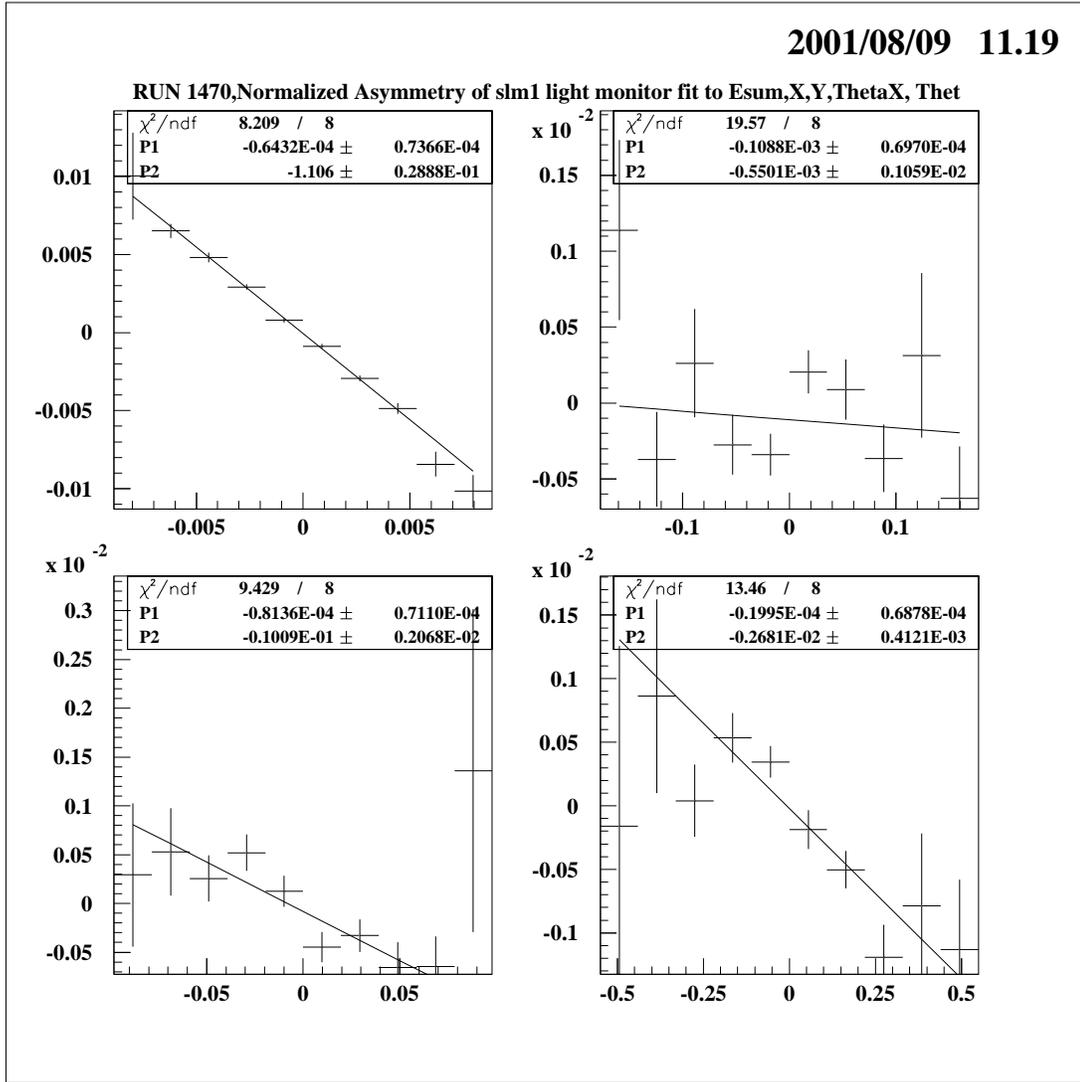


Figure 3.12: First order polynomial fits of a) top left; $A_{raw}(= A_0)$ vs. E_{sum} , b) top right; $A_1(= A_{raw} - C_{Esum} \cdot E_{sum})$ vs. x , c) bottom left; $A_2(= A_{raw} - C_{Esum} \cdot E_{sum} - C_x \cdot x)$ vs. y , d) bottom right; $A_3(= A_{raw} - \sum_{i=1}^3 C_i \cdot x_i)$ vs. θ_x . P2s are the slopes of the fits and are the correlation coefficients at the same time.

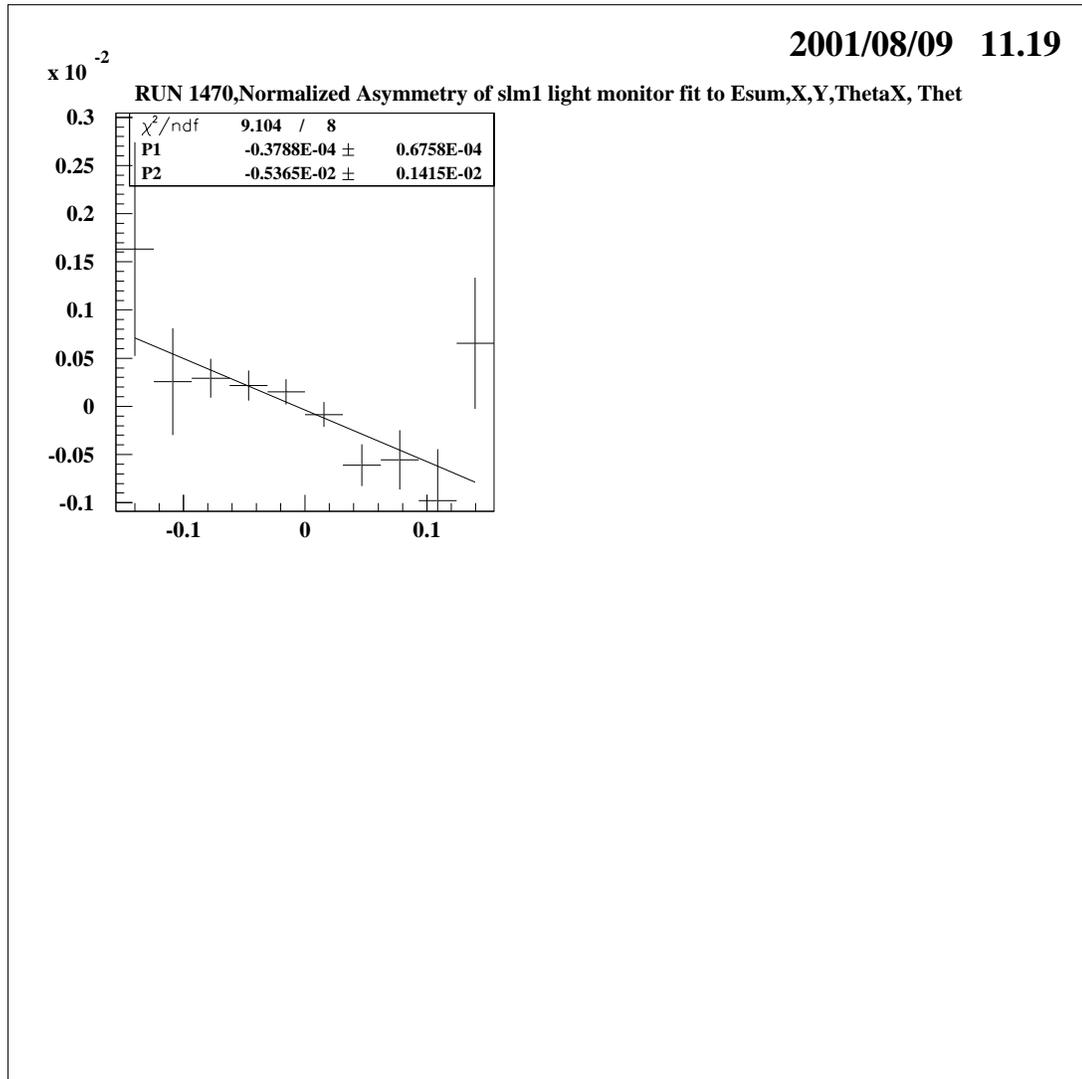


Figure 3.13: First order polynomial fit of $A_4(= A_{raw} - \sum_{i=1}^4 C_i \cdot x_i)$ vs. θ_y , as continuation of the previous figure.

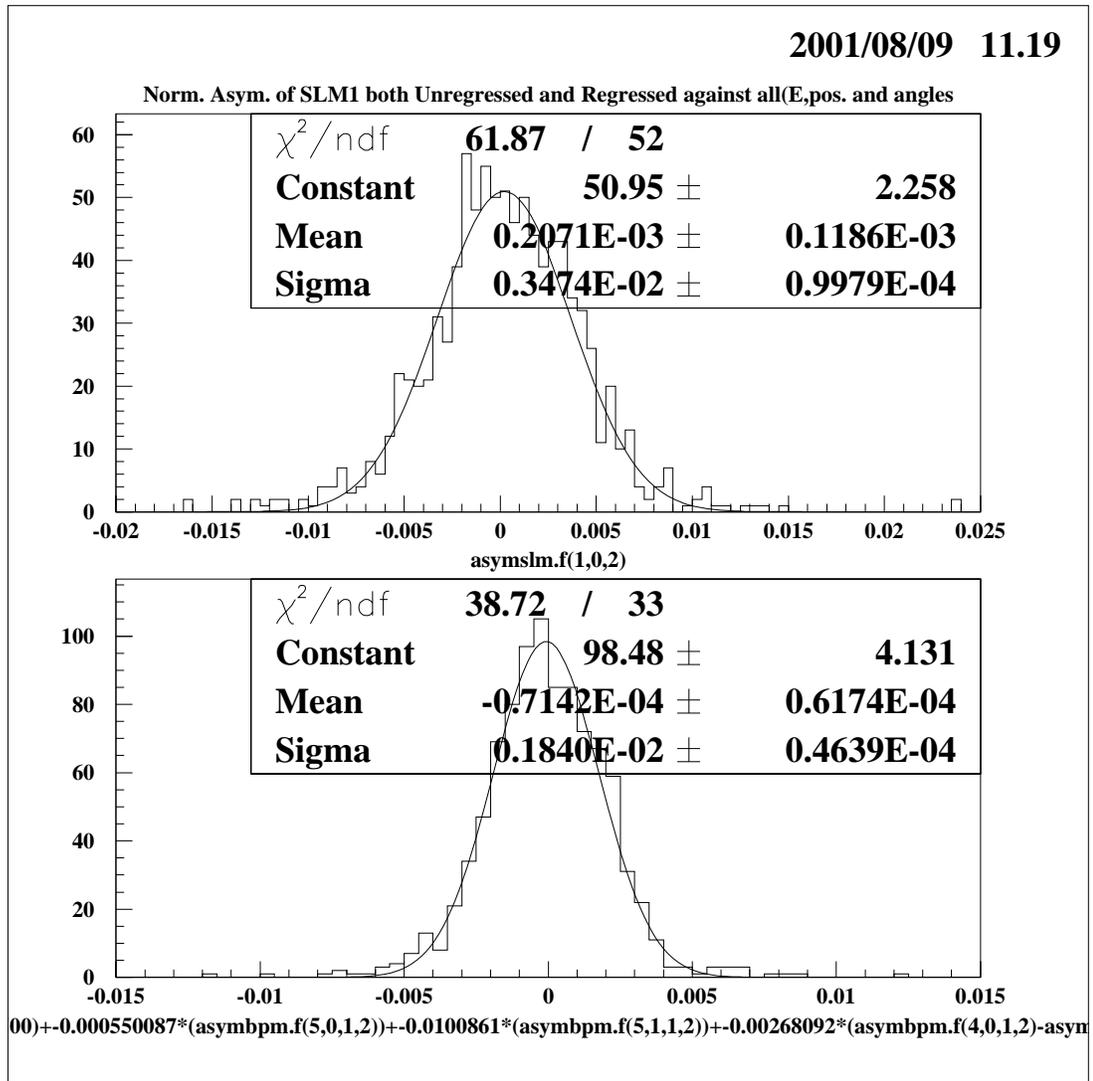


Figure 3.14: *Normalized SLM 1 asymmetry distribution a) top plot; raw, b) bottom plot; regressed to $E, x, y, \theta_x, \theta_y$ for the run 1470*

As further step, one might attempt to combine two SLM monitor data in order to see $\sqrt{2}$ scaling both on the $\sigma_{A_{raw}}$ and $\sigma_{A_{regressed}}$. However, such reduction was not observed as a result of comparison of the raw and regressed plots separately shown in Fig. 3.14 and Fig. 3.15.

3.8 What we have done

Our aim is/was to get as much information as possible from the SLMs we have. The raw data was on tapes but there were no machinery to make them suitable for the analysis. Therefore, we put some time and energy on modifying the existing machinery in order to make this happen before passing to the analysis. After that, we did some pedestal, linearity and regression analysis. However, more data is yet to be processed.

3.9 Conclusion

We were able to limit the vertical polarization using the data from magnets and realized that it is within the tolerable level. With a very small fraction of processed SLM data at hand, we are quite far from the determination of the P_σ using $A_{regressed}$. However, the analysis of the SLM data lead to the conclusion that some updates be necessary in the current setup. One of these is to replace the photodiodes with the ones that have more active surfaces. This will help dominate signal over noise. The other update will be to upgrade the ADC from 11 bit to 16 bit in order to increase the signal resolution while being digitized.

According to the SLM data after the modifications made in the setup, it was seen that the improvements seemed to help a lot to lower the widths of the slm

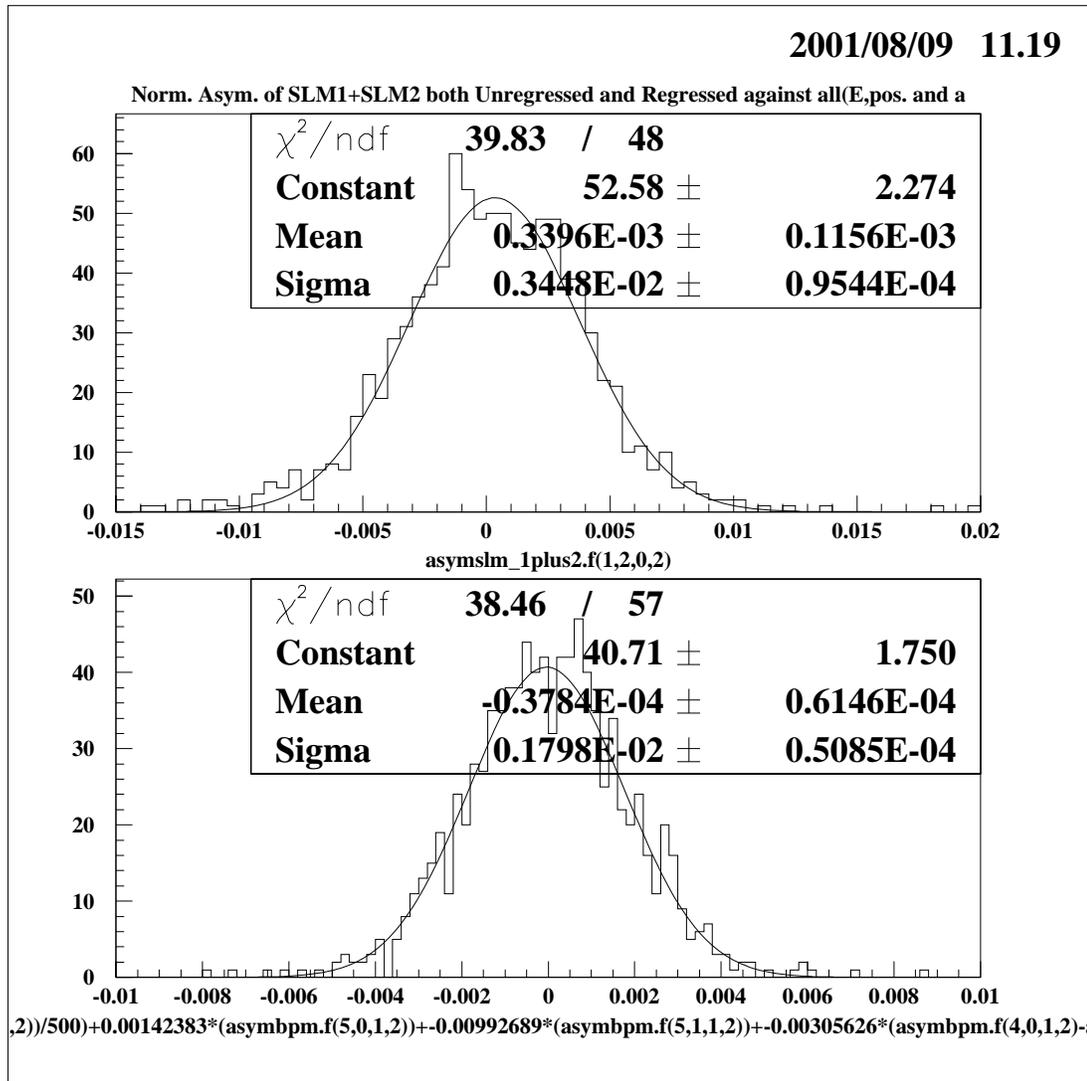


Figure 3.15: Sum of SLM 1 and SLM 2 *normalized asymmetry distribution* a) top plot; raw, b) bottom plot; regressed to $E, x, y, \theta_x, \theta_y$ for the run 1470

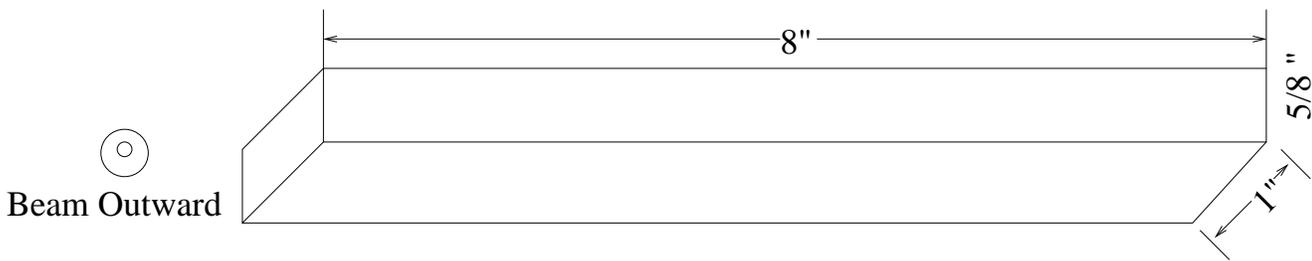
asymmetry both for the regressed and the unregressed cases [21].

3.9.1 Technical Drawings of SLM

During an A-line access we did some remeasurements of high energy SR detector for upcoming modifications as a result of the analysis. Mainly, three technical drawing are attached for future reference, of which quartz bar (Fig.3.16), SR detector backplate where photodiodes are mounted (Fig.3.17) and SR detector box (Fig.3.18).

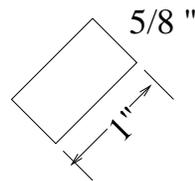
Drawing of Quartz Bar in High Energy Synchrotron Radiation Detector Box

3D VIEW



SIDE VIEW

Beam Direction



Notes: Mirror thickness in the detector box 1/8" and tilted by 45 degrees.

Figure 3.16: Technical drawing of quartz bar.

High Energy SR detector backplate drawing

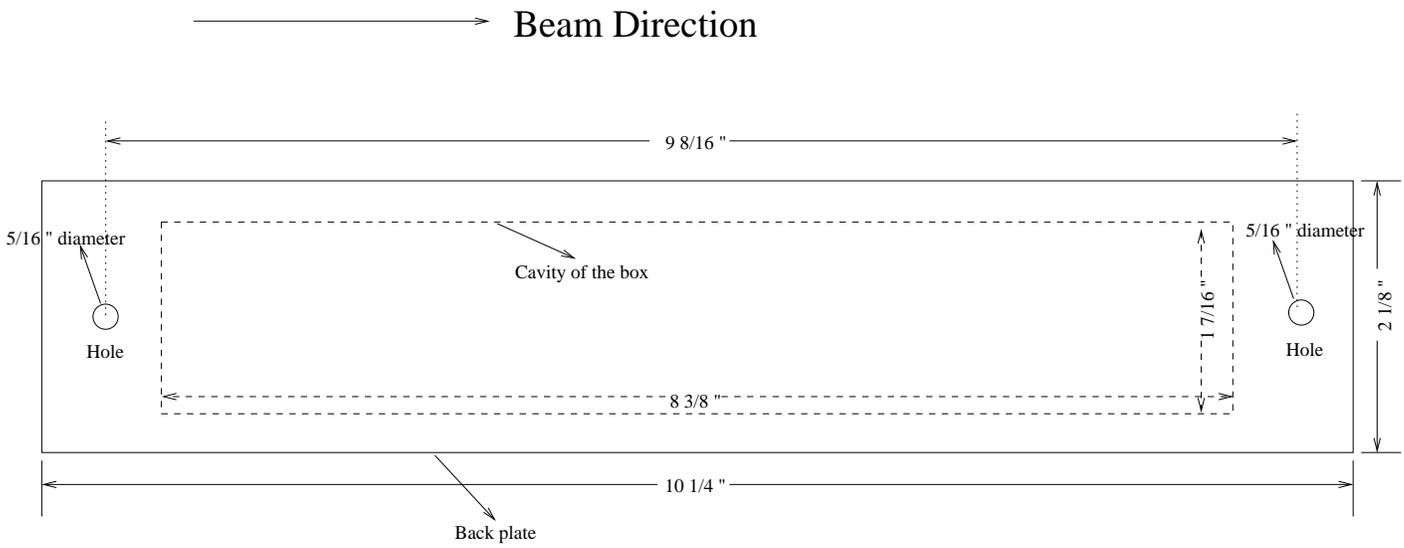


Figure 3.17: Technical drawing of high energy synchrotron radiation detector backplate.

High Energy Synchrotron Detector Box

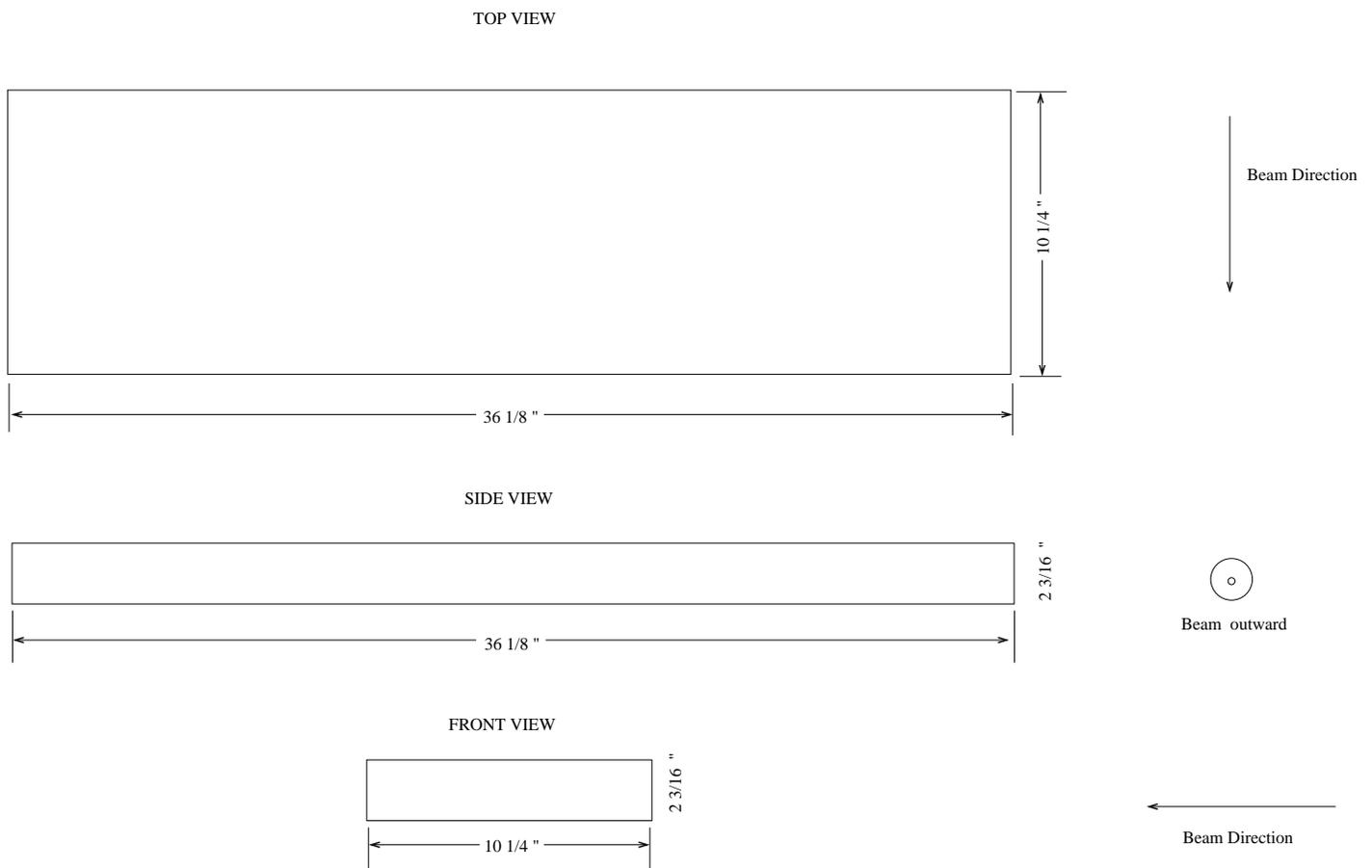


Figure 3.18: Technical drawing of high energy synchrotron radiation detector box.

Chapter 4

Asymmetry Corrections for HAPPEX

4.1 Introduction

In this chapter, we describe how HAPPEX data was organized, how the raw asymmetry was defined and how it was corrected. In the end, the corrections to the raw asymmetry, i.e. the asymmetry corrections for HAPPEX, are presented.

4.2 Organization of the Data

The types of data sets used in HAPPEX are *gate*, *run* and *slug*. The smallest type of data is *gate*. Typically, for $100\mu\text{A}$ beam current with 30 Hz repetition rate, a gate includes in the order of 10^{13} electrons. In addition, the electrons in a gate are in the same helicity state, either -1 or +1. Another type of data set is *run*. A run, generally, is one hour length of data which contains about 100K gates or 50K gate

pairs. It is the kind of data in which most of the parameters are averaged over by DAQ. Another type of data that consists of runs is *slug*. HAPPEX has 20 slugs. Each slug consists of 30 to 70 runs in one particular mode, either with half-wave plate in or with half-wave plate out. The half wave plate reverses the helicity of the laser and hence that of electrons. It is used to eliminate the systematic effects due to the laser source.

4.3 Raw Asymmetry

For a detector, the raw asymmetry A_{raw} is defined by

$$A_{raw} = \frac{D'^+ - D'^-}{D'^+ + D'^-} \quad , \quad D' \equiv \frac{D}{I} \quad (4.3.1)$$

where D' is the detector signal D normalized to the beam current I . The superscript $+(-)$ shows that the helicity state of the gate for that particular signal is $+1(-1)$. As can be seen, we need at least two gates with opposite helicity states to obtain A_{raw} . Therefore, at Jlab, the gates are grouped in pairs called *gate pairs*. Every gate pair comprises of one gate with $+1$ helicity and one gate with -1 helicity. One feature of the gate pairs at Jlab is that the state of the helicity of the first gate of a pair is assigned randomly; conversely, the helicity of the second gate is the complement of the first. For example, if the helicity of the first gate of a pair is assigned as $-1(+1)$ then the helicity of the following gate of that pair must be $+1(-1)$. The randomness in the helicity assignment prevents the helicity from coupling with the noise at any frequency.

Eq. 4.3.1 filters out most of the effects except the net effect ΔA , known as asymmetry correction, arising from the helicity correlated differences in beam parameters: intensity, position, and energy. These differences presumably arise at the

electron gun, proceed through accelerator, beam monitors, target, and finally show up in the raw asymmetry. This effect must be eliminated from the raw asymmetry in order to obtain true asymmetry A_{true} which is

$$A_{true} = A_{raw} - \Delta A \quad (4.3.2)$$

In the next section, it is shown how-to-calculate the asymmetry correction ΔA for a detector.

4.4 Asymmetry correction

The asymmetry correction can be calculated by

$$\Delta A = \frac{\sum_{i=1}^n \left(\frac{\partial D'}{\partial M_i} \right) \Delta M_i}{\left(\frac{\langle D^+ + D^- \rangle}{I} \right)} \quad (4.4.1)$$

where n is the total number of the BPMs (Beam Position Monitors) used for the calculations in general; for the experiment it is equal to 5. Partial derivatives $(\partial D' / \partial M_i)$ are the quantities that show the sensitivity of the detector signal to a monitor (i.e. a beam parameter). The key assumption is that the detector signal is linearly dependent on the 5 BPMs. The partial derivatives will be explained more in the following paragraph. The factor, ΔM_i is the gate pair position difference in the BPMs . The denominator term is the average of the sum of the detector signals of the gate pair normalized to the beam current. It has been explained in chapter 3 how the beam position parameters are utilized to measure the beam parameters.

4.4.1 Computation of $\frac{\partial D'}{\partial M_i}$

The partial derivatives $\partial D'/\partial M_i$ cannot be obtained directly. The indirect way is discussed as follows. Modulation coils are placed upstream of BPMs so that position and angle of the beam can be perturbed deliberately. Fig. 4.1 shows where modulation coils, and beam position monitors stand on Hall A beam line [35]. In addition, the energy of the beam is modulated by an energy vernier in the accelerator. The coils and the energy vernier are ramped consecutively under computer control and this is known as dithering procedure. As a convention, the energy vernier is thought of as another coil and this will be valid for the rest of the text. In HAPPEX, the position and the energy of the beam are modulated approximately by ± 0.1 mm and ± 500 KeV respectively.

We can calculate $\partial D'/\partial M_i$ terms mathematically by using the information provided by the dithering procedure. The information readily available is the response of the detector and the BPMs to the coils: $\partial D'/\partial C_j$ and $\partial M_i/\partial C_j$ respectively. Let us find out $\partial D'/\partial M_i$ in terms of $\partial D'/\partial C_j$ and $\partial M_i/\partial C_j$. For j th coil, one can write

$$\frac{\partial D'}{\partial C_j} = \sum_{i=1}^5 \left(\frac{\partial D'}{\partial M_i} \right) \left(\frac{\partial M_i}{\partial C_j} \right) \quad (4.4.2)$$

In order to accommodate the detector response from all coils rather than j th one, writing in matrix form would be more appropriate. Therefore, writing Eq. 4.4.2 for all coils in the matrix form is

$$\mathbf{D}'_{\mathbf{c}} = \mathbf{D}'_{\mathbf{m}} \mathbf{M}_{\mathbf{c}} \quad (4.4.3)$$

where

$$\mathbf{D}'_{\mathbf{c}} \equiv \left(\frac{\partial D'}{\partial C_1} \quad \frac{\partial D'}{\partial C_2} \quad \dots \right)_{1 \times k}, \quad \mathbf{D}'_{\mathbf{m}} \equiv \left(\frac{\partial D'}{\partial M_1} \quad \frac{\partial D'}{\partial M_2} \quad \dots \right)_{1 \times n} \quad (4.4.4)$$

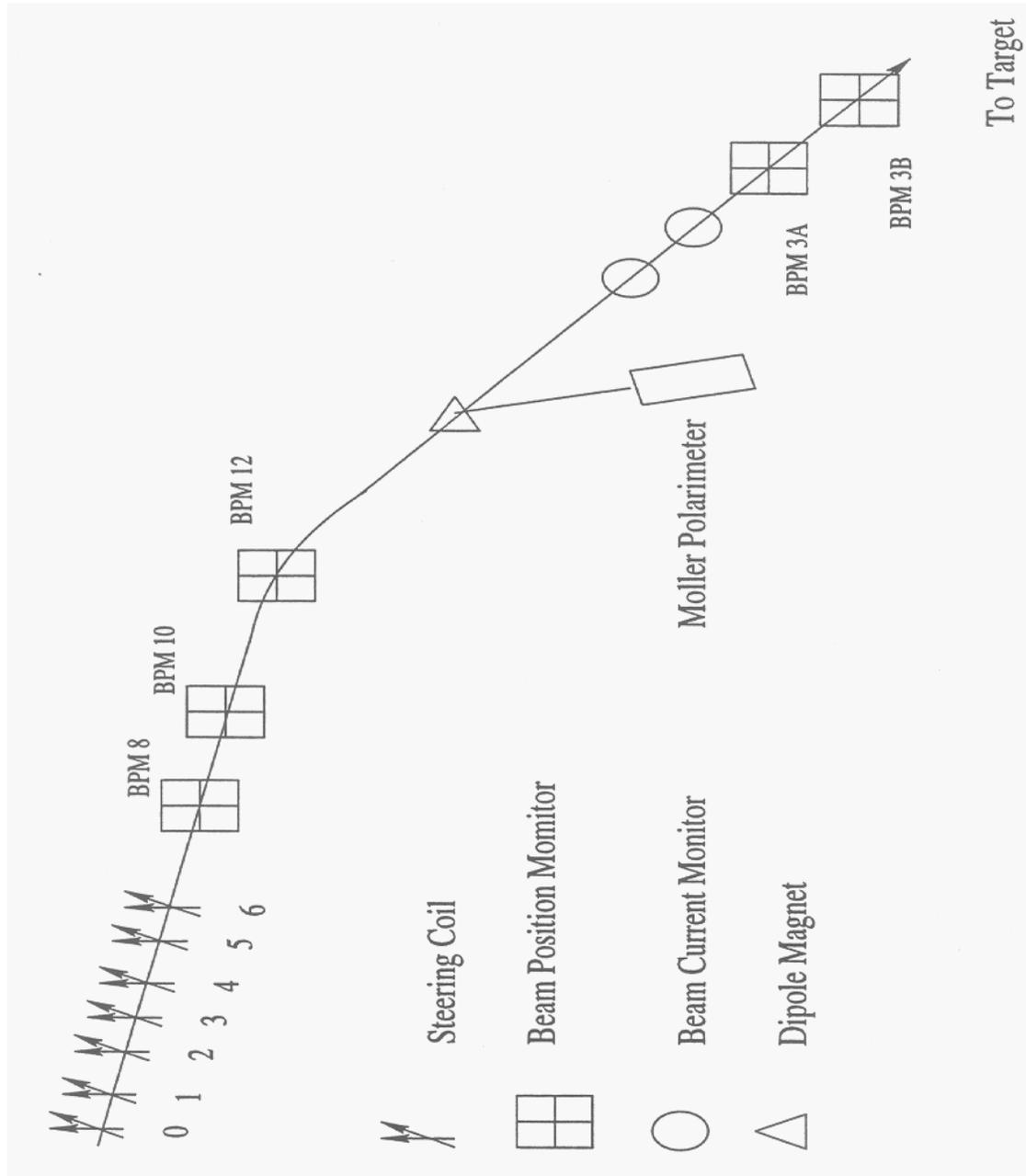


Figure 4.1: Hall A beam line instrumentation.

and

$$\mathbf{M}_c \equiv \begin{pmatrix} \frac{\partial M_1}{\partial C_1} & \frac{\partial M_1}{\partial C_2} & \cdots \\ \frac{\partial M_2}{\partial C_1} & \frac{\partial M_2}{\partial C_2} & \cdots \\ \vdots & \vdots & \ddots \end{pmatrix}_{n \times k} \quad (4.4.5)$$

Here, the number of chosen coils (k) as the number of chosen monitors (n) is 5. Evidently, if both sides of the Eq. 4.4.3 multiplied by \mathbf{M}_c^{-1} from right side, then \mathbf{D}'_m will be

$$\mathbf{D}'_m = \mathbf{D}'_c \mathbf{M}_c^{-1} \quad (4.4.6)$$

As can be guessed that \mathbf{D}'_m involves plenty of algebra; hence, it requires programming. In HAPPEX, *Anpar* is the program that does the matrix inversion and returns the values of \mathbf{D}'_m .

4.4.2 Computation of ΔA

The asymmetry correction can be calculated by using Eq. 4.4.1 directly or indirectly. Here, the indirect way is described. One can rewrite Eq. 4.4.1 as

$$\Delta A = \sum_{i=1}^5 a_i \Delta M_i \quad , \quad a_i \equiv \left(\frac{\partial D' / \partial M_i}{\langle D^+ + D^- \rangle / I} \right) \quad (4.4.7)$$

ΔA above is calculated for a gate pair only. Therefore, averaging is necessary to obtain one value representing whole data. The asymmetry correction averaged over a slug, $\langle \Delta A \rangle_{slug}$, can be written as

$$\langle \Delta A \rangle_{slug} = \sum_{i=1}^5 \langle a_i \rangle_{slug} \langle \Delta M_i \rangle_{slug} \quad (4.4.8)$$

where the latter terms are supplied by the DAQ while the former terms are obtained by averaging $\langle a_i \rangle_{run}$, a_i averaged over a run, values for the slug. One example that

shows how the data look like for slug 11 is given in Fig. 4.2. In addition, plotting a_i terms for all slugs provide us information with regard to the stability of the modulation hardware. Some of them are illustrated in Fig. 4.3.

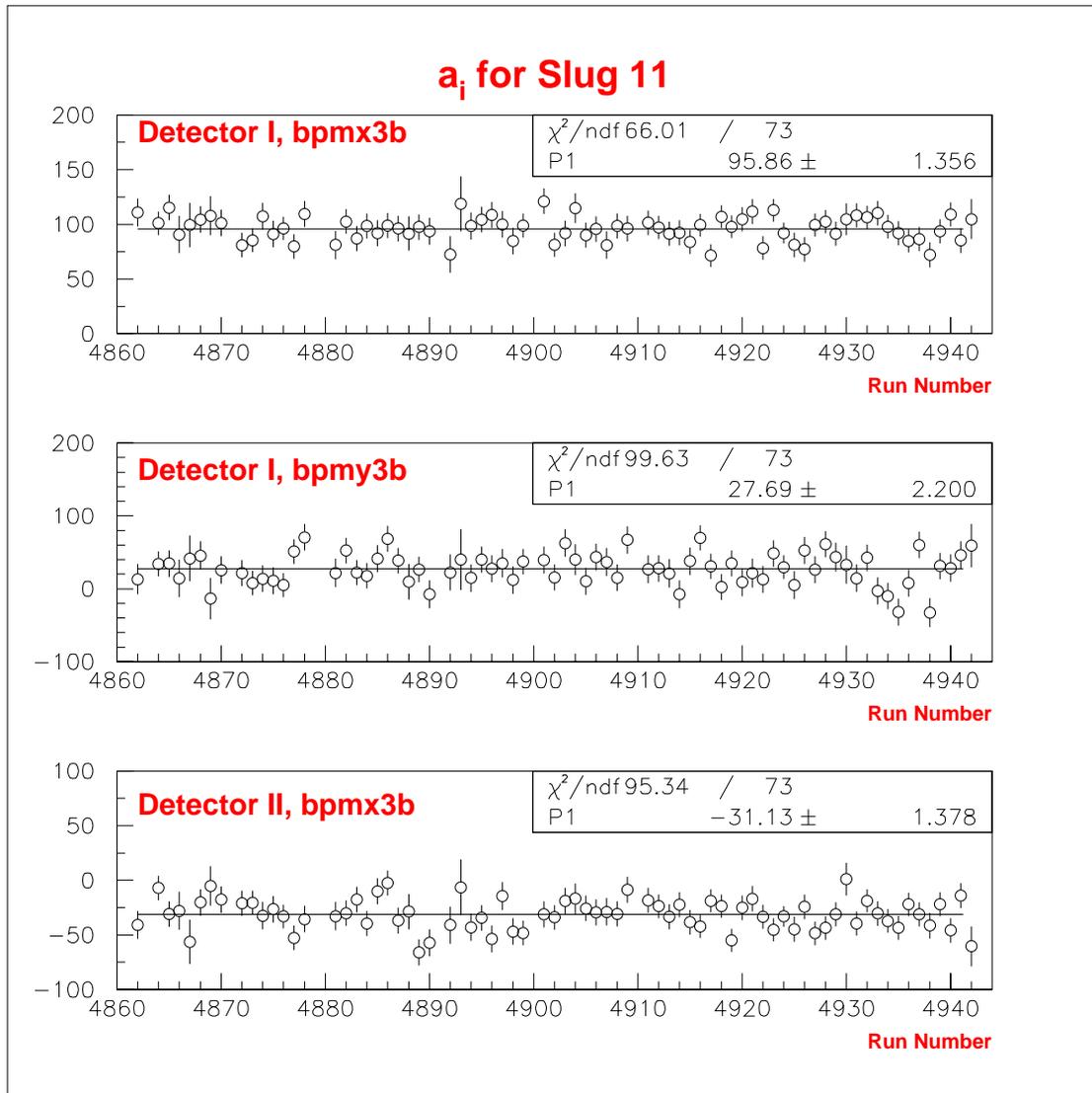


Figure 4.2: Representative plots of the a_i versus run number for slug 11 including their fits to straight line.

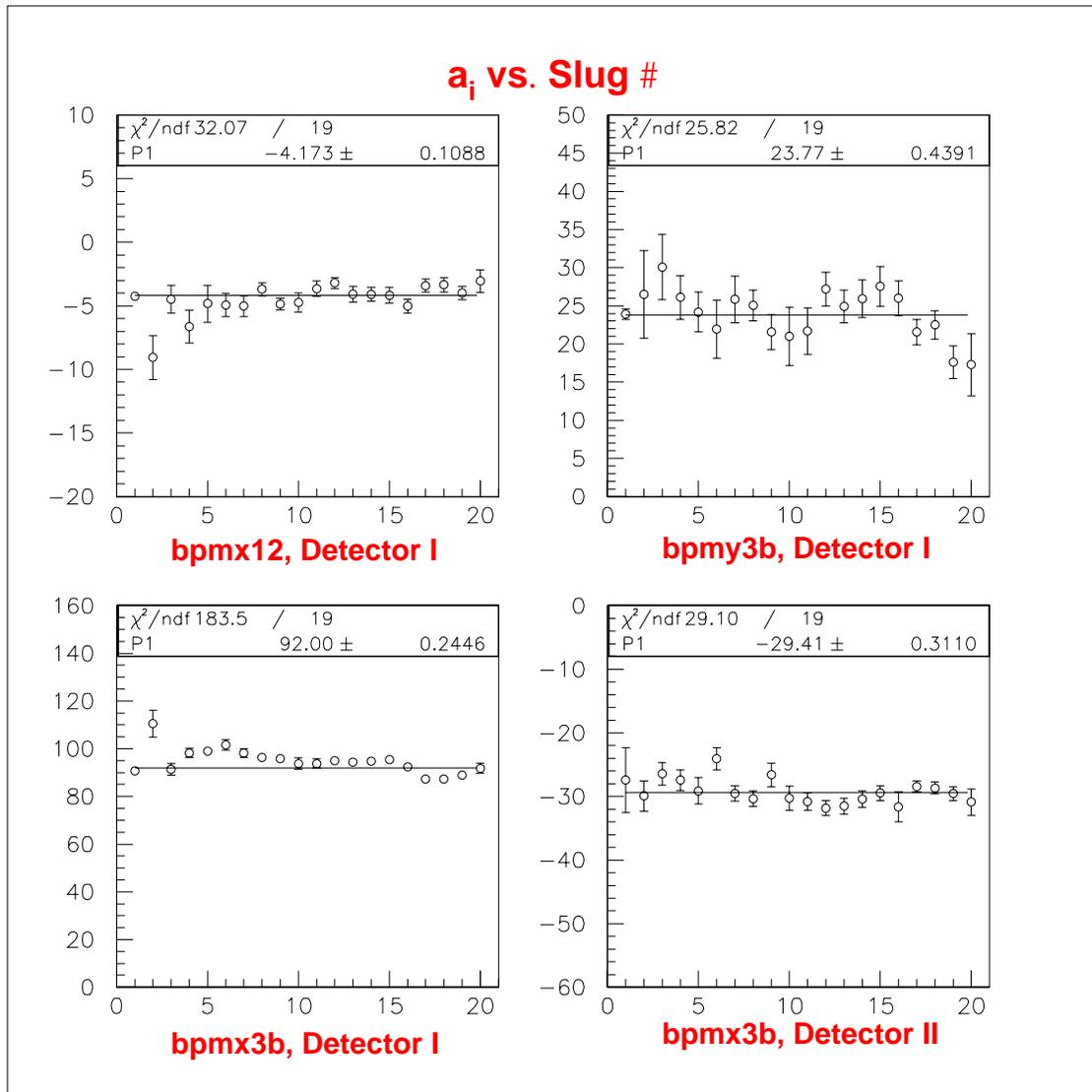


Figure 4.3: Representative plots of the a_i overall slugs.

Finally, the asymmetry correction ΔA is obtained by averaging the corrections calculated in Eq. 4.4.8 for each detector separately. Fig. 4.4 shows the asymmetry correction results for HAPPEX accompanied by the results calculated by the straightforward method. The results are 0.048 ± 0.034 and 0.003 ± 0.013 ppm (parts per million) for both detector I and detector II respectively. The results obtained by the other method for the detector I and II are 0.032 ± 0.034 and -0.002 ± 0.014 ppm respectively. Consequently, the results of both methods agree within errors, and the contribution of the helicity correlated beam differences to the raw asymmetry is found to be negligibly small. Bigger values in the asymmetry correction results indicate a major problem where it was the case of slug 18 of detector I. We realized that the tuning of the beam was not good.

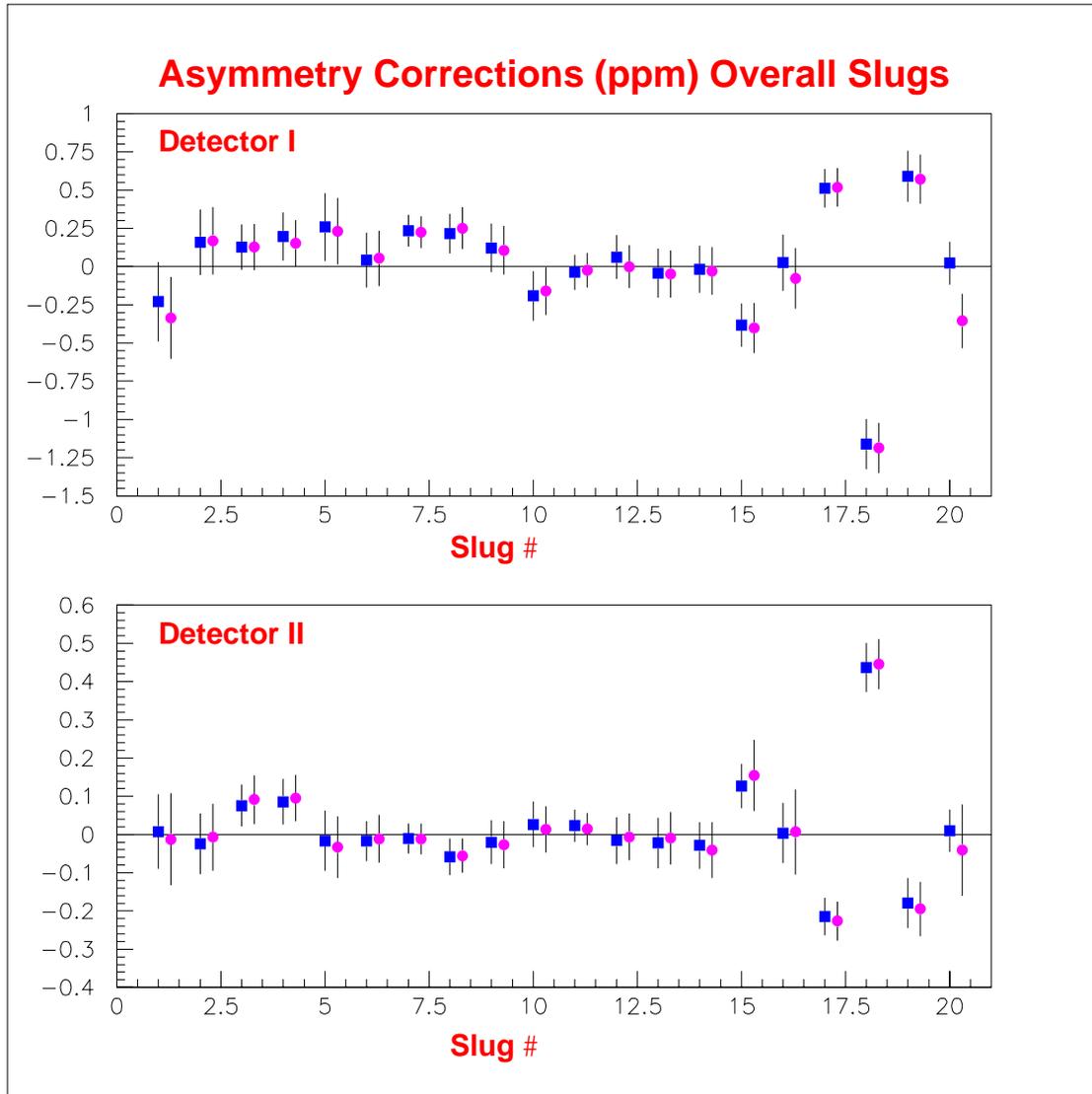


Figure 4.4: Asymmetry corrections for detectors I and II versus Slug number. Results using the straightforward method are also shown as solid circles.

Chapter 5

HAPPEX Results and Conclusions

5.1 Results

After the data taking the asymmetry we have is raw asymmetry(A_{raw}). Fig. 5.1 shows A_{raw} as a function of data set number for both spectrometers. In order to get the experimental asymmetry (A_{exp}) the relation below is used.

$$A_{exp} = \frac{A_{raw}}{P_e} \quad (5.1.1)$$

where P_e is the average of the measured electron polarization. The polarization for the experiment is $P_e \approx 70\%$. Fig. 5.2 shows a number of measurements versus time for the part of the run using techniques of Compton polarimeter and Moller scattering.

The experimental asymmetry for the 1999 data is $A_{exp} = -15.1$ ppm at $Q^2 = 0.477$ $(GeV/c)^2$ [37]. If the 1998 data reported earlier is extrapolated from 0.474 $(GeV/c)^2$ to same Q^2 then it gives $A_{exp} = -14.7$ ppm [38]. The summary of the errors is given

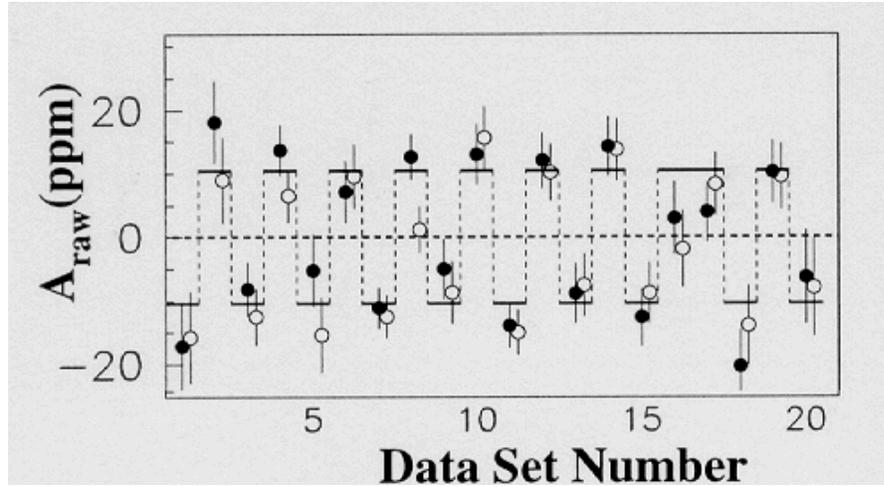


Figure 5.1: Plot of A_{raw} versus data set number. The full circles are from left spectrometer and the empty circles are from the right spectrometer. The superimposed pattern is due to half wave plate mode.

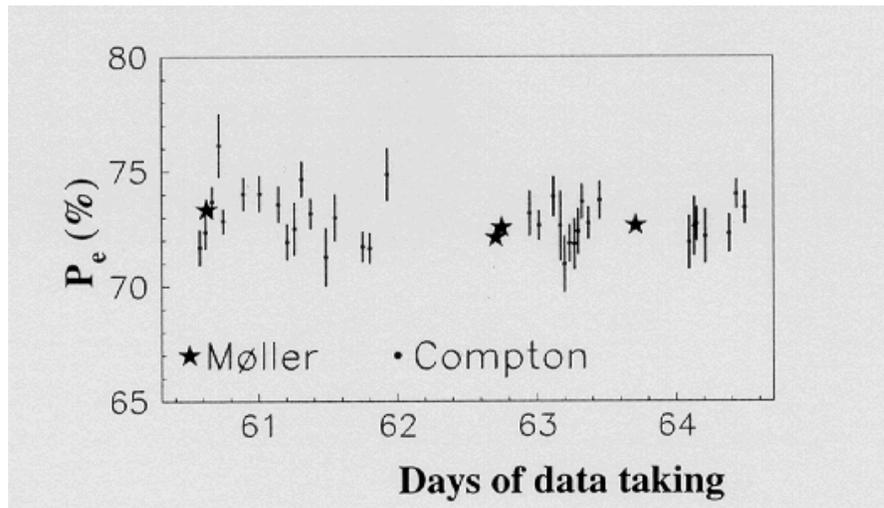


Figure 5.2: Showing a part of the electron polarization measurements performed daily basis via both Moller and Compton polarimetry methods.

in table 5.1. The combined result is $A_{exp} = -15.05 \pm 0.98 (stat.) \pm 0.56 (syst.)$ ppm at $Q^2 = 0.477 \text{ (GeV/c)}^2$ and $\theta = 12.3^\circ$.

Table 5.1: Summary of contributions to the errors in % for the measured asymmetry.

Source	$\delta A/A(\%):1998$	$\delta A/A(\%):1999$
Statistics	13.3	7.2
P_e	7.0	3.2
Q^2	1.8	1.8
Backgrounds	0.6	0.6

By substituting measured value into the Eq. 1.4.1 together with the theoretical value of the proton axial form factor, $A_A = (0.56 \pm 0.23)$ ppm [39, 40], the linear combination of $G_{E,M}^0$ is given by

$$\frac{G_E^0 + \beta G_M^0}{(G_M^{p\gamma}/\mu_p)} = 1.527 \pm 0.048(stat.) \pm 0.027(syst.) \pm 0.011(\delta A_A) \quad (5.1.2)$$

Finally, if this result and the data for the electromagnetic form factors from table 5.2 [41]- [48] are utilized in Eq. 1.4.2, then the linear combination of the strange form factors is given by [37]

$$G_E^s + 0.39G_M^s = 0.025 \pm 0.020 \pm 0.014 \quad (5.1.3)$$

where the first error is the error in G^0 and the second error is due to the electromagnetic form factors. The plot of G_E^s versus G_M^s , which uses the equation above is given in Fig. 5.3 where the estimates from different models [3, 5, 7-9] are also shown. The data points estimated from [3] and [7] are excluded by our result.

Table 5.2: Electromagnetic form factors normalized by G_M^p/μ_p .

Form Factor	Value	Ref.
$G_E^p/(G_M^p/\mu_p)$	0.99 ± 0.02	[41, 42]
$G_E^n/(G_M^p/\mu_p)$	0.16 ± 0.03	[44-48]
$(G_M^n/\mu_n)/(G_M^p/\mu_p)$	1.05 ± 0.02	[43]

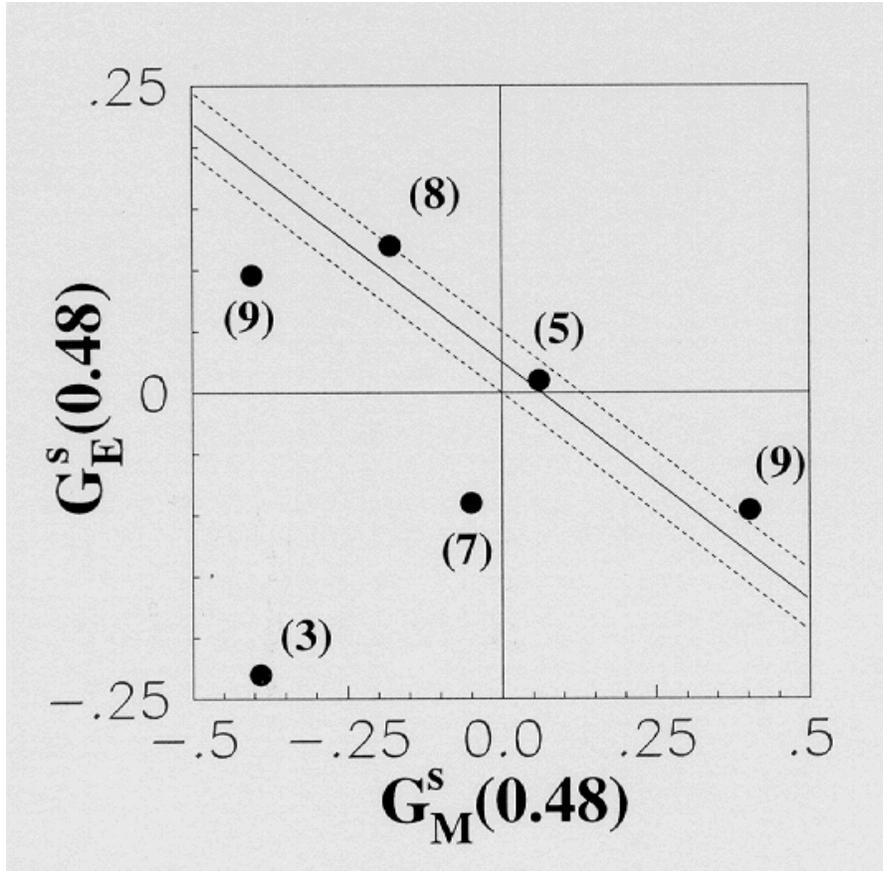


Figure 5.3: Plot of G_E^s versus G_M^s at $Q^2 = 0.477$ $(\text{GeV}/c)^2$ is accompanied by the data points from various models [3, 5, 7-9] at the same Q^2 . The numbers near the data points are the reference numbers of the models. Ref. [9] is plotted twice due to a sign ambiguity.

5.2 Discussion

By looking at the result, one can say that the $s\bar{s}$ contribution to the electric and magnetic properties of the proton is smaller than that of many of the predictions. This is consistent with the assumption of the standard model so far. Even though the 1999 data has the half of the statistical and systematic errors of the 1998 data, the conclusion remains the same. Since the experiment has yielded the result for the linear combination of G_E^s and G_M^s rather than separate results for each of the strange form factors, it is within the possibilities that both of them may be small [5] or may be canceling each other [8,9]. Therefore, there are new experiments underway to find out which one is the case. There are two experiments approved at Jlab at $Q^2 \sim 0.1(GeV/c)^2$. One [49] of them will measure the same combination at a low Q^2 and the other [50] will be sensitive to G_E^s but not G_M^s . The former will use a hydrogen and the latter will use a ^4He target. In addition to these experiments, there are two more experiments underway: the G^0 experiment [51] at Jlab and the Mainz A4 experiment [52] at the Mainz Microtron (MAMI). The G^0 experiment will make a complete set of measurements for $0.16 < Q^2 < 0.95(GeV/c)^2$ using both the liquid hydrogen and the liquid deuterium as the targets. The Mainz A4 Collaboration will make the measurement at $Q^2 = 0.23(GeV/c)^2$ by using either a liquid hydrogen or a liquid deuterium target.

Bibliography

- [1] J. Ashman, *et al.*, Phys. Lett. B 206, 364 (1988).
- [2] J. Ashman, *et al.*, Nucl. Phys. B 328, 1 (1989).
- [3] H.-W. Hammer, Ulf-G. Meissner, and D. Drechsel, Phys. Lett. B 367 (1996) 323.
- [4] See for example, D.H. Perkins, *Introduction to High Energy Physics*, Addison-Wesley Pub. Comp., Menlo Park,CA, (1987) p.386-389.
- [5] H. Weigel *et al.*, Phys. Lett. B 353 (1995) 20.
- [6] D. Griffith, *Introduction to Elementary Particles*, John Wiley and Sons, NY, 1987 page 198-199.
- [7] N.W. Park and H. Weigel, Nucl. Phys. A 541 (1992) 453.
- [8] S. J. Dong, K.F. Liu, and A. G. Williams, Phys. Rev. D 58 (1998) 074504.
- [9] H.-W. Hammer and M. J. Ramsey-Musolf, Phys. Rev. C 60 (1999) 045205.
- [10] Particle Data Group, K. Hagiwara *et al.*, Phys. Rev. D 66(2002) 010001.
- [11] S. Godfrey, Phys. Rev. D 51, 1402 (1995)

- [12] E. J. Eichten, K.D. Lane and M.E. Peskin, Phys. Rev. Lett. 50, 811 (1983).
- [13] B. Schrempp *et al.*, Nucl. Phys. B 296, 1 (1988).
- [14] B.W. Lynn, M.E. Peskin and R.G. Stuart, in *Physics at LEP*, CERN Report No. CERN-86-02 (1986).
- [15] M.E. Peskin, T. Takeuchi, Phys. Rev. D 46, 381 (1992).
- [16] October 2, 2000 SLAC-I-040-20200-001-R003 10.1, Page 1 of 1,
<http://www.slac.stanford.edu/grp/ad/addo/toc/20200-001BLMaps.html>
- [17] M.S. Griffo, *Design for Electron Beam Energy Monitors Using Synchrotron Light*, E158 Technical Note #4, SLAC, Stanford, CA.
- [18] Bondar and Saldin, Nucl. Inst. Meth. 195, 577 (1982).
- [19] Belomesthnyleh et al., Nucl. Inst. Meth. 227, 173 (1984).
- [20] B.T. Tonguc, M. Woods, *Report on Synchrotron Radiation Analysis.*, E158 Technical Note, TN #17, SLAC, Stanford, CA, August 2001.
- [21] Private Discussions with M. Woods.
- [22] Private Discussions with P. A. Mastromarino.
- [23] E. Derman and W.J. Marciano, Ann. Phys. 121, 147 (1979).
- [24] Medium Energy Physics Group, Syracuse University,
<http://mepserv.phy.syr.edu/e158/index.html>
- [25] Personal archive of Lou Buda, Syracuse University.

- [26] Particle Data Group *Particle Physics Booklet* extracted from the *Review of Particle Physics* D.E. Groom *et al.*, The European Physical Journal C15 (2000) 1.
- [27] David R. Relyea.
- [28] Peter Bosted.
- [29] P. A. Souder, Internal Collaboration Memo, (unpublished 1999).
- [30] HAMAMATSU company website, <http://usa.hamamatsu.com/hcpdf/catsandguides/Pmt-h>, page 29, diagram 29.
- [31] GEANT 3.21, Detector Description and Simulation Tool, CERN Program Library Long Writeup W5013.
- [32] SLAC-Proposal-E158, P.A. Souder, E.W. Hughes and K.S. Kumar, spokespersons.
- [33] E158 Poster, presented at Lepton Photon 2001, Rome, Italy.
- [34] L. Lyons, *Statistics for Nuclear and Particle Physicists*.
- [35] W.E. Kahl, Ph.D. thesis, Syracuse University, 2000.
- [36] PAW, Physics Analysis Workstation, Cern Program Library Reference Manual, http://wwwinfo.cern.ch/asd/paw/reference_manual/index.html
- [37] K. A. Aniol *et al.*, Phys. Lett. B509:211-216, (2001).
- [38] K. A. Aniol *et al.*, Phys. Rev. Lett. 82 (1999) 1096.
- [39] M. J. Musolf and B.R. Holstein, Phys. Lett. B 242 (1990) 461.

- [40] S.-L. Zhu *et al.*, Phys. Rev. D 62 (2000) 033008.
- [41] R. C. Walker *et al.*, Phys. Lett. A 212 (1996) 231.
- [42] M. K. Jones *et al.*, Phys. Rev. Lett. 84 (2000) 1398.
- [43] H. Anklin *et al.*, Phys. Lett. B 428 (1998) 248.
- [44] I. Passchier *et al.*, Phys. Rev. Lett. 82 (1999) 4988.
- [45] C. Herberg *et al.*, Eur. Phys. Jour. A 5 (1999) 131.
- [46] M. Ostrick *et al.*, Phys. Rev. Lett. 83 (1999) 276.
- [47] J. Becker *et al.*, Eur. Phys. Jour. A 6 (1999) 329.
- [48] D. Rohe *et al.*, Phys. Rev. Lett. 83 (1999) 4257.
- [49] Jlab experiment E99-115 (K. Kumar and D. Lhuillier, spokespersons).
- [50] Jlab experiment E00-114 (D.S. Armstrong and R. Michaels, spokespersons).
- [51] Jlab experiment E91-017 (D. Beck, spokesperson).
- [52] Mainz proposal A4/1-93 (D. von Harrach, spokesperson).

CURRICULUM VITÆ

NAME OF AUTHOR : Baris Tamer Tonguc

PLACE OF BIRTH : Eskisehir, Turkey

DATE OF BIRTH : 4th August, 1973.

GRADUATE AND UNDERGRADUATE SCHOOLS ATTENDED:

Anadolu University, Eskisehir Turkey Syracuse University, Syracuse, NY

DEGREES AWARDED :

Bachelor of Science in Physics, 1993, Anadolu University, Eskisehir, Turkey

Master of Science in Physics, 1998, Syracuse University, Syracuse, NY.

AWARDS AND HONORS :

Graduated from Anatolia University as the valedictorian.

Ranked as the 1st from the top among 172 highly qualified university graduates who took the exam in Physics. As a result, became eligible for graduate level educational scholarship from Ministry of Education in Turkey.

Research Assistant, Syracuse University, 1998-2002.

Graduate Scholarship, Ministry of Education, Turkey 1995-2000.

Teaching Assistant, Syracuse University, Summer 1997.

Teaching Assistant, Dumplupinar University, 1994.

PROFESSIONAL EXPERIENCE :

Talk on “Asymmetry Correction Results”, presented at HAPPEX collaboration meeting at Syracuse in September 1999.

Talk on “Synchrotron Radiation Analysis Results”, presented at E158 collaboration meeting at SLAC, Stanford, CA, August 2001.